Engineering electronic and magnetic properties of surface-confined lanthanide-directed metal-organic networks

Tesis doctoral presentada por

Daniel Moreno Cerrada

Facultad de Ciencias

Departamento de Física de la Materia Condensada

Director de tesis:

Prof. David Écija

Madrid, Octubre de 2021

instituto IMdea nanociencia

EXCELENCIA
SEVERO
OCHOA

UAM
UNIVERSIDAD AUTONOMA
DE MADRID

Abstract

In the last decades the advance of technology is demanding a constant miniaturization of electronic components. On this respect, the role of nanoscience in the development of technology able to operate at the ultimate size scale is crucial. In the age of internet, data science and artificial intelligence, one of the most important challenges to solve is the increment of memory density by surface unit to store large amounts of data in the smallest feasible space. Herein, lanthanide atoms have emerged as potential candidates to be used as single atom magnets for commercial applications, being possible to read and write information on them, thus acting as bits. Nevertheless, the mechanisms to exploit the full potential of these elements are not well understood and very poorly explored on surfaces, which is mandatory for future technological applications.

In this context, metallosupramolecular coordination chemistry of lanthanides on surfaces is postulated in this thesis as a strategy to design nanomaterials that could exploit the potential of lanthanides for information storage and quantum information. We formulate the following two scientific questions: i) Can we tailor the magnetic properties of lanthanide-directed metal-organic networks on surfaces?, and ii) Can such networks feature magnetic remanence, i.e. behave as a robust assembly of single atom magnets on surfaces?

This thesis present distinct surface-confined lanthanide-directed metallosupramolecular networks on surfaces, being characterized by means of STM and STS, introducing for the first time in literature XAS, XNLD and XMCD measurements of lanthanides in two-dimensional coordination environments, which are complemented by DFT and multiplet calculations.

First, the effects of coordination on the magnetic properties of Dy are studied. A Dy-carboxylate metal-organic network featuring square unit cell is synthesized on Cu(111). Comparison with Dy clusters and individual Dy atoms reveals that coordination of Dy by carboxylate moieties improves the magnetic anisotropy and tilts the easy axis, though no opening of the hysteresis loop is detected.

Second, ditopic linear ligands equipped with pyridyl groups coordinate with Dy on Au(111) affording the formation of the first dinuclear lanthanide-directed metallosupramolecular network on Au(111). Notably, the exchange of Dy by Er results in a distinct energy level alignment of the frontier orbitals, while preserving the network structure. Its magnetic characterization reveals a close to in-plane easy axis of magnetization for Dy, whereas such axis is notably tilted for the Er case. In addition, magnetic anisotropy is much higher in Dy than in Er. In both cases, no remanence at zero magnetic field is observed.

To conclude, the metal substrate is identified as the main actor in quenching the magnetic stability of lanthanide networks through the relaxation of the magnetization via the electron and phonon bath from the metal. To circumvent such limitations and inspired from a recent report about magnetic bistability of Dy on Gr/Ir(111), the feasibility of growing lanthanide-direct metal-organic networks on such a sp^2 support is explored. To this aim, a variety of ligands is tested, being successful the coordination of Dy with a three-fold ligand equipped with peripheral carbonitrile groups. As a result, a metallosupramolecular network featuring quasi-hexagonal order and some concomitant defects is obtained. Thus, fascinating opportunities are open to study the electronic and magnetic behaviour of such type of assemblies on decoupling supports.

Our results introduce the first electronic and magnetic characterization of lanthanide-directed metallo-supramolecular networks on surfaces, revealing coordination protocols to tune their easy axis of magnetization as well as their magnetic anisotropy, while identifying the pernicious role of the metallic substrate for magnetic bistability.

We envision further research efforts dedicated to coordination chemistry on decoupling supports such as sp^2 templates grown on metallic substrates.

Altogether, our findings will open new avenues in the fascinating and emerging field of molecular magnetism and quantum information of lanthanide-based nanomaterials.

Resumen

Durante las últimas décadas, el avance de la tecnología está demandando una constante miniaturización de los componentes electrónicos. Respecto a esto, el rol de la nanociencia en el desarrollo de tecnología capaz de operar en la escala última de tamaño es crucial. En la era de internet, la ciencia de datos y la inteligencia artificial, uno de los retos más importantes a solucionar es el aumento de la densidad de memoria por unidad de superficie para almacenar grandes cantidades de datos en el menor espacio posible. En este escenario, los lantánidos han emergido como candidatos potenciales para ser usados como átomos magnéticos para aplicaciones comerciales, siendo posible leer y escribir información en ellos, actuando como bits. Sin embargo, los mecanismos para explotar el potencial de estos elementos no están bien entendidos y han sido poco explorados en superficies, lo cual es fundamental para desarrollar futuras aplicaciones tecnológicas.

En este contexto, la coordinación química de lantánidos en superficies se postula en esta tesis como una estrategia para diseñar nanomateriales capaces de explotar el potencial de los lantánidos como dispositivos de almacenamiento de información e información cuántica. Para ello, formulamos dos preguntas: i) ¿Podemos manipular las propiedades magnéticas de redes metal-orgánicas dirigidas por lantánidos en superficie?, y ii) ¿Pueden estas redes presentar remanencia magnética, es decir, comportarse como una estructura robusta de átomos magnéticos en superficie?

Esta tesis presenta distintas redes metalosupramoleculares basadas en lantánidos en superficie, caracterizadas por STM y STS, introduciendo por primera vez en la literatura de estos sistemas medidas de XAS, XNLD y XMCD, complementadas por cálculos DFT y de multipletes.

En primer lugar, se estudian los efectos de la coordinación en las propiedades magnéticas del Dy. Para ello, se sintetiza sobre Cu(111) una red metal-orgánica formada por enlaces Dy-carboxilato caracterizada por una celda unidad cuadrada. Comparando los resultados con clústers de Dy y átomos de Dy individuales, se observa que la coordinación con grupos carboxilato mejora la anisotropía magnética del Dy e inclina el eje fácil, aunque no se observa apertura del ciclo de histéresis.

En segundo lugar, se observa que ligandos lineales equipados con grupos piridiles coordinan con Dy sobre una superficie de Au(111), permitiendo la formación de la primera red binuclear basada en lantánidos sobre dicha superficie. El intercambio de Dy por Er produce un alineamiento diferente de los niveles energéticos de los orbitales frontera a la vez que preserva la estructura de la red. La caracterización magnética revela un eje fácil de la magnetización casi en el plano para los centros de Dy, mientras que en el caso del Er el eje está notablemente inclinado. En ambos casos, no se ha podido observar remanencia a campo magnético cero.

Para concluir, el sustrato metálico aparece aquí como el principal causante del bloqueo de la estabilidad magnética de las redes de lantánidos a través de mecanismos de relajación magnética vía el baño de electrones y fonones del metal. Para superar dicha limitación, e inspirados por el reciente descubrimiento de biestabilidad magnética de átomos de Dy sobre Gr/Ir(111), se explora la viabilidad de crecer estas redes en este tipo de soportes sp^2. Para ello, se prueba una alta gama de ligandos, resultando exitosa la coordinación de Dy con una molécula con simetría c3 equipada con grupos carbonitrilo en los extremos. Como resultado, se obtiene una red metalosupramolecular quasi-hexagonal con escasos defectos. Tal investigación abre oportunidades fascinantes para estudiar el comportamiento electrónico y magnético de este tipo de autoensamblados de coordinación.

Nuestros resultados introducen la primera caracterización electrónica y magnética de redes supramoleculares basadas en lantánidos en superficies, mostrando que los protocolos de coordinación pueden utilizarse para variar tanto el eje fácil de magnetización como la anisotropía magnética de los lantánidos, además de demostrar el rol pernicioso de los sustratos metálicos en la estabilidad magnética. Por este motivo, nuestros futuros esfuerzos irán dirigidos al crecimiento de capas desacoplantes, ya sean materiales sp^2 o MgO, sobre metales. Nuestros descubrimientos abren nuevas rutas para el fascinante y emergente campo del magnetismo molecular y la información cuántica basada en lantánidos.

Acknowledgments

Es curioso como, cuando te acercas al final de una etapa, de repente te viene a la mente como empezó todo. Fue el 27 de enero de 2017 cuando David Écija me respondió a la solicitud de doctorado. Lo sé porque todavía conservo los correos. En aquel momento le respondí nervioso y concertamos la entrevista que me metería de lleno en este proyecto.

Y aquí estoy ahora, 4 años más tarde, tras haber vivido una experiencia personal y profesional increíble que me ha llevado a pasar por todos los estados emocionales habidos y por haber. Varias veces.

Después de este tiempo ha llegado el momento de agradecer a todo el mundo por todo apoyo, el cariño y la profesionalidad recibida durante estos años.

Y por supuesto a la primera persona a la que le quiero dar las gracias es a mi director, al Profesor David Écija, tanto por darme la oportunidad como por su apoyo incondicional y guía científica. Es justo decir que esta tesis no hubiese sido posible sin su ayuda, y por ello le estaré siempre profundamente agradecido. Ha costado, pero lo hemos conseguido.

Hablando de gente sin la cual no hubiese salido esta tesis, hay dos personas cuyo trabajo y guía han sido imprescindibles para mí en estos últimos años. Una de ellas es el Dr. Koen Lauwaet, o como nos gusta llamarle, Koen. Sin sus impecables conocimientos de instrumentación y su apoyo científico, aún estaría arreglando la máquina. La otra persona es la Dra. Sofía de Oliveira, sin su esfuerzo e infinita dedicación, me hubiese sido imposible racionalizar muchos de los resultados aquí presentados. Muchas gracias a ambos por todo el conocimiento científico que me habéis aportado y por la paciencia ante mis interminables preguntas.

También me gustaría dar las gracias al Dr. José Ignacio Urgel, por las largas discusiones sobre ciencia, tecnología y el apoyo tanto personal como profesional que me ha bridado en estos últimos años. Cuando vuelva nos echamos un café. Y por supuesto quiero agradecerle al Dr. José María Gallego por sus aportaciones, que me han ayudado a ser mejor científico gracias a su increíble pensamiento crítico y rigurosidad científica.

Me gustaría también agradecerle al Dr. José Ignacio Martínez por dar sentido a muchos de los resultados gracias a sus simulaciones. A través de ellas he podido aprender muchas cosas y espero seguir haciéndolo en el futuro.

No puedo olvidarme de la gente del sincrotrón. Muchas gracias al Dr. Manuel Valvidares por aceptarme durante 3 meses en ALBA y por toda la atención e implicación que tuvo conmigo. Y por supuesto, gracias también al Dr. Pierluigi Gargiani por su inestimable ayuda, su conocimiento científico y su infinita paciencia cuando estaba perdido.

Por supuesto, una parte muy importante de esta tesis se debe gracias al apoyo tanto dentro como fuera del laboratorio de mis compañeros de batalla. A Óscar, Cristina y a Kalyan os agradezco muchísimo por el apoyo y las largas sesiones de coaching unos a otros. También quería agradecer a nuestros compañeros del semi sótano, a Cosme, Iván, Joan, Fabián, Manuela y Miguel Ángel Valbuena por su inestimable compañerismo. Y a Borja Cirera, que se le echa de menos por su buen hacer científico y por sus infinitas historias de fin de semana (guiño guiño).

A las nuevas incorporaciones, Sibi, Elena y Ana, estoy seguro de que os irá bien, os deseo la mejor de las suertes.

Y llegados a este punto, quiero agradecer al que ha sido mi mayor apoyo dentro del laboratorio, mi compañera, amiga y casi mi hermana mayor, Ana Sánchez por todas las largas charlas sobre la ciencia y la vida en general, su inestimable ayuda y sobre todo su apoyo profesional y personal. Sé que vas a llegar lejos, y espero estar ahí para verlo.

También quiero darles las gracias a mis compañeros de patrulla, Alberto Martín y Pablo Casado (no el del PP, otro) por su apoyo y amistad tanto dentro como fuera del laboratorio. Cuando termine con esto nos echamos un Apex.

Fuera del laboratorio, quiero dar las gracias a mi familia del colegio, a Diego, Marina, Inma, Estefanía, Elena, Gema, Belén, Jose, Renato, Jesús y Manu, por haber sido como hermanos para mí. También a mis compañeros de la universidad: Raúl, Eva, Germán, Juan, Julio, San Juan y Víctor, por estar en los momentos más oscuros de la tesis y por las largas cenas hablando de cómo hacernos ricos. Seguimos intentándolo.

Finalmente, esta tesis no hubiese sido posible sin el apoyo de mi familia, que siempre creen en mí y me apoyan cuando las cosas se ponen más feas, ayudándome a levantarme y a dar un paso más hacia adelante.

Por último, quería darla las gracias a la persona que más me ha ayudado y apoyado durante este proceso. Y esa persona es Adriana, mi amiga, mi compañera y mi pareja. Muchas gracias por estar ahí incluso cuando yo no quería estar. Por sujetarme cuando ya no podía más y por impulsarme cuando podía con todo. Gracias a ti no solo he podido realizar esta tesis, me has hecho mejor persona.

List of abbreviations

CF. Crystal Field

SOC. Spin-orbit coupling

SMM. Single Molecule Magnet

STM. Scanning tunneling microscopy

LDOS. Local density of states

STS. Scanning tunnelling spectroscopy

XAS. X-ray absorption spectroscopy

XMCD. X-ray magnetic circular dichroism

XNLD. X-ray natural linear dichroism

TEY. Total Electron Yield

arPLS. Asymmetrically Reweighted Penalized Least Square

UHV. Ultra-High Vacuum

LT-STM. Low Temperature Scanning Tunnelling Microscopy

LN$_2$. Liquid Nitrogen

LHe. Liquid Helium

PBN. Pyrolytic Boron Nitride

OMBE. Organic Molecule Beam Epitaxy

QCM. Quartz Crystal Microbalance

Gr. Graphene

LEED. Low Energy Electron Diffraction

QMS. Quadrupole Mass Spectrometer

HECTOR. High Field Vector Magnet

RT. room temperature

TDA. p-terphenyl-4,4′-dicarboxylic acid

PDOS. Projected local density of states

ML. monolayer

TPA. benzene-1,4-dicarboxylic acid

DPBP. 1,4-bis(4-pyridyl)-biphenyl

LUMO. Lowest Unoccupied Molecular Orbital

HOMO. Highest Occupied Molecular Orbital

NI. Normal Incidence

GI. Grazing Incidence

h-BN. Hexagonal Boron Nitride

BCNB. (1,3,5-tris(40-biphenyl-400-carbonitrile) benzene

RT. Room Temperature

CVD. Chemical Vapour Deposition

List of Figures

List of tables

Contents

1. Introduction

During the last decades, we are witnessing a progressive miniaturization of electronic circuits and information storage units. Nowadays, technology is characterized by its portability, which allows to possess highly complex pieces of technology compressed in the palm of the hand. However, at the end, there will be a physical limit to such miniaturization, which would be the size of an atom. Atoms are postulated as the smallest structures able to be employed as electronic and magnetic components in circuitry. In this sense, one of the most urgent challenges to be solved in nanoscience is the development of nanodevices that take advantage of the electronic and magnetic properties of molecular and atomic nanostructures. Nevertheless, the employment of atoms is still elusive, due to its high complex and scientific uncharted behaviour. Herein, in order to design the smallest imaginable units of circuitry, it is mandatory to fully understand the properties of atoms and their relation to the chemical environment.

One of the most desired futuristic applications is the employment of atoms as the smallest data information storage units. There are two main requirements that an atom needs to satisfy to behave as a single atom magnet[1].

1) It needs a doubly degenerated ground state. This first condition is essential, since it determines the existence of two magnetic states separated by a thermal barrier driven by magnetic anisotropy. Thus, once the quantum system is set in one magnetic state, it will keep the magnetic stability unless thermal or non-thermal processes quench such stability.
2) Large energy separation between the ground state and the first excited state. This condition is related to the stability of the magnetic moment. The lower the energy separation, the easier to quench the magnetic barrier.

On one hand, during last years, the employment of 3d metals have been extensively studied in a great variety of situations, reaching the limit of magnetic anisotropy for Co atoms deposited on top of MgO(100)[2]. However, the use of 3d metals for information storage at the ultimate size scale is jeopardized, since their orbital moments are usually quenched by the environment [2–4]. This phenomenon causes that the spin is the only source of magnetic behaviour of these elements. Only with a wise choice of the atom-environment configuration, in occasional circumstance the orbital moment can be preserved[2,5,6]. To solve this difficulty, plenty of effort has been put into the synthesis of metal-oxo clusters structures[7]. This kind of structures belongs to the family of the so called Single Molecule Magnets (SMMs) which consist in molecules complexes embedding transition metal clusters coordinated by oxygen atoms in a specific geometry[8–13]. The wise idea behind these structures is to take advantage of the exchange coupling to craft molecular species presenting a large spin state and magnetic anisotropy.

However, in general, the lack of geometric control produces molecules with large spin values not acting as SMMs due to the absence of axial magnetic anisotropy[7].

On the other hand, lanthanide elements naturally overcome the quenching of the orbital angular momentum. First, their electronic structure is characterized by the presence of valence electrons in 4f orbitals, which are internal. Such electronic configuration makes the valence electrons strongly shielded against interaction with the environment. Second, lanthanide elements display a strong spin-orbit coupling, which together with the preservation of the orbital angular momentum, leads to large magnetic anisotropy barriers[1,14,15]. Additionally, the anisotropy barrier can be tuned by an appropriate configuration of the environment (crystal field), making lanthanides appealing as candidates to be employed as single atom magnets or embedded as single molecule magnets.

In the following lines, the basics of atomic magnetism will be discussed. Then, the choice of lanthanides will be further explained. Additionally, coordination chemistry on surfaces will be introduced as a potential strategy to tune the magnetic anisotropy of lanthanides. Finally, the main goal of the thesis, which is to establish magnetic stability in lanthanide-directed networks, will be commented, together with an outline and a brief description of the contents of each chapter.

1.1 Atomic magnetism: requirements for single atom magnets

Due to the size scale of the atoms, their physical properties are described by quantum mechanics. In the classical world, the energy of a system is a continuous function, where the system can take any value in that domain. However, in quantum mechanics the rules are different. In the quantum world, the energy of a system is described by a set of discrete energy values, and the system just can take these values. The origin of the magnetic properties of an atom lies on the electrons of its valence shell. The occupancy of valence shell determines the value of the orbital angular moment (L) and the spin moment (S), according to Hund´s rules. The sum of these terms is the total magnetic moment J ($\vec{J} = \vec{L} + \vec{S}$).

Considering a free atom in gas phase, the system has no preferential direction for the magnetic moment, due to the rotational symmetry. This means that all discrete J values can be taken with equal probability (Figure 1-1a). To characterize the possible directions, the projection of J along an arbitrary axis of quantification is taken. The values of these projections are labelled as J_z. Considering the atom as a sphere, the ±Jz available values are degenerated. In consequence, the system has not magnetic anisotropy.

If this atom now faces the environment, for instance by being deposited on a substrate, there is an interaction between the electrons of the magnetic atom and such environment. Such interaction is described by the so-called crystal field (CF), which breaks the degeneration of the J_z levels, splitting them, resulting in a parabolic energy

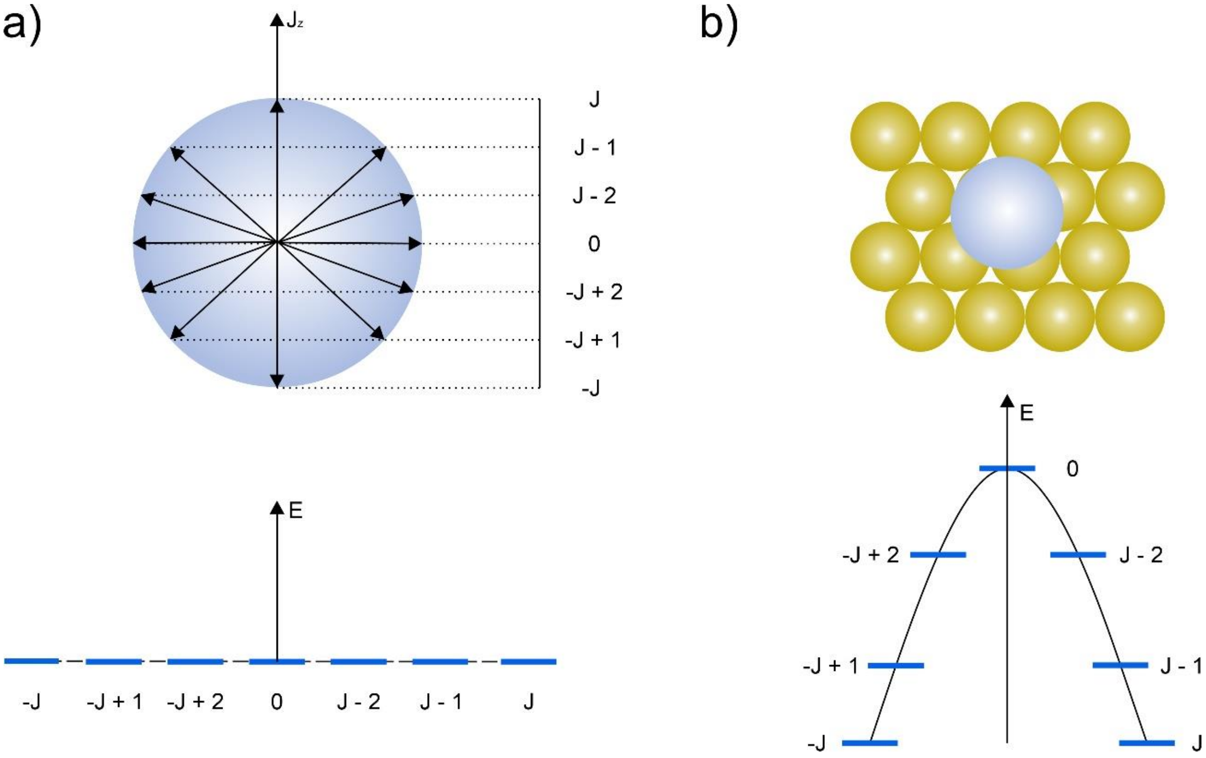

Figure 1-1 Magnetism of an atom.

a) J_z values allowed for the total magnetic moment J in a free atom. These values are the projection of the magnetic moment along an arbitrary axis of quantization. Since there is not any preferential direction, all the states are degenerated in energy and equally probable. b) Single atom on top of a surface. The presence of the substrate breaks the energy degeneracy of the states, generating the parabolic energy distribution.

distribution (Figure 1-1b)[1]. The energy difference between the ground state and the highest unoccupied state in energy is called the magnetic anisotropy energy. In the presence of a perfect uniaxial CF, the reversal of J_z would be produced by excitations from the ground state to upper states until reaching the highest energy unoccupied state, subsequently decaying into the reversed J_z ground state (Figure 1-2a). The energy for the magnetic excitations could be acquired from scattered electrons coming from the substrate, phonon interactions or thermal fluctuations. Nevertheless, a perfect uniaxial CF is not easy to achieve. Typically, the CF introduces transversal terms that produce the mixing of otherwise pure quantum states[16], which means that the eigenstates of the system are linear combinations of several J_z states. The mixing of these states gives rise to faster relaxation mechanisms, which at the end, is a reduction of the effective magnetic anisotropy energy. Examples of these mechanisms are depicted in Figure 1-2b. On the way to obtain single atom magnets, smart choices of the CF have to be taken. On one hand, the CF should be configured in such a way that the energy difference between the ground state and the first excited state would be as larger as possible. Following this strategy, the ground state is protected against spin transitions towards higher energy levels. On the other hand, a good election of the CF decreases the shortcuts for the electrons to tunnel through the anisotropy barrier [16,17]. Thus, an appropriate choice of the CF can boost the magnetic relaxation time of an atom.

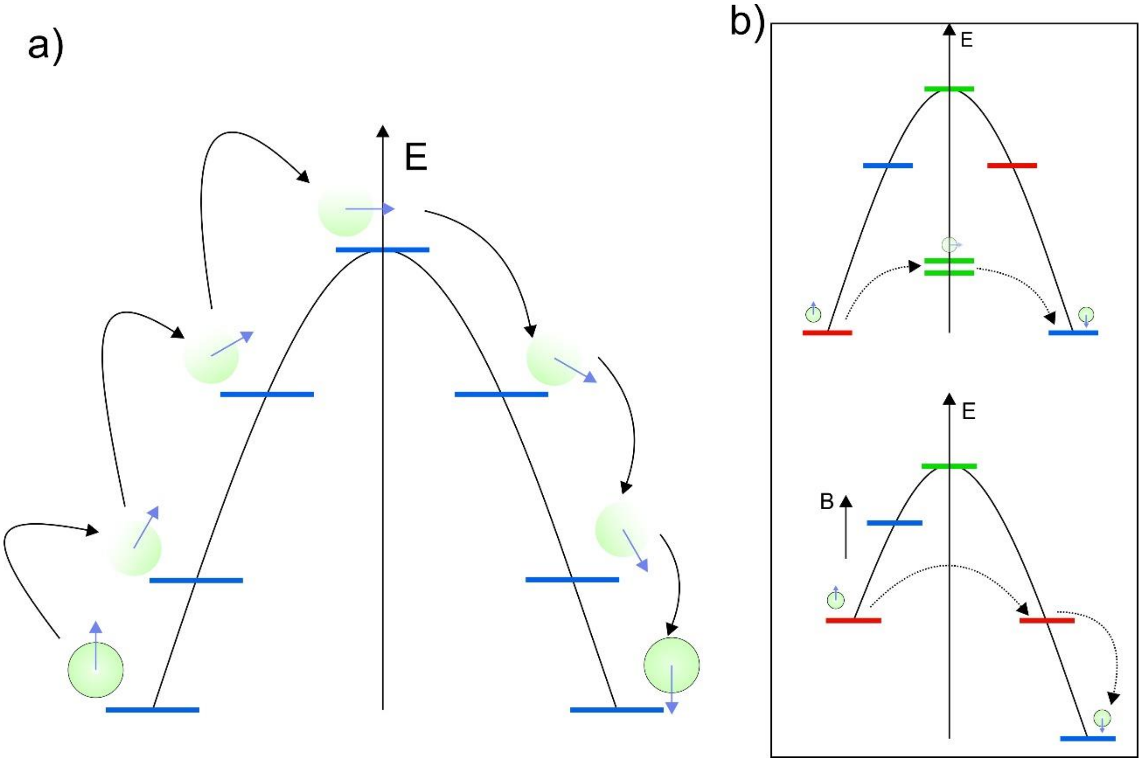

Figure 1-2 Magnetic moment relaxation mechanisms

a) In a perfectly uniaxial CF, the magnetic moment is reversed through spin excitations, requiring an energy equal to the anisotropy barrier. b) Relaxation mechanism for a non-perfect uniaxial CF. The distinct colours indicate mixed quantum states. Upper panel: Relaxation shortcut. The state can be reversed by tunnelling through J_z mixed states. As a result, the anisotropy barrier is lower. Lower panel: Quantum tunnelling of the magnetization. In the presence of a magnetic field, the energy states shift due to the Zeeman effect. Due to this shifting, mixed J_z states can coincide in energy, stablishing a shortcut for reversal of the magnetic moment.

1.2 Lanthanides in single atom magnetism

The discovery of lanthanide phthalocyanine double-decker sandwiches showed an unprecedent magnetic relaxation time in 2003. Since then, the use of lanthanides in single molecule and single atom magnets has been widely increased, both in wet chemistry [18–23] and in surface science [17,24–26].

Their unique magnetic characteristics are a consequence of their electronic and nuclear structure. On one hand, lanthanides are characterized by valence electrons in the 4f shell. These electrons are strongly protected from hybridization with the environment due to their inner character. Because of this, the orbital moment L cannot be quenched as in the case of 3d metals. On the other hand, since they are heavy elements, lanthanides present a strong spin-orbit coupling (SOC) and must be described by the total quantum number J, with a 2J + 1 degeneracy. As a result, lanthanides typically result in higher magnetic moments and much larger magnetic anisotropy barriers than their 3d-metal counterparts. Importantly, the CF for these elements is considered a perturbation, which breaks the degeneracy of J.

When lanthanides are coordinated with molecules, either forming metal-organic complexes or coordination networks, their oxidation state is usually +3 (Ln^{3+}) [18–23,27–29]. Notably, some of the lanthanide metals are naturally more suitable to be employed as magnetic building blocks than others. As it has been previously stated, one of the requirements to get single atom magnets is to achieve a double degenerated bistable ground state. Such ground state will be described by $|J, J_z>$. Of course, to satisfy this condition, the ground state cannot be the superposition of distinct J_z levels, but just a pure J_z. Otherwise, the spin direction will be perpetually fluctuating, and no magnetic behaviour will be observed. One way to protect the ground state is an appropriate CF to avoid the mixing (superposition). Alternatively, there are lanthanide ions that have odd number of electrons in their valence shells, (Gd^{3+} ($4f^7$), Dy^{3+} ($4f^9$) or Yb^{3+} ($4f^{13}$) to name some) and by virtue of the Kramers theorem[16,30] they exhibit a doubly degenerated ground state.

To take advantage of the magnetic properties of lanthanide ions, a clever election of the CF is mandatory. Here, it is important to notice that there is a strong relation between the shape of the electronic charge and the J quantum number. The charge of +3 ions can present three distinct shapes with respect to the symmetry axis: oblate (charge is equatorially elongated), isotropic (spherical charge) and prolate (charge is axially elongated), as illustrated in Figure 1-3a. In principle a good chemical design should target to stabilize the maximum J_z, trying to minimize the repulsion between the electronic cloud of the metal and the ligand. Thus, sandwich-like CFs maximizes the magnetic anisotropy for oblate ions with the highest out of plane magnetic moments, like in the case of $TbPc_2$ or $DyPc_2$ [31–34] (Figure 1-3b). On the other hand, equatorial CF increments the anisotropy for prolate ions with the highest in-plane magnetic moments[18,19,23] (Figure 1-3c). If the crystal field is not properly engineered, then the lanthanide element will simply adapt the electronic cloud to minimize the repulsion, lowering the magnetic moment J_z in the process.

Along this thesis, two lanthanides have been employed, Dy and Er. Their use is justified by two fundamental reasons:

1) Both are Kramer ions (Dy^{3+} [$4f^9$] and Er^{3+} [$4f^{11}$]), which ensures a doubly degenerated bistable ground state regardless the CF.
2) Dy^{3+} is representative for oblate ions with maximum out of plane J_z, whereas Er^{3+} is an archetype for prolate ions with maximum in-plane J_z.

1.3 Coordination chemistry as a tool to tailor the crystal field

Coordination chemistry deals with the bonding between organic ligand and metallic atoms to afford molecular complexes and nanostructures, including bidimensional and tridimensional frameworks. During last decades, metallosupramolecular synthetic protocols, originally coming from wet chemistry, have been exported to surfaces, mostly employing 3d elements, giving rise to a large plethora of surface-confined metal-organic

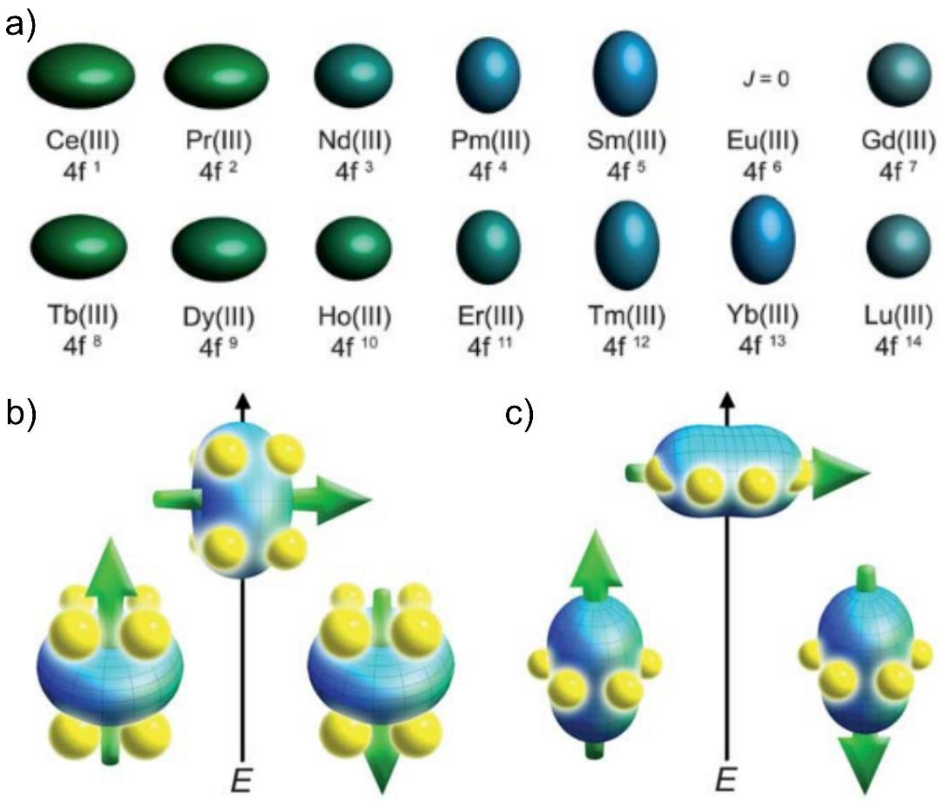

Figure 1-34f electron distribution for lanthanides on their trivalent states and optimized CF depending on the charge distribution of the J states.

a) Quadrupole approximations of the 4-f shell electron distribution of the distinct lanthanide ions. b) Optimized CF for oblate ions. In this case, the CF should trap the ion charge in a sandwich-like structure to stabilize the highest magnetic moment, which points along the short charge symmetry axis. c) Optimized CF for prolate ions. In this case, the best option is an equatorial CF. Figure adapted from the work of D. Rinehart and R. Long[1].

networks [35,36,45,46,37–44](Figure 1-4 a-c). Recently, such strategy was also exploited making use of lanthanides, a field in which our group is a pioneer[27,47–50] (Figure 1-4 d-f).

The structure of the final nanomaterial to be formed depends on the balance between the metal-molecule, intermolecular and network-substrate interactions. Such balance can be tailored by controlling the substrate temperature, the evaporation rates of the organic ligands and metallic atoms, or by increasing the coverage of adsorbates on the surface[46].

The development of the field has led to the development of surface-confined coordination networks featuring unique interesting electronic, magnetic and optical properties by exploiting the synergy between organic building blocks and metal atoms.

The variety of organic ligands based on distinct backbones and functional groups, allows the availability of distinct crystal fields, which could be employed to maximize the magnetic anisotropy of lanthanide ions.

In this thesis, coordination chemistry on surface is used to design metallosupramolecular architectures directed by lanthanides on surfaces.

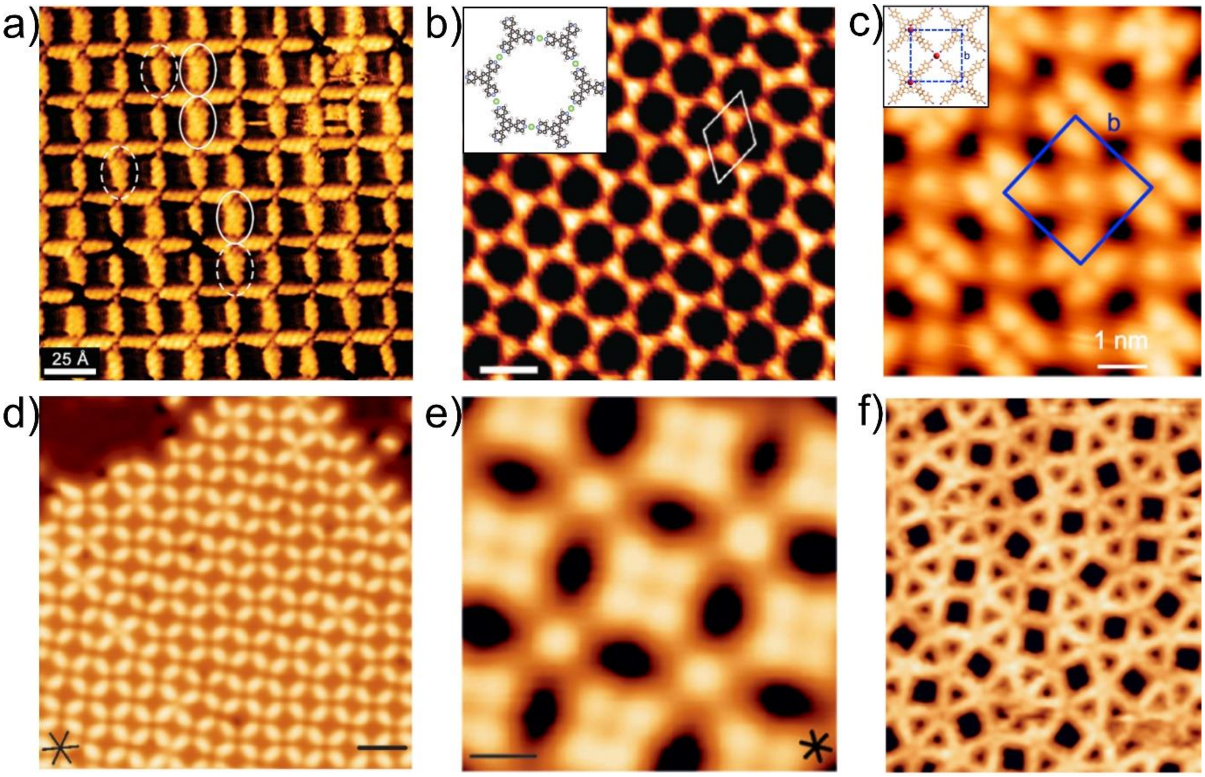

Figure 1-4 Examples of surface-confined coordination networks employing 3d and 4f metals.

a,b,c) Metallosupramollecular networks driven by coordination with 3d metals as: (a) Fe, (b) Cu or (c) Co on different substrates. d,e,f) Metal-organic structures based on lanthanide coordination. d, e) Gd atoms coordinated with (d)carboxylate and (e)carbonitrile groups. f) Eu-directed metallosupramolecular quasicrystal on Au(111) by coordination with linear ligands equipped with terminal carbonitrile groups. Images adapted from references [44,43,42,27,49 and 48] respectively.

1.4 Goals and out-line of the thesis

The objectives pursued during the realization of this thesis have been:

- To validate the coordination chemistry strategy as a mechanism to tune and increase the magnetic anisotropy of lanthanide ions in coordinative environments.
- To determine how the election of oblate and prolate ions impacts in the synthesis of on-surface metal-organic networks, as well as in the resulting structural, electronic and magnetic properties.
- To design lanthanide-directed networks both on metals and sp^2 supports.
- To assess the feasibility of observing single atom magnetism on metallosupramolecular architectures grown on metals.

The thesis is organized as follow:

In chapter 2, the basic principles of the different experimental techniques used in the thesis are explained. Some details about their theoretical fundaments are given, as well as how to analyse the obtained data. Additionally, the experimental set-up employed during the realization of the experiments is described, together with an explanation of the protocols to clean and prepare the samples.

In chapter 3, the structural, electronic, and magnetic properties of Dy-directed carboxylate metallosupramolecular architectures on Cu(111) are studied, by exploiting the coordination between ditopic linear organic linkers equipped with terminal carboxylate moieties and Dy. The ionic nature of the coordinative bond is addressed by DFT, despite a small covalent contribution is observed in the experiments. Magnetic properties are characterized by means of XAS, XNLD and XMCD, revealing an increment of the magnetic anisotropy of the Dy upon coordination. The easy axis of the magnetization is close to the surface. The employment of a shorter linear ligand attached to the same carboxylate groups produces a related reticular lattice with a reduced internodal distance. The easy axis of the magnetization lies closer to the surface compared with the network directed by the longer linker and the magnetic anisotropy is increased, which reveals the importance of the CF.

In chapter 4, the synthesis of Dy-directed dinuclear coordination networks on Au(111) is studied. The molecular linkers feature a linear backbone with pyridyl groups at its termini. The deposition of a submonolayer coverage of the linkers, followed by dosage of Dy, affords a Kagome metallosupramolecular network. An increment of the amount of molecules and metal atoms, while preserving the lanthanide:molecule stoichiometry, gives rise to the formation of a coordination network featuring a rhombic pattern. The electronic properties of both networks are addressed by STS, preserving the alignment of the electronic states. The characterization of the magnetic properties reveals that both structures show an easy axis of the magnetization close the plane of the surface. Substitution of Dy by Er atoms in the synthesis procedure results in identical coordination networks. The Er atoms realign the energy level alignment of the frontier orbitals when compared to the Dy-directed architectures. The charge distribution of the Er ions is inverted with respect to the orientation of the charge of Dy ions, as it determined by XNLD. XMCD measurements show a strong enhancement of the magnetic anisotropy in Dy networks versus Er ones. Finally, multiplet calculations compared with experimental findings reveal a tilting of the easy axis of Er (50° from normal incidence).

In chapter 5, the feasibility of designing Dy-directed metal-organic coordination networks on Gr/Ir(111) is explored. Six distinct molecular species equipped with either carbonitrile or pyridyl functional groups are explored. Success is achieved by using a 3-fold symmetric ligand with terminal carbonitrile groups. The metal-organic architecture is first grown on Au(111), producing a quasi-hexagonal lattice based on 4-fold Au-directed nodes, and 5-fold mononuclear and 6-fold binuclear Dy-directed nodes. Following the same protocol an equivalent network is obtained on Gr/Ir(111), but lacking the four-fold nodes associated to coordination with Au adatoms. Such results open new avenues for the synthesis of lanthanide-directed architectures on sp2 templates.

Finally, chapter 6 contains a summary of the main conclusions obtained along the thesis, as well as perspectives on the future of the field.

2. Theoretical fundaments and experimental techniques

In this chapter, the theoretical fundaments of the experimental techniques used in this thesis, as well as a technical description of the labs are detailed. First, the theory of scanning tunnelling microscopy is introduced. Next, the principles of XAS, XMCD and XNLD are explained, as well as its data processing. Herein, the acquisition of magnetization curves is described, as well as the sum rules to interpret the information from photoelectron adsorption spectroscopies. Finally, the experimental set-ups are described. The experiments have been performed in a customized UHV system hosting an Omicron LT-STM at IMDEA Nanoscience and at the Boreas beamline at ALBA synchrotron.

2.1 Scanning tunnelling microscopy (STM)

The core technique of the experiments shown in this thesis is the STM. Developed in 1981 by H. Roher and G. Binnig, this technique marked a revolution in the surface science field. STM allows to explore surfaces with atomic resolution. Combined with additional surface techniques, it is a highly versatile tool to explore physical and chemical properties of distinct kinds of samples, like thin films [51–55], individual atoms [56–60], molecules [61–65] or polymers [66–70]. The STM is a microscope that makes use of the tunnelling effect between a rastering tip and a surface. By means of such effect, the electrons from the tip can go through the vacuum barrier to the sample (or vice versa) upon application of a tip-bias voltage, thus establishing a tunnelling current, which is exponentially proportional to the distance from the tip to the sample, as it will be discussed later. The tip is attached to a piezoelectric tube that rasters the tip along the substrate with sub-nanometre precision. Typically, during measurements, the tip-sample distance is controlled by a feedback system, which maintains the tunnelling current, and thus the tunnelling gap, preventing the tip to crash or move too far away from the sample (Figure 2-1a). As the tip rasters the surface, the vertical movement of the piezos (Z) to maintain the tunnelling current is recorded, and then plotted in a 3D graph, which are the STM images, being X and Y the positions on the sample (top view), and Z the intensity of the plot.

2.1.1 Modes of operation

The STM offers two scanning modes:

- Constant current mode: During measurements, a current setpoint is chosen. Then, the feedback loop approaches or retracts the tip from the sample to establish and maintain the selected current. When the tip is rastering the sample, the feedback loop measures in every point the tunnelling current. If the current deviates from

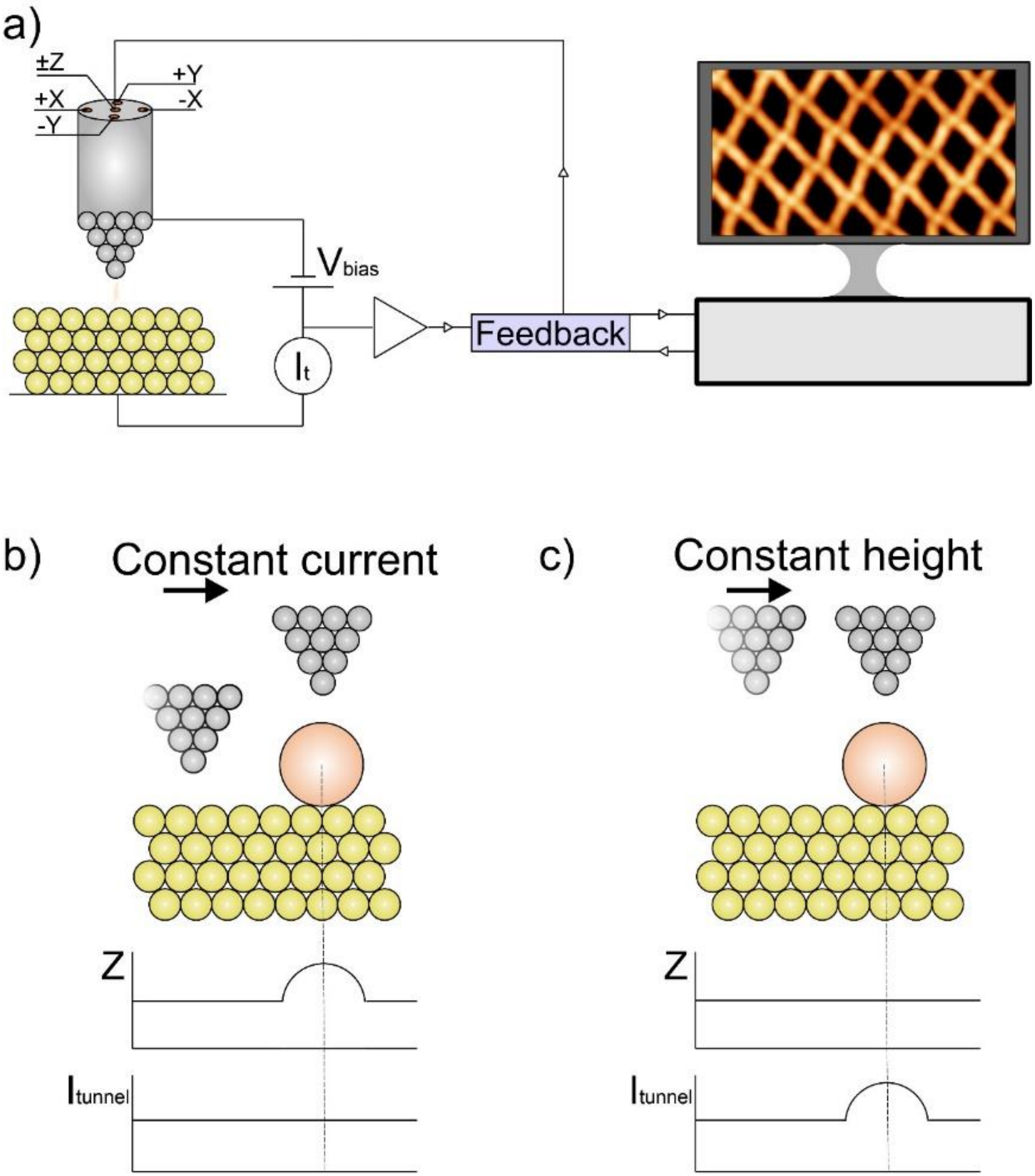

Figure 2-1 Scheme of working principle and modes of operation of an STM.

a) Scheme showing how an STM works. b) Scheme of constant current mode, in which the feedback is on, maintaining constant the tunneling current, while changing tip-sample distance. c) Scheme of constant height mode, in which the feedback loop is off.

the setpoint value, the feedback loop sends a signal to the piezoelectric to approach or retract the tip until the current matches the setpoint value. Since the current is related to the tip-sample distance, the piezo movements are recorded and used to generate an image (Figure 2-1b). When the measured current decreases from the setpoint value, the tip is considered too far away from the sample, so the feedback commands the piezo tube to approach the tip. On the contrary, if the measured current is higher than the setpoint, the feedback interprets that the tip is too close to the surface and the tip is retracted. Measurements in this mode are safe for the integrity of the tip and the sample, since the feedback loop takes care of avoiding crashing.

- Constant height mode: The feedback loop is off. Prior to scanning, a tip-sample distance is selected. Since the feedback loop is opened, the established current between the tip and the sample depends on the chosen distance. While scanning, the tip moves over the surface without approaching or retracting from the sample, preserving the vertical position (Figure 2-1c). When the tip moves along some protrusion, the tip-sample distance is shorter, which augments the current value. On the contrary, if the tip crosses over some kind of depression, like a defect in the atomic lattice, the current is decreased. These current changes are tracked and used to generate a 3D image, in which the Z values are the changes of tunnelling current. Since the measurements in this mode are performed with the feedback loop opened, the scanning should be done in regions where the surface is as flat as possible. Otherwise, the tip could crash against the sample.

2.1.2 Quantum tunnelling effect

The working principle behind the STM is the quantum tunnelling effect, which is a quantum phenomenon that describes the possibility for a wavefunction (particle) to propagate across a potential barrier.

Such effect is not seen in classical mechanics. The energy of a classical particle moving in a 1D potential $U(x)$ is defined as:

$$E = \frac{p^2}{2m} + U(x) \tag{2. 1}$$

In this scenario, if the energy of the particle satisfies $E > U(x)$, the particle can go through the energy barrier decreasing its kinetic energy proportionally to the magnitude of the potential. On the contrary, if the energy of the particle is not enough $E < U(x)$, the particle cannot overcome the barrier, since its kinetic energy term $\frac{p^2}{2m}$ can not be negative. In this case, the particle is confined and cannot escape from the potential well (Figure 2-2a). This is the well known classical picture, which can be daily observed.

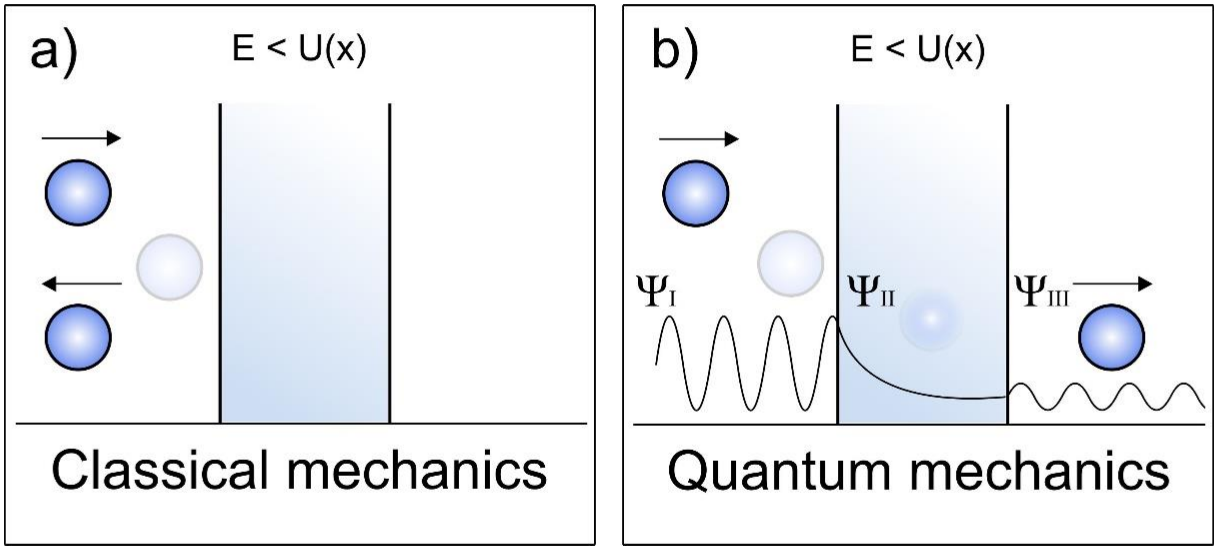

Figure 2-2 Scheme of a particle travelling through a potential barrier in classical and quantum mechanics.

a) In classical mechanics, the particle has not enough energy to go through the barrier, travelling in the opposite direction by momentum conservation. b) In quantum mechanics, the particle is described by its wave function. Inside the barrier, the probability to find the particle decays exponentially. The probability to find the particle at the other side of the barrier is proportional to its width. As a result, the quantum particle is able to cross the barrier.

But in quantum mechanics, the wave-particle duality states that every particle or quantum entity may be described as either a particle or a wave. Thus, in this framework, the particles are not described by a position x anymore, but by wavefunctions $\psi(x)$, and thus, there is always a probability of finding such a particle in a position x.

A quantum particle moving in a 1D potential is described by the time-independent Schrodinger equation:

$$E\psi(x) = \left(-\frac{\hbar^2}{2m}\frac{d^2}{dx^2} + U(x)\right)\psi(x) \tag{2.2}$$

Considering the potential described in Figure 2-2b and $E < U(x)$, there are three different solutions for the Schrodinger equation attending to the different regions:

$$\psi(x) = \begin{cases} \psi_1(x) = Ae^{ik_1x} + Be^{-ik_1x} \\ \psi_2(x) = Ce^{-k_2x} + De^{k_2x} \\ \psi_3(x) = Ee^{ik_1x} \end{cases} \tag{2.3}$$

The solution in the first region consists of a planar wave travelling towards the energy barrier with a certain amplitude (Ae^{ik_1x}) and the reflected wave travelling in the opposite direction (Be^{-ik_1x}).

Inside the potential barrier, the solution is an evanescent wave that decays exponentially. This means that though the particle has not enough energy, it has some probability to be found inside the barrier, decreasing when going deeper into it.

Finally, when the particle crosses the barrier, it continues as a planar wave. Since there is no additional barrier, there is not further reflection.

The terms k_1 and k_2 are the wave numbers, and they are related to the particle energy to the equations:

$$k_1 = \sqrt{\frac{2mE}{\hbar}} \ ; \ k_2 = \sqrt{\frac{2m(U_0 - E)}{\hbar}} \tag{2. 4}$$

where U_0 is the energy of the barrier. Of course, since the probability of finding the particle in the classically forbidden region decays exponentially, the energy barrier cannot be too wide, otherwise the electrons could not go through. In analogy, in an STM, the vacuum between the tip and sample is the barrier. Such tip-sample distance should be short enough to allow the electrons to travel from the tip to the sample or vice versa.

2.1.3 The tunnel junction: Tersoff and Hamann model

In order to realistically describe the tunnelling junction, a model was introduced by Tersoff and Hamann in 1985 [71]. This model takes the formalism proposed by Bardeen [72] to express the tunnelling current in first order perturbation theory as:

$$I_t = \frac{2\pi e}{\hbar} \sum_{t,s} f(E_t)[1 - f(E_s + eV_{bias})] \left|M_{t,s}\right|^2 \delta(E_t - E_s) \tag{2. 5}$$

where $f(E)$ is the Fermi distribution, V_{bias} is the applied voltage to the sample, E_t and E_s are the energies corresponding to the states of the tip and of the sample, respectively, and $M_{t,s}$ is the tunnelling matrix between the states of the tip and the surface. Considering low temperatures and small bias voltages, the equation can be rewritten as:

$$I_t = \frac{2\pi}{\hbar} e^2 V_{bias} \sum_{t,s} \left|M_{t,s}\right|^2 \delta(E_t - E_F) \delta(E_s - E_F), \tag{2. 6}$$

where E_F is the energy of the Fermi level. The most problematic term in equation (2.6) is $\left|M_{t,s}\right|^2$. To simplify this term, it is possible to consider the tip as a point probe, a simplification by which the matrix elements become proportional to the density of states of the surface ϕ_s placed at the position $\vec{r_0}$ of the probe, thus simplifying equation (2.6) into:

$$I_t \propto V_{bias} \sum_s |\varphi_s(\vec{r_0})|^2 \delta(E_s - E_F) \tag{2.7}$$

Here, the sum represents the definition of the local density of states (LDOS, ρ_s) of the sample evaluated at $\vec{r_0}$ at the Fermi level E_F:

$$\rho_s(\vec{r_0}, E_F) \equiv \sum_s |\varphi_s(\vec{r_0})|^2 \delta(E_s - E_F) \tag{2.8}$$

Equation (2.7) indicates that the tunnelling current is proportional to the bias applied and to the local density of states of the sample. Nevertheless, this description is not fully accurate, since a real tip has a certain shape. When Tersoff and Hamann developed this model, the microscopic structure of the tip had not yet been studied, so they considered the tip as a locally spherical potential well featuring a local radius R, with the centre of the tip positioned at a distance $\vec{r_0}$ from the sample being d the gap between the tip and the surface. Assuming such a simplification for the tip, the tunnelling current can be expressed like:

$$I_t \propto V_{bias}\, \rho_t(E_F)\, \rho_s(\vec{r_0}, E_F) e^{-2kR} \tag{2.9}$$

where k is a decay constant defined as $k = \sqrt{\frac{2m\phi}{\hbar}}$, and ϕ is the work function of both the tip and the sample (assumed equal). Introducing d (tip-sample distance) as $r_0 = R + d$ and considering that $\rho_s(\vec{r_0}, E_F) = \rho_s(0, E_F)\, e^{-2k(R+d)}$, equation (2.9) can be expressed as:

$$I_t \propto V_{bias}\, \rho_t(E_F)\, \rho_s(0, E_F) e^{-2kd} \tag{2.10}$$

Formula 2.10 gathers the main ingredients contributing to the tunnelling current. Importantly, such current is directly proportional to the bias voltage applied and to the

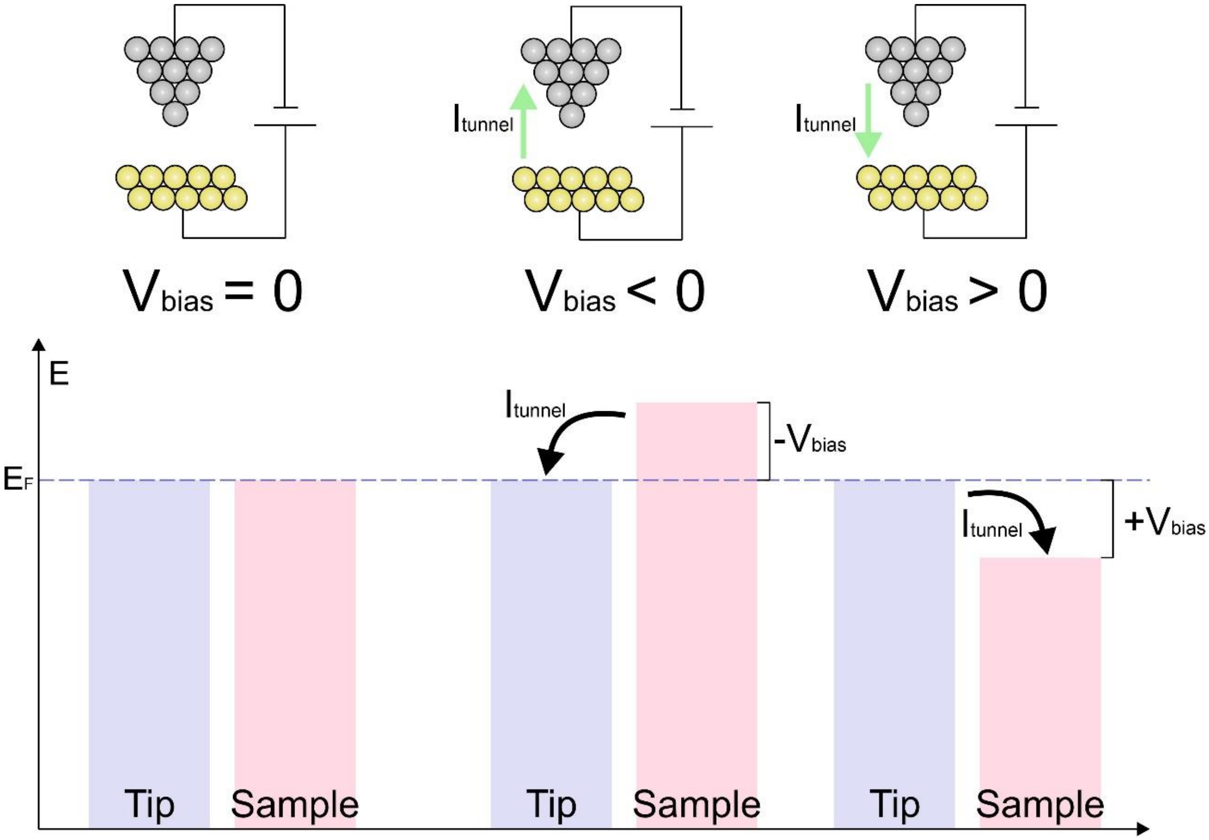

Figure 2-3 Effects of the bias voltage on the tunnelling current.

Left panel: when no voltage is applied, the Fermi levels of both tip and sample are equal, and no current is detected. Middle panel: when a negative bias is applied to the sample, its Fermi level shifts to higher energies, and electrons can flow from the sample to the tip. Right panel: if a positive bias is applied to the sample, its Fermi level decreases. The most energetic electrons from the tip can tunnel towards the sample.

density of states of the tip and the sample close to the Fermi level. In addition, it shows the exponential decay of the tunnelling current with the tip-sample distance d. Importantly, the relation between the density of states and the current means that the images are not just topographic, but a convolution between the topographic and the electronic properties of the materials under study. Thus, in general, STM imaging should be compared with theoretical modelling to assess for such electronic contributions.

The effects of the bias voltage V_{bias} on the tunnelling current are graphically represented in Figure 2-3. In this scheme, the work functions of the tip and the sample are assumed to be equal and the bias voltage is applied to the sample with the tip grounded. For a negative bias the Fermi level of the sample shifts toward higher energies, being now $E'_{FS} = E_F + eV_{bias}$. Thus, electrons can tunnel from the substrate to the tip. On the contrary, when a positive bias is applied to the sample, the Fermi level of the sample decreases $E'_{FS} = E_F - eV_{bias}$, and electrons can tunnel from the tip to the substrate.

2.1.4 Scanning tunnelling spectroscopy (STS)

In addition to its capabilities for imaging with supreme spatial resolution, STM can be used to get information about the electronic properties of the samples by means of STS.

As discussed above, the tunnelling current is proportional to the density of states of the sample. From equation 2.10, the derivative of the tunnelling current with respect to the bias voltage can be expressed as:

$$\left.\frac{dI_t}{dV}\right|_{V_{bias}} \propto \rho_s(eV_{bias})\rho_t(0) \qquad (2.11)$$

Thus, Equation 2.11 establishes a direct link between the magnitude dI/dV and the electronic states of the sample, assuming a constant value for the density of states of the tip.

Inspired in such link, scanning tunnelling spectroscopy is a technique used in a wide range of experiments to determine the surface states of metallic substrates [73–75], the electronic structure of 2D materials [76–78], to localize the frontier orbitals of molecules [79–81] or even to get access to some magnetic properties [82–84], among other uses. To perform the STS measurement, the tip is moved and stabilized to the point where the electronic properties are going to be inspected. Then, the feedback loop is open and the V_{bias} is varied in a ramp, tracking the current changes with the bias voltage. To obtain the dI/dV signal, there are two distinct methods:

i) First and direct method is to record I versus V_{bias} signal and mathematically obtain the derivative of I with respect to V_{bias}. This method seems easy since any programming software could compute this quantity. The problem with this procedure is given by the signal to noise ratio. In normal conditions, the currents measured in a STM experiment are in the range of pA or nA, so the obtained signals are weak and, in the integration time of a standard STS experiment, they show too much noise to allow a direct calculation of the derivative.

ii) The second method, used in this thesis, takes advantage of a lock-in amplifier to experimentally record the dI/dV signal, improving notably the signal to noise ratio when compared to the output of method 1.

The working principle of the lock-in amplifier in STS is based on the concept of the temporal correlation of the tunnelling current I(V) and a modulated V_{bias}.

The V_{bias} is plugged into the lock-in, where an additional AC signal (V_{ref}) is added, with an amplitude V_{mod}, frequency ω and phase α:

$$V_{ref}(t) = V_{mod}\sin(\omega t + \alpha) \tag{2. 12}$$

$$V_{ac}(V,t) = V_{bias} + V_{mod}\sin(\omega t) \tag{2. 13}$$

As a result, the tunnelling current is modulated by a sinusoidal oscillation. Since the modulation of the reference signal is small compared to the V_{bias}, typically 20mV or lower, the tunnelling current can be expanded in Taylor series around V_{bias} as:

$$\begin{aligned} I\big(V_{ac}(V,t)\big)\Big|_{V_{bias}} \approx I(V_{bias}) + \frac{dI(V_{bias})}{dV}V_{mod}\sin(\omega t) \\ + \frac{d^2I(V_{bias})}{dV^2}\frac{{V_{mod}}^2\sin(\omega t)^2}{2}\dots \end{aligned} \tag{2. 14}$$

In formula 2.14, higher terms of the Taylor expansion can be mathematically neglected, since V_{mod} << 1.

In the lock-in the current is amplified and converted to a voltage signal:

$$V_{sig} = GI(V,\omega,t) \tag{2. 15}$$

where G is an amplification constant with units $[V/A]$.

This signal is then multiplied by the reference one:

$$\begin{aligned} V_{sig}x\,V_{ref} = I(V_{bias})V_{mod}\sin(\omega t + \alpha) \\ + \frac{dI(V_{bias})}{dV}V_{mod}^2 sin^2(\omega t)\cos(\alpha) \\ + \frac{dI(V_{bias})}{dV}\frac{V_{mod}^2 sin(2\omega t)\sin(\alpha)}{2} \end{aligned} \tag{2. 16}$$

Finally, the output signal is obtained by the temporal correlation of this product:

$$
\begin{aligned}
V_{out} = \frac{1}{T}\int_0^T V_{sig} x\, V_{ref}\ dt \\
= \frac{1}{T}\Bigg(I(V_{bias})V_{mod}\int_0^T \sin\,(\omega t +\ \alpha)dt \\
+ \frac{dI(V_{bias})}{dV} V_{mod}^2 \cos(\alpha)\int_0^T sin^2(\omega t)dt \\
+ \frac{dI(V_{bias})}{dV}\frac{V_{mod}^2 \sin\,(\alpha)}{2}\int_0^T \sin\,(2\omega t)dt \Bigg)
\end{aligned}
\tag{2. 17}
$$

where T is the integration time of the signal. If this time is long enough (at least two times the period of the reference signal), the only term not cancelled is the corresponding to $sin^2(\omega t)$, thus given an output for the integral of:

$$
V_{out} = \frac{dI(V_{bias})}{dV}\frac{V_{mod}^2 \cos(\alpha)}{2} \tag{2. 18}
$$

By using this approach, the output signal from the lock-in is proportional to the derivative of the tunnelling current with respect to the modulated voltage. Finally, the output signal is driven through a low-pass filter, with a cut-off frequency of $\omega/2$. This way, all the contributions from signals at higher frequencies are removed, improving the signal to noise ratio. Notably, there is a term that depends on the phase, which can be tuned to maximize the signal.

In addition to point STS, the lock-in can be used to acquire dI/dV maps at selected V_{bias}, to observe the spatial distribution of electronic states [79,85,86]. To this aim, the tip rasters the surface at a given V_{bias}, being in each X, Y position the feedback loop open and the dI/dV signal at such bias measured. As a result, a 3D plot is given, in which the intensity at each X,Y position is the value of the measured dI/dV.

2.2 XAS, XMCD and XNLD spectroscopy

X-ray Absorption Spectroscopy (XAS), X-ray Magnetic Circular Dichroism (XMCD) and X-ray Natural Linear Dichroism (XNLD) are three of the most employed techniques on surfaces to characterize the electronic and magnetic properties of materials [24,87,88], since they are surface sensitive and element specific techniques.

XAS is typically used to obtain information about the coverage of the samples and the oxidation states of different elements. XMCD provides information about the magnetic moments of the samples, their magnetic anisotropy, as well as magnetic interactions.

XNLD is mostly used to provide information about the charge anisotropy, given information about the charge distribution of the elements inspected, though its dependence with the magnetic moment is used for detecting antiferromagnetism[89–91].

During XAS measurements, the energy of an incident X-ray beam is focused on a sample with certain angle of incidence and it is tuned to localize an electronic transition of the element under study. During the process, the photons of the beam can excite core electrons to the unoccupied states of the valence band provided they have the required energy. When this process happens, the photon is absorbed and the electron is excited, creating a hole in the core level. This hole is rapidly filled by electrons from higher energy levels, producing at the same time an Auger electron cascade, apart from the emission of photons and ions[92].

These Auger electrons are proportional to the amount of absorbed photons. Additionally, the Auger electrons produce the scattering of secondary electrons, which are detected as the Total Electron Yield (TEY). To measure the TEY, the most common methods are the use of a channeltron electron multiplier or to record the drain currents flowing from the ground to the sample to compensate the electron emission current[92].

The scattered electrons possess a finite kinetic energy. If they are placed in the bulk, this energy will be dissipated by inelastic scattering events. During this process, electrons can be deviated, losing energy before reaching the surface. In that case, the remaining energy will be lower than the work function of the material, and the electrons will be trapped. On the other hand, secondary electrons emitted close to the surface will have enough energy to overcome the work function, contributing to the signal. In consequence, this technique shows an extraordinary surface sensitivity, allowing to measure the signal coming from magnetic adatoms lying on a surface[93,94].

XMCD measurements are based on circularly polarized light, with two possible orientations, i.e. right- or left-handed. When a magnetic element is analysed, the photon absorption is different depending on the helicity of the beam. The process is described by a two-stage model [92]. In the first stage, the right- or left-handed circularly polarized light is used to excite the targeted core electrons. Depending on the helicity of the light and the spin configuration, the probability to excite electrons with spin up or spin down is different (Figure 2-4a). In the second stage, the applied magnetic field breaks the degeneracy of the valence band, producing more holes for one spin direction than for the other. The spin polarized electrons occupy one of the spin valence bands more than the other one, giving rise to the so-called dichroic signal (Figure 2-4b).

In XNLD, linearly polarized light is used to detect the charge anisotropy of the element studied in presence of a low magnetic field (0.05 T). The two orientations allowed are vertical and horizontal polarized light, and dichroic signal comes from the different number of valence holes between both directions. In addition, its employment under larger magnetic fields (5 T-6 T) can be used to detect antiferromagnetic behaviour due to

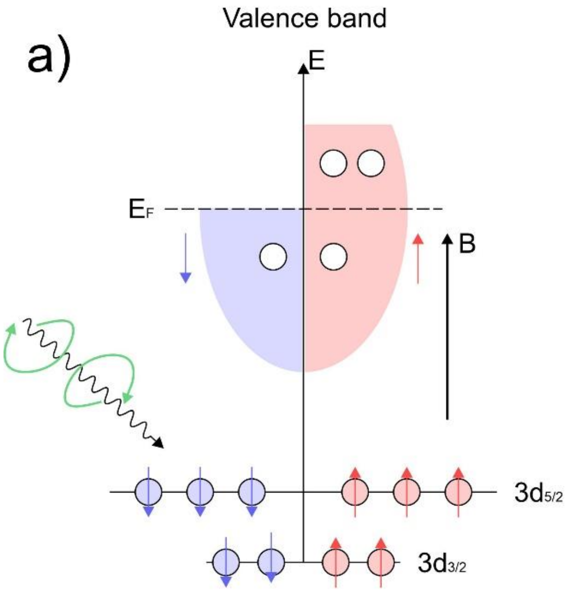

Figure 2-4 XMCD working principle

a) In the first stage, circularly polarized light with distinct helicity, in independent experiments, is used to excite electrons from the core levels. b) Due to the applied magnetic field, the number of unoccupied states for one spin direction increases with respect to the other orientation. As a result, there is a different x-ray absorption for the core levels, which produces the dichroic signal.

its dependence on the square of the magnetization $\langle M^2 \rangle$ [91]. In this case, the technique is renamed as X-Ray Magnetic Linear dichroism (XMLD).

These experiments should be performed in synchrotron facilities, since a high intensity X-ray light source is required, as well as the capability to polarize the light and to apply high magnetic fields (of the order of T).

Since the elements analysed in this thesis are lanthanides, their valence electrons are in the 4f orbitals. Thus, the discussion of the XAS and XMCD measurements will be restricted to the $M_{5,4}$ edges, which correspond to electronic transitions from 3d core levels to 4f unoccupied levels. XMCD measurements are typically performed in two different orientations of the sample with respect to the magnetic field, at 0° (Normal Incidence, NI) and at 70° (Grazing Incidence, GI). The comparison of both signals allow to determine the easy axis of magnetization of the samples. [93,95]. Furthermore, the values of the integrals of the XAS and XMCD curves can be used to quantitative determine the expected values of the magnetic moment per atom through the sum rules, as it will be discussed later.

The experiments have been performed applying a magnetic field of 6 T in the direction of the beam, holding the samples at a nominal temperature of 2 K, and in ultra-high vacuum conditions ($P < 1 \times 10^{-10}$ mbar), unless otherwise stated.

2.2.1 Magnetization curves

Magnetization curves in this thesis refer to the measurement of the variation of the highest XMCD peak of the M_5 edge with respect to the magnetic field. During such measurements, the system acquires the intensity of the M_5 compared to the intensity of the pre-edge for different values of the magnetic field, typically with a ramp rate of 2T/min. This process is performed several times from positive to negative values of the magnetic field in order to average the signal and to determine if the behaviour is symmetric.

Our interest in the magnetization curves lies in confirming the magnetic anisotropy, as well as the easy axis of magnetization. Importantly, an opening of the hysteresis loop with remanence at zero magnetic field would indicate single atom/molecule behaviour[17,26] or ferromagnetic coupling[96].

The speed of the ramp of the magnetic field can be varied. Low ramps increment the signal to noise ratio, resulting in cleaner signals. However, the observation of remanence depends on the temporal decay of the magnetic states. On one hand, if the relaxation time of the state is lower than the measurement time, it means that the orientation of the magnetic moment changes during the measurement. In this case, no magnetic remanence would be observed. On the other hand, high speed ramps imply noisier signals, but afford a higher temporal window to access to the magnetic properties, prior to decay.

2.2.2 Analysis of XAS, XNLD and XMCD data

The data obtained by XAS, XNLD and XMCD give important information, but it is necessary to properly analyse the samples to obtain an accurate and quantitative understanding of them.

When XAS curves are obtained, they show a structure that is a combination of the electronic transitions of the specific element targeted and a background signal. The background comes from the absorption spectrum of the surface and its contribution should be removed. In the measurements presented in this thesis, the background has been extracted by the computational Asymmetrically Reweighted Penalized Least Square (arPLS) method. The algorithm accurately detects the base line of the spectrum, which coincides with the background signal. This contribution is then removed (Figure 2-5). The details of the method are illustrated in reference [97].

The remaining signals are then normalized by the M_5-edge of the average XAS spectrum $\left(\frac{\mu_+ + \mu_-}{2}\right)$. The XMCD curve is also normalized by this quantity. Following this procedure, the effects of the coverage are suppressed and a comparison between samples of different coverages is feasible.

XNLD spectra are normalized by the M_5-edge of the isotropic spectra $\left(\frac{1}{3}\mu_V + \frac{2}{3}\mu_H\right)$.

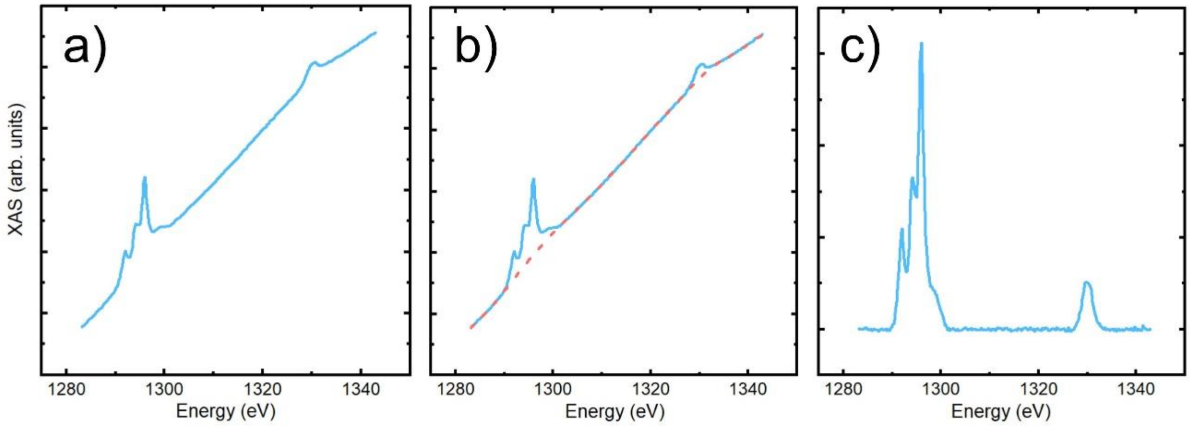

Figure 2-5 XAS background subtraction example.

a) Raw experimental XAS curve obtained for Dy in a metallosupramolecular architecture on Au(111). The signal is the combination of the peak structure of Dy together with the background signal coming from the substrate. b) The red dashed line corresponds to the baseline detected by arPLS. The algorithm excludes the peak structure during the detection. c) XAS spectrum with the background subtracted.

2.2.3 Sum rules

The normalized XAS and XMCD curves can be used to quantitative determine the expected values of the projected moments along the quantization axis. In particular, the values of $\langle L_z \rangle, \langle S_z \rangle$ and $\langle J_z \rangle$ can be obtained, as well as the total magnetic moment M_T of the elements of the sample. To compute these quantities, the famous sum rules are employed, which are a set of equations that relate the amounts described above with the values of the integrals of the XAS and XMCD normalized curves. They can be adapted for different electronic transitions and elements, which makes them a powerful tool to quantify the magnetic properties of a sample. In the following rules, the sum rules used for lanthanides will be derived.

The starting point is the work by P. Carra and co-workers in 1993 [98]. Herein, they establish the relation between the values of the integrals of the XAS and XMCD spectra with the electronic transitions of the element under study through the introduction of the variables ρ and δ:

$$\rho = \frac{\int_{M_5+M_4} dE\,(\mu^+ + \mu^-)}{\int_{M_5+M_4} dE\,(\mu^+ + \mu^- + \mu^0)} = \frac{1}{2}\frac{l(l+1)+2-c(c+1)}{l(l+1)n_h}\langle L_z \rangle \qquad (2.16)$$

$$
\begin{aligned}
\delta &= \frac{\int_{M_5} dE(\mu^+ - \mu^-) - \left[\frac{c+1}{c}\right] \int_{M_4} dE(\mu^+ - \mu^-)}{\int_{M_5+M_4} dE\,(\mu^+ + \mu^- + \mu^0)} \\
&= \frac{l(l+1) - 2 - c(c+1)}{3cn_h}\langle S_Z\rangle \\
&+ \frac{l(l+1)[l(l+1) + 2c(c+1) + 4] - 3(c-1)^2(c+2)^2}{6lc(l+1)n_h}\langle T_Z\rangle
\end{aligned}
\tag{2.18}
$$

Here, M5 and M4 subindexes represent integration along these edges. μ^+ and μ^- correspond to the XAS signals for right and left polarizations respectively and μ^0 is the spectrum of lineal polarization. The terms c and l correspond with the orbital moment of the core level and the valence band of the electronic transition studied. Since the transitions studied in the present thesis are $3d \longrightarrow 4f$, it is possible to specify $c = 2$ and $l = 3$. The term n_h represents the number of holes available in the valence band. In subsequent chapters, it will be shown that lanthanides are typically trivalent upon coordination. As a result, for Dy^{3+}, $n_h = 5$ and for Er^{3+}, $n_h = 3$. Finally, the term $\langle T_Z\rangle$ is the expected value of the magnetic dipole, which will be taken from literature.

To simplify these equations, the terms related with the electronic transitions are grouped in a set of variables called pre-factors and computed by the specific values given:

$$
preL_Z = \frac{1}{2}\frac{l(l+1) + 2 - c(c+1)}{l(l+1)n_h} = \frac{1}{3n_h} \tag{2. 17}
$$

$$
preS_Z = \frac{l(l+1) - 2 - c(c+1)}{3cn_h} = \frac{2}{3n_h} \tag{2. 18}
$$

$$
preT_Z = \frac{l(l+1)[l(l+1) + 2c(c+1) + 4] - 3(c-1)^2(c+2)^2}{6lc(l+1)n_h} = \frac{2}{n_h} \tag{2. 19}
$$

To continue, reference [99] introduces a new notation for the integral values that have been widely used in the literature when the sum rules have been employed:

$$p = \int_{M_5} dE(\mu^+ - \mu^-) \tag{2.20}$$

$$q = \int_{M_5 + M_4} dE(\mu^+ - \mu^-) \tag{2.21}$$

$$r = \int_{M_5 + M_4} \frac{\mu^+ + \mu^-}{2} \tag{2.22}$$

Additionally, it is introduced a simplification for the linear polarized spectra $\left(\mu^0 = \frac{\mu^+ + \mu^-}{2}\right)$. Thus, it is possible to rewrite ρ and δ parameters in these new terms:

$$\rho = \frac{\int_{M_5 + M_4} dE\,(\mu^+ + \mu^-)}{\int_{M_5 + M_4} dE\,(\mu^+ + \mu^- + \mu^0)} = \frac{q}{3r} = \frac{\langle L_z \rangle}{3n_h} \tag{2.23}$$

$$\begin{aligned} \delta &= \frac{\int_{M_5} dE(\mu^+ - \mu^-) - \left[\frac{c+1}{c}\right] \int_{M_4} dE(\mu^+ - \mu^-)}{\int_{M_5 + M_4} dE\,(\mu^+ + \mu^- + \mu^0)} \\ &= \frac{5p - 3q}{6r} = \frac{2}{3n_h}\langle S_Z \rangle + \frac{2}{n_h}\langle T_Z \rangle \end{aligned} \tag{2.24}$$

Reordering the terms to the right, it is obtained:

$$\langle L_Z \rangle = \frac{q}{r} n_h \tag{2. 25}$$

$$\langle S_Z \rangle = \frac{15p - 9q}{2r} n_h - 3\langle T_Z \rangle \tag{2. 26}$$

To compute the value of $\langle S_Z \rangle$, it is necessary to know the value of the dipolar term $\langle T_Z \rangle$. Instead, the ratio $\langle T_z \rangle / \langle S_z \rangle$ have been obtained from reference [99], being -0.053 for Dy^{3+} and +0.213 for Er^{3+}. Following this assumption, the expected values for $\langle L_Z \rangle$ and $\langle S_Z \rangle$ can be estimated.

Finally, the total momentum is by definition ($\langle J_Z \rangle = \langle L_Z \rangle + \langle S_Z \rangle$) and the total magnetic moment is $M_T = \langle L_Z \rangle + 2\langle S_Z \rangle$. In the following $\langle L_Z \rangle, \langle S_Z \rangle$ and $\langle J_Z \rangle$ are expressed in $\hbar$ units, whereas M_T is expressed in μ_B.

2.3 Experimental set-up

For the development of the experiments, appropriate ultra-high vacuum (UHV) systems are required. The experiments carried out in this thesis have been mainly performed in two distinct systems: a low temperature STM (LT-STM) placed in IMDEA Nanoscience, and the BOREAS beamline, at ALBA synchrotron.

2.3.1 The importance of UHV conditions

All the experiments presented in this thesis follow a common protocol: the deposition of different molecular species and metal atoms on top of some pristine substrates. In this context, the first issue to consider is that the substrate remains clean during the preparation of the samples and the time required to collect the data, which can last several days. For this purpose, it is mandatory to perform the experiments in UHV. In this sense, a substrate exposed to ambient conditions ($\sim 10^{3}$ mbar) will take just a few nanoseconds to be fully covered by contaminants coming from the environment. Even in vacuum conditions ($\sim 10^{-6}$ mbar), a substrate is still not well protected, since it will remain clean for just a few seconds [100]. Nevertheless, in UHV regime ($\sim 10^{-10}$ mbar), the surface needs tens of hours to be covered by a monolayer, assuming the worst scenario of a sticking coefficient of 1, which gives time to prepare and measure the sample. In this thesis, the measurements have been at $\sim 10^{-11}$ mbar, allowing to preserve samples during days.

2.3.2 The pumping system

To achieve and preserve UHV conditions, a set of pumps is constantly working. Each pump is necessary to achieve different ranges of vacuum:

- Primary pumps: The rough vacuum in the system is produced by a set of pumps composed by membrane pumps and a scroll pump. This mechanism allows to establish a first vacuum regime of the order of ~10^{-2} mbar.

- Turbo-molecular pump: This pump cannot operate at atmosphere conditions. A primary pump is connected to the exhaust of the turbo, and when the vacuum is in the range of ~10 mbar, the turbo can be started. This pump employs a set of angled blades rotating at high frequencies, which compresses the gases and send them out of the chamber through the exhaust. The vacuum level produced is around ~10^{-10} mbar.

- Ion pump: The residual gases of the chamber are ionized and accelerated towards Ti plates by a strong electric potential. Depending on the elements, these gases get embedded in the plates or release Ti gas that traps the rest of the gases in the walls. To start this pump, it is required a high vacuum level of the order of ~10^{-8} mbar. The vacuum produced by this pump is in the regime of low ~10^{-10} mbar. Importantly, since it does not have any mobile component, its use does not produce mechanical noise that could disturb the measurements. If necessary, both turbo and primary pumps can be switched off, provided the security valve between chamber and turbo is closed.

Additionally, a cold trap can be used to improve the vacuum. Such trap is simply a part of the system that can be refrigerated by cryogenic liquids, as nitrogen. Because of the lower temperatures of these parts, the contaminant particles condensate on the walls of these materials, reducing the pressure on the chamber, which can be used to gain time to prepare samples in cleaner conditions. The outer shield of the LT-STM in the analysis chamber acts as a cold trap when it is refilled by LN_2, reaching pressures in this chamber of the order of ~10^{-11} mbar.

Finally, once the pumps are up and running, in order to optimize the vacuum inside the UHV system, a bake out process is realized. The system is covered by heating tapes and wrapped in aluminium foil. Then, the tapes are turned on to warm up the system. The heating temperature depends on the components that are going to be heated. For the analysis chamber, where the STM is placed, the maximum allowed bake out temperature is 133 °C to avoid STM piezo damage. On the other hand, the bake out temperature in the preparation chamber can be set in a range from 150 °C top 200 °C.

2.3.3 Measuring UHV

To properly perform the experiments, it is required to be able to measure the quality of the vacuum. To this end, pressure gauges are placed inside of the UHV systems. In this thesis, two different types of gauges have been employed. Bayard-Alpert gauges have been used to monitor the vacuum level inside the preparation and the analysis chamber. These gauges are very precise, which make them suitable for controlling the pressure, but they need vacuum conditions to operate. On the other hand, full-range gauges have been employed to monitor the pressure in the load-lock chamber and in the Kentax evaporator. These gauges are not such precise as Bayard-Alpert, but they can work at atmospheric conditions and, thus, they are adequate to control the pressure in those parts of the system that could be face higher pressures.

2.3.4 LT-STM

For most of the experiments presented in this thesis, we employed an ultrahigh vacuum system hosting a LT-STM located at IMDEA Nanoscience (Figure 2-6). This system operates in UHV conditions and at cryogenic temperatures, making it ideal to grow and characterise metal-organic systems. It is composed by two different chambers, which are suitable for different purposes.

2.3.4.1 Preparation chamber

The preparation chamber is the part of the system where the samples are prepared. This chamber is equipped with all the necessary instrumentation for inserting substrates from air, cleaning them and preparing the different samples to be further studied in the STM (Figure 2-7a). The most important part of this chamber is the manipulator. It consists of a long bar that can be moved along 60cm ended in a head where there is a stage to hold the samples during the different operations. Substrates are single crystals of a metal (Au, Cu or Ir) welded to a molybdenum plate with tantalum foils (Figure 2-7c). The sample holders possess two small flanges that prevent the sample to fall into the chamber. When the sample is in the manipulator stage, it can be cleaned up or used for deposition of molecules or metals on top of it. In the following we will describe in detail the instrumentation employed for these purposes:

- Cleaning the substrate
  Cleaning of surfaces is the most important operation in the preparation chamber. To this aim, sputtering and annealing cycles of the crystals are performed. During sputtering, the chamber is filled with Ar gas until reaching a pressure of $\sim 10^{-6}$ mbar. Then, the gas is ionized and accelerated towards the sample by a strong electric potential in normal incidence by means of an ion gun. This process takes approximately 10 minutes and it is used to remove the contaminants in the upper layers. After sputtering, a subsequent annealing is performed. The manipulator

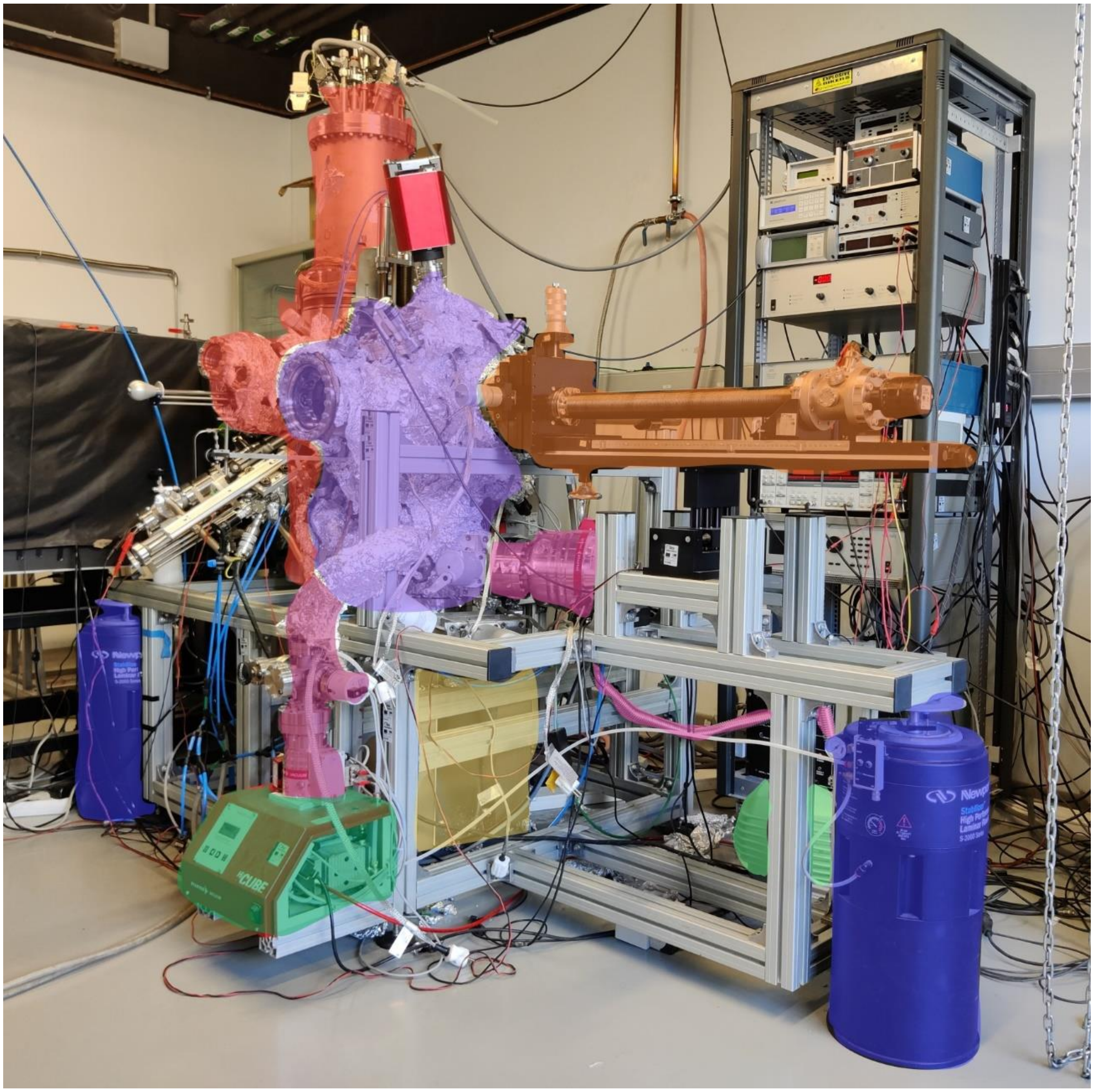

Figure 2-6 LT-STM set-up at IMDEA Nanoscience

Photograph of the experimental set-up at IMDEA. The different colors highlight the most important components. Red: Analysis chamber; Violet: Preparation chamber; Orange: Manipulator; Green: Primary pumps; Pink: Turbo-molecular pumps; Yellow: Ion pump; Blue: Pneumatic legs.

head can be equipped with two different heaters depending on the crystals to be cleaned. For coinage metals, a Pyrolytic Boron Nitride (PBN) head is used to heat the samples up to temperatures from 600 K to 700 K for 10 minutes (Figure 2-7b). In this case, the temperature is monitored by a type-K thermocouple placed in the sample stage. To prepare Ir(111) crystals prior to graphene growth, flash annealing at 1800 K is required. To achieve these temperatures, the PBN is substituted by a head that can stand high temperatures equipped with a filament. High voltage is applied to the sample and electrons ejected from the filament are accelerated towards the plate, heating the substrate. The temperature of the

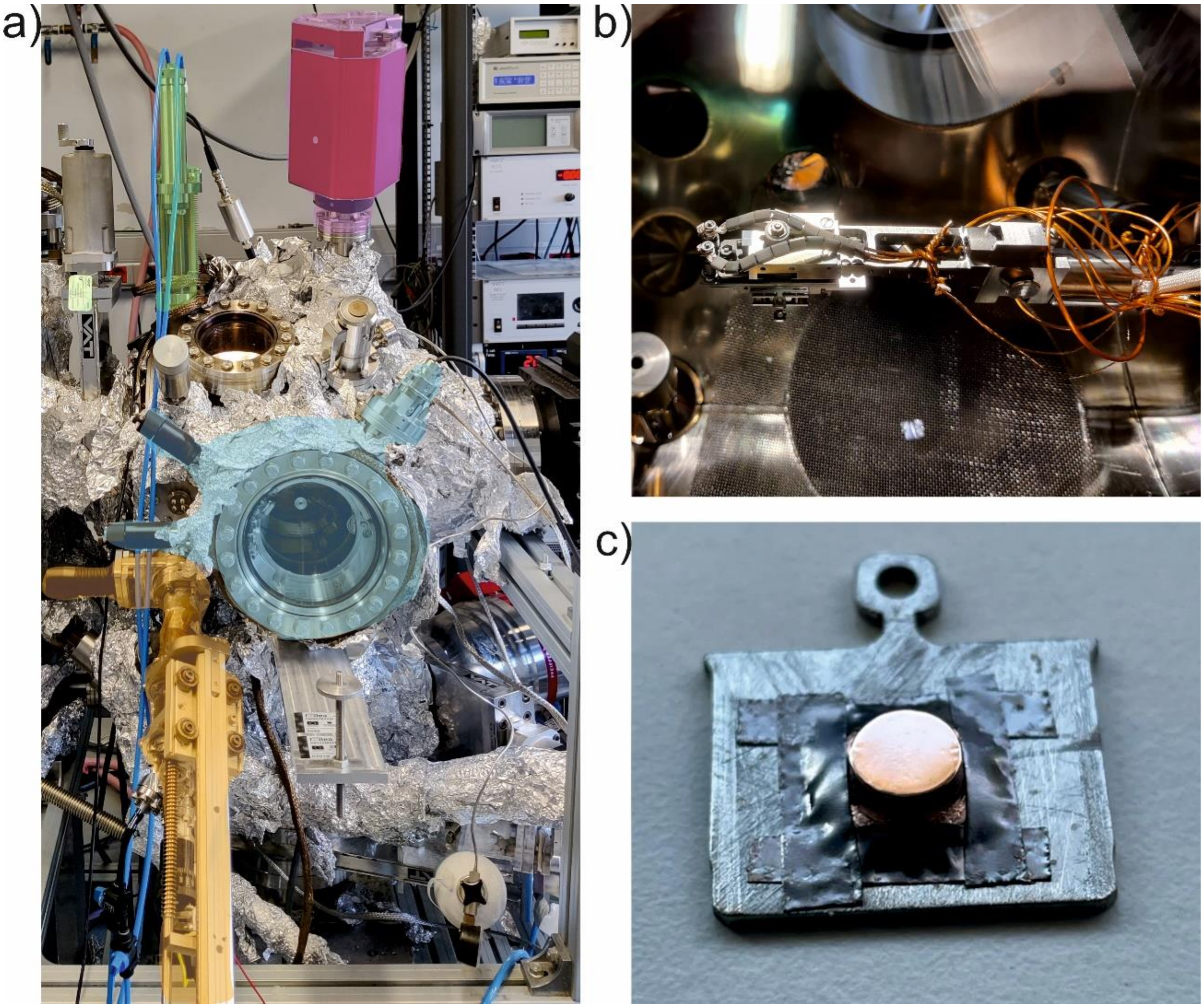

Figure 2-7 Components of the preparation chamber.

a) Photograph of the preparation chamber with the main components being highlighted. Green: Quartz Crystal Microbalance; Pink: Quadrupole Mass Spectrometer; Cyan: Low Energy Electron Diffraction; Yellow: Molecule evaporator. b) Manipulator head equipped with PBN heater. c) Cu(111) monocrystal on a molybdenum plate.

crystal is controlled by a properly calibrated pyrometer. These cycles are repeated as many times as it is required to obtain a clean surface.

- Molecule evaporator

  The deposition of molecules is performed by means of Organic Molecular Beam Epitaxy (OMBE) by employing a commercial Kentax TCE-BSC evaporator. The molecule powder is placed in crucibles out of vacuum and inserted in one of the available cells. Then, the evaporator is connected to a port of the preparation chamber and it is pumped through a pump station prior to be inserted. Following this protocol, the molecules to be deposited can be changed in the evaporator without breaking the vacuum. Once the evaporator is in vacuum, the molecules can be deposited by resistive heating.

- Metal evaporator

  To deposit metal atoms, we have employed a commercial Focus EFM3Ts evaporator. The metals to be deposited are rods that are placed in the cells of the evaporator. Once in vacuum, the rod is connected to a high voltage (1500 V) and the filament of the cell is turned on. The electrons coming from the filament are accelerated towards the metallic rod, transferring their kinetic energy to it. The rod starts to warm, and when the proper temperature is reached, metal atoms are sublimated from the rod and deposited on the substrate.

- Quartz Crystal Microbalance (QCM)

  The QCM is employed to discover the sublimation temperature of the molecular species and to calibrate the coverage. It consists of a quartz crystal that can oscillate at frequencies of the order of 6 MHz due to the piezoelectric effect. Nevertheless, the oscillation frequency is strongly sensitive to the mass of the crystal. When the crucible is heated at the deposition temperature, the molecules are sublimated into the chamber. When the molecules arrive to the QCM, they get attached to the quartz crystal, slightly increasing the mass and hence decreasing the oscillation frequency. This variation of frequency lets us stablish the sublimation temperature of the distinct molecular precursors. Because of the position of the metal evaporator, we cannot use the QCM to calibrate the amount of metal atoms.

- Quadrupole Mass Spectrometer

  During cleaning or deposition processes, a large amount of contaminants coming from the samples or from the instrumentation are released into the vacuum of the preparation chamber. To check that the vacuum is in good conditions, a Quadrupole Mass Spectrometer (QMS) is employed. The QMS gives us information about the composition of the residual gas in the chamber (Figure 2-8).

- Low Energy Electron Diffraction (LEED)

  To check the quality of the Gr or the crystals before STM, LEED is employed. During LEED, low energy electrons are directed towards the sample. Because of the interaction of these electrons with the surface, they are diffracted against a fluorescent screen, forming a diffraction pattern. The analysis of this pattern gives information about the crystallinity of the surface.

- Load-lock

  The preparation chamber is connected to a small chamber called load-lock, which is pumped by a primary and a turbo pump. Through this port, the substrates can be transferred from air to vacuum and vice versa without venting (exposing to air) the preparation chamber.

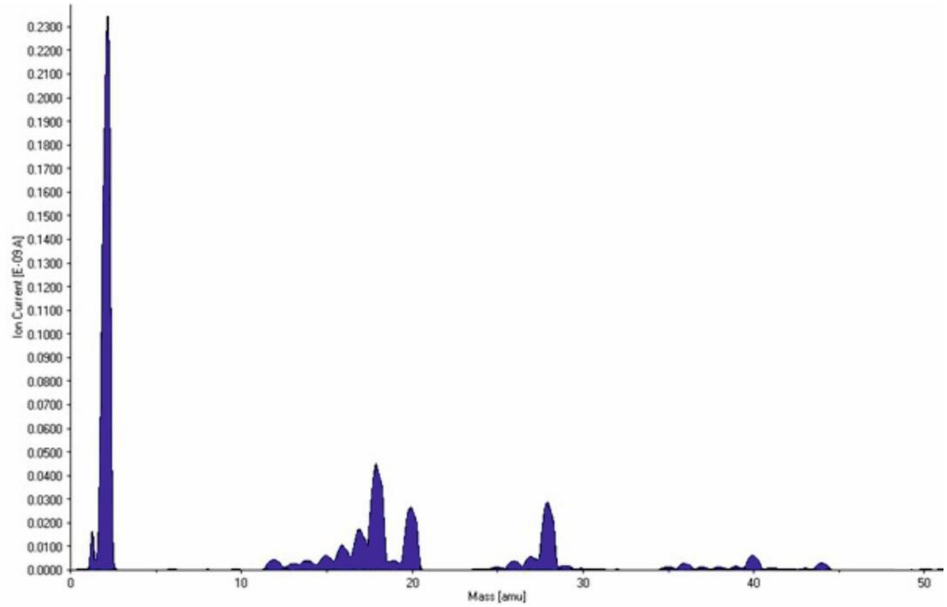

Figure 2-8 QMS spectrum of the preparation chamber.

The base pressure during the analysis was $2x10^{-10}$ mbar. The higher peak corresponds to presence of H_2, concomitant to the UHV. The peaks placed between 12 and 20 amu. are associated to different hydrocarbons, water to 18 and carbon monoxide to 28. No peak signal at 32 indicates the absence of leaks (oxygen) The low intensity of these peaks relative to the hydrogen is representative of a clean vacuum.

2.3.4.2 Analysis chamber

The purpose of this analysis chamber is the structural and electronic characterization of the samples by STM. To this end, the chamber hosts a commercial Omicron LT-STM that can operate at cryogenic temperatures. The main parts of this chamber are described in the following:

- Cryostats

  To be able to operate at low temperatures, the STM needs to be cooled down and both the sample and tip temperature need to be preserved during the experiment. Working at low temperatures is not mandatory, but it presents substantial advantages. At cryogenic temperatures, the diffusion of most of the adsorbates on the surface is severely diminished or stopped, making it easier to measure and to interpret the results. Additionally, the thermal drift of the system is strongly decreased. For this reason, the STM is equipped with two concentric cryostats (Figure 2-9a). The inner cryostat is in direct contact with the STM head and it is the one in charge of cooling down the STM to perform the experiments. This cryostat can be refilled both with LN_2 and with LHe, depending on the needs of the experiments. The outer cryostat covers the inner one and its purpose is the thermal protection of the cryogenic liquid in the inner cryostat. This cryostat is filled with LN_2, reducing the fast evaporation of the LHe. Both cryostats have

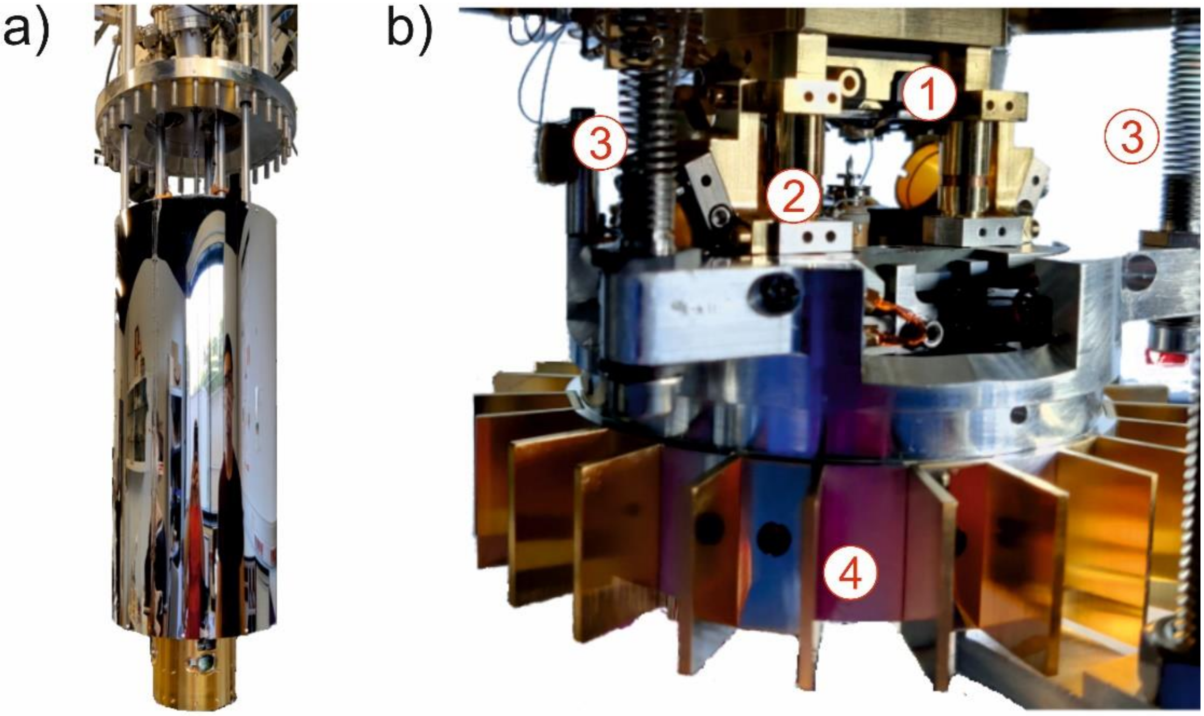

Figure 2-9 Components of the STM

a) Photograph of the STM out of the analysis chamber. The metallic cylinder is the outer cryostat and the golden piece in the lower part is the shield where the STM is hosted. b) Photograph of the main parts of the STM. 1) Sample Stage; 2) Piezo-electric with a STM tip; 3) Springs for vibrational isolation; 4) Eddy current dumper.

thermal shields that can be removed in situ to let the operator insert the sample into the sample stage. During measurements, these thermal shields must be closed to preserve sample and STM temperature.

- Parking
  The STM parking is placed inside of the analysis chamber. It consists of a carrousel structure where the samples and the STM tips can be stored in UHV conditions. The parking has capability to simultaneously host six samples.

- STM Head
  The STM head is the core part of the whole set-up, since the experiments are performed in the tunnelling junction. The STM head consist principally of two parts, the sample stage and the STM tip (Figure 2-9b).
  In the sample stage, the samples are placed inside, with the crystals pointing towards the STM tip. To put the samples into the stage, we employ a magnetic wobble stick. With the wobble stick, we can open the thermal shields, collect the sample from the parking and insert it into the stage.
  On the other hand, we can find the STM tip. The tip consists in a W or Au wire of 0.25 mm of diameter electrochemically etched. It is inserted in a tip holder, having into account that the maximum length of the tip can be around 1.5 mm, in order to be able to insert samples in the STM with the tip fully retracted. The tip holder

is magnetically attached to a ceramic piezoelectric tube, which is responsible for the imaging. When scanning, the feedback system collects the electrical current coming from the tip and actuates the piezo by applying a voltage, which makes the piezo contract or expand. By mapping these movements, the 3D images are formed. Additionally, the piezo can be moved in the X, Y directions, allowing to control the size of the image and the region to be scanned.
At the same time, the piezoelectric is mounted on a motorized table. This table can move macroscopically in the X, Y directions, and it is mounted on a rail that lets it move in the Z direction. Thus, the tip can also be moved macroscopically, approaching or retracting it to the surface.

- Dumping system
  The STM experiments are sensitive to vibrations of the environment. Because of the exponential dependence of the tunnelling current with the tip-sample distance, any movement that disturbs this distance can introduce noise in the measurement. To avoid most of the effects coming from vibrations, the set-up counts with a four-stage dumping system.

  The first dumping stage is the floor of the laboratory. The experimental set-up is mounted on top of a special floor that is decoupled from the rest of the building, preventing mechanical noises produced by the activity of other laboratories. The second stage consist in three pneumatic legs distributed strategically over the structure. When they are inflated, the whole set-up is floating, and most of the low frequency mechanical noises are removed. Importantly, special care must be taken during measurements, avoiding touching the machine to prevent the swinging of the STM and possible damages. The third stage are four springs that hang the STM. When the sample needs to be inserted or cooled down, these springs tight the STM head towards the cryostat, favouring the thermal contact and avoiding movement during the insertion. Nevertheless, to scan the sample, the springs are released and the whole STM head is suspended. In this way, several vibrational noises are avoided, especially those coming from the boiling of the cryogenic liquids inside the inner cryostat. The last stage of dumping is called eddy current dumper and it consists of a series of copper plates placed in the lower part of the STM head and permanent magnets mounted in the inner shield of the cryostat. When the STM head moves inside of the magnetized slots, the swinging of the head produces eddy currents in the copper plates (Figure 2-9b), inducing at the same time a magnetic field that is opposite to the one from the permanent magnets. These opposite fields dump the radial movement of the STM head inside the stage. Additionally, during the precise measurements, the primary pumping is turned off and decoupled from the system, while the turbo pumps are also turned off, avoiding the vibrational noise coming from them.

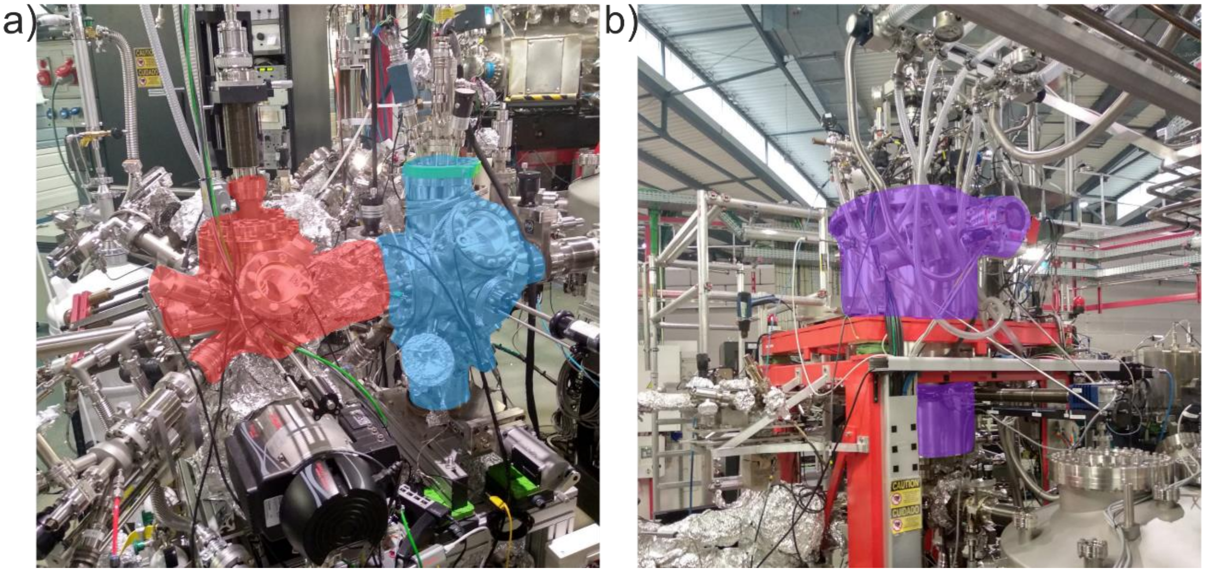

Figure 2-10 BOREAS Beamline experimental set-up.

a) Photograph of the preparation chamber (marked in red) and the analysis chamber (marked in blue) of the beamline. The preparation chamber is fully equipped to prepare in-situ the samples. b) Photograph of the HECTOR magnet (marked in purple). XAS, XMCD and XNLD measurements are performed in this chamber.

2.3.5 BOREAS Beamline

To explore the chemical magnetic properties of the samples with element specificity and surface sensitivity, we have taken advantage of the Boreas beamline at ALBA synchrotron [101,102]. We thank deeply the technical and scientific support from Dr. Manuel Valvidares and Dr. Pierluigi Gargiani.

The whole set-up operates in UHV conditions. The parts involved in the experiments presented in this thesis are described in the following:

- Preparation and STM chambers:
  The beamline is equipped with auxiliary preparation and STM chambers (Figure 2-10a). The samples can be introduced in the preparation chamber through a load-lock chamber. The preparation chamber is equipped with the same instrumentation described in Section 2.3.4.1 to perform the cleaning of the sample and graphene growth, making it possible to prepare in situ the samples.
  Next, samples are inspected in the STM chamber. This chamber hosts a commercial PanScan Flow STM, manufactured by RHK. The STM can operate at cryogenic temperatures, but in this case the cooling down is achieved by passing a flow of LN_2 or LHe, depending on the required temperatures.

- HECTOR magnet:
  After preparing the samples, they are carried from the preparation chamber to the end-station of the BOREAS beamline (preserving the UHV at all time). The end-station is equipped with a High Field Vector Magnet (HECTOR) (Figure 2-10b).

HECTOR is composed by superconductive magnets that allow to reach magnetic fields up to 6 T. In HECTOR, the magnetic and chemical properties of the samples have been measured by means of XAS, XMCD and XNLD. In this station, an X-ray energy beam is directed to the sample. The energy range of the beam can be varied between 80 eV and 4000 eV and the size of the spot can be changed between 100x100 μm^2 and 1000x1000 μm^2. During the experiments, the magnetic field was always applied parallel to the direction of the beam, to reach the magnetic saturation of the different samples. To measure magnetization curves, the magnetic field can be varied from +6 T to -6 T with a rate up to 2 T/min. Additionally, the magnet can operate at a wide range of temperatures, from 1.5 K to 350 K, allowing variable temperature measurements of the magnetic properties, which is important for the determination of the Curie temperature of the different materials. To properly perform XMCD and XLD measurements, the sample can be tilted in situ with respect to the beam. In particular, the two main positions are: i) perpendicularly oriented to the beam (normal incidence, NI, 0°), and ii) tilted 70° with respect to beam (grazing incidence, GI, 70º). Real grazing incidence (90°) is avoided, since if the sample is oriented completely parallel to the beam, the surface cannot be measured. A similar effect occurs when samples are measured with a grazing incidence angle of 80°, since in this case, the effective available surface is too small for the diameter of the beam, reducing the signal. Importantly, additional rotation angles between 0° and 70° can be selected to make angle dependent measurements.

3. Increasing magnetic anisotropy of Dy by metal-organic coordination

Lanthanide metals are nowadays common in technology, being used in different fields, as alloys, permanent magnets, optical fibers, luminescent devices, high-temperature superconductors, and catalysts [50,103,104]. Nevertheless, recent works have remarked the potential of these elements to be used as single atom magnets. Particularly, the observation of magnetic remanence in holmium (Ho) single atoms deposited on a decoupling layer of MgO(100) on Ag(100)[105] with relaxation times up to 1500 s at 10 K indicates that lanthanides can be used as single atom magnets on surfaces. A later study proved the feasibility to write and read electronic states from these atoms, being a pioneer work showing the future use that these elements can have as the smallest magnetic information units [106,107].

The main problem of employing individual atoms, not involved in any assembly, resides in the thermal stability of the materials under study, since the experiments were realized at temperatures ranging from 1 K to 10 K. However, at higher temperatures, the individual atoms gain enough energy to diffuse over the surface forming clusters, which avoid their use in practical applications. To solve this inconvenient, it is proposed in this chapter a strategy based on the coordination of lanthanides with organic ligands to form metal-organic networks, envisioning potential for using the nodes as bits.

We speculate that our approach could be employed to get the full potential of lanthanides as single atom magnets, because of their electronic structure, as described in detail in the introduction. First, lanthanides exhibit a strong spin orbit coupling, being characterized by the total angular momentum J [108,109]. In this context, the crystal field acts as a perturbation of the spin orbit coupling, breaking the degeneracy of the electronic states and defining the final set of $|J, J_z>$ states. Second, the valence electrons of lanthanides reside in the 4f shell, which is very internal, and, consequently, they interact much less with the environment, thus preserving the orbital magnetic moment. As a result, lanthanides exhibit in general a high magnetic anisotropy. Through on-surface coordination chemistry, it should be possible to tune the crystal field by an appropriate choice of organic linkers to increase the magnetic anisotropy of the lanthanides [1,110]. Nevertheless, such strategy has never been experimentally ratified for on-surface lanthanide-based metal-organic networks.

In the first section of this chapter, the structural, electronic and magnetic properties of a Dy-TDA metal-organic network on Cu(111) are revealed by means of STM, STS, XAS, XNLD and XMCD, complemented by DFT and multiplet calculations. These techniques show that the coordination bond established between the carboxylate groups and Dy

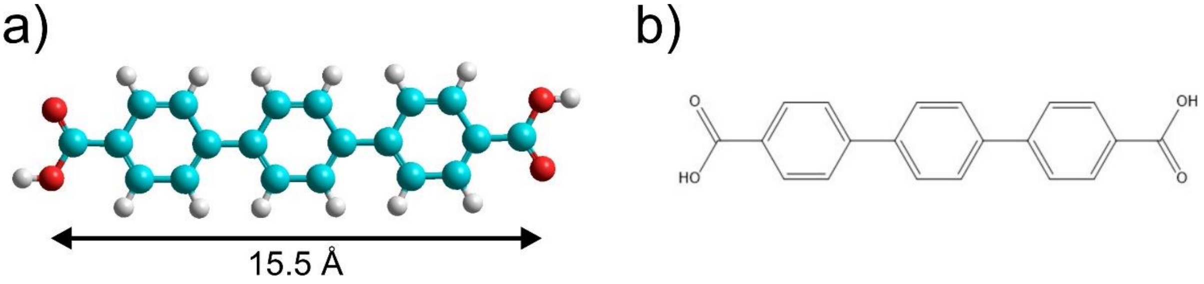

Figure 3-1 Chemical structure of a free standing TDA species.

a) Stick and ball model obtained by relaxing the species in the gas phase (MM+, Hyperchem package). Carbon, oxygen and hydrogen atoms are represented by cyan, red and white solid spheres, respectively. b) Chemical structure of TDA.

atoms is fundamentally ionic, with a minor covalent contribution. In addition, the coordination environment dictated by the organic linker induces an almost in-plane easy axis of the magnetization of the Dy centres, in contrast with the out of plane behaviour of individual atoms on Cu(111)[93]. In addition, the coordination scheme produces a huge increment in the magnetic anisotropy of Dy while embedded in the metal-organic architectures.

In the second section of the chapter, a shorter ligand equipped with the same terminal carboxylate moieties (TPA) is used to infer the implications of reducing the internodal distance. A Dy-TPA metallosupramolecular architecture is formed on Cu(111), being also reticular as the previous Dy-TDA network, but featuring reduced internodal distance. The structural characteristics are determined by means of STM and complemented with DFT calculations. On the other hand, the magnetic properties are characterized by means of XAS, XNLD and XMCD. Our results show that the small variation of the crystal field induces a higher tilt of the easy axis of magnetization of Dy centres towards the surface and an increase in the magnetic anisotropy as compared to Dy-TDA.

The main results of this chapter have been recently published by us in Small[111].

3.1 TDA deposition on Cu(111)

The p-terphenyl-4,4′-dicarboxylic acid (TDA) species is a linear organic ligand equipped with carboxylic groups to steer metal-organic coordination (Figure 3-1). Such molecular linkers and derivatives have been widely used as building blocks to engineer on-surface metal-organic networks embedding alkali and 3-metals[44,112–117], and recently it has been demonstrated their capability to coordinate with lanthanide metals to form metallosupramolecular architectures[27,29], making them appealing for our scientific purposes.

First, deposition of TDA species on a clean surface of Cu(111) gives rise to the formation of ordered islands, which are stabilized by hydrogen bonds between adjacent molecular species, in agreement with previous published results[29]. The network can be described

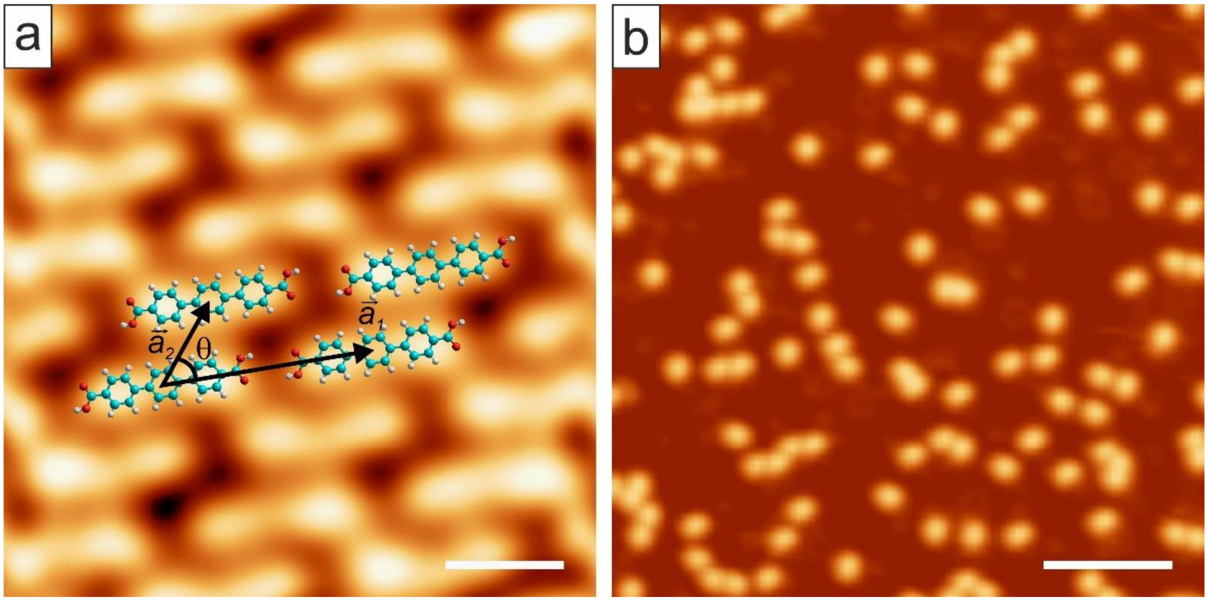

Figure 3-2 Assembly and deprotonation of TDA species on Cu(111).

a) Self-assembly of TDA after deposition on Cu(111) at RT. The self-assembly pattern features an oblique unit cell, described by the vectors $\vec{a}_1 = (18.7 \pm 0.5)$ Å and $\vec{a}_2 = (8.2 \pm 0.5)$ Å, forming an angle between them of $\theta = (55 \pm 5)°$ (V_{bias} = 0.5 V, I_t = 20 pA, Scale bar: 1 nm). b) TDA deprotonated species after deposition with the substrate held at 373 K (V_{bias} = 1.0 V, I_t = 100 pA, Scale bar: 8 nm).

by an oblique unit cell, with unit cell vectors $\vec{a}_1 = (18.7 \pm 0.5)$ Å and $\vec{a}_2 = (8.2 \pm 0.5)$ Å, spanning an angle of $\theta = (55 \pm 5)°$ (Figure 3-2a).

Next, deposition of TDA species on Cu(111) held at 373 K leads to a full deprotonation of the carboxylic moieties, now transformed into carboxylates[29]. The molecules are imaged as bright protrusions, which are randomly distributed on the surface, not forming any assembly (Figure 3-2b).

3.1.1 Structure of Dy-TDA coordination network

When Dy atoms are deposited on a submonolayer coverage of TDA on Cu(111) held at 373 K, to favour the diffusion of the molecules, a reticular coordination network is obtained as previously reported (Figure 3-3a)[29]. A closer inspection to the network reveals that the molecules are imaged as bright rods, whereas the mononuclear metallic centres are seen as depressions[27]. The network is described by an almost square lattice, with internodal distance $\vec{b} = (20.5 \pm 0.5)$ Å and an angle of $\theta = (88 \pm 5)°$ between the unit cell vectors (Figure 3-3b). Herein, the structure is stabilized by an 8-fold coordination bond between the Dy and the oxygens of the carboxylate moieties.

To gain further insights about the structure, DFT calculations were performed. Figure 3-4a displays the optimized DFT calculated models for the Dy-TDA network, both in lateral and top view. Dy is placed on hollow positions of the Cu atomic lattice. Notably, to

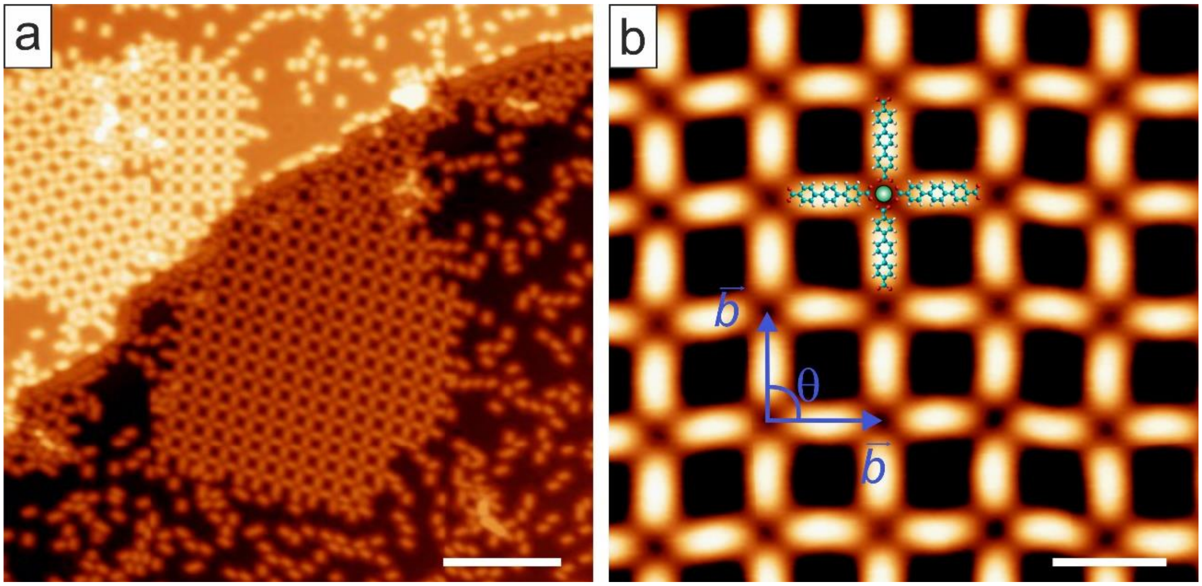

Figure 3-3 Dy-TDA coordination networks on Cu(111).

a) STM image of Dy-TDA showing coordination patches with 4 different orientations (V_{bias} = 0.5 V, I_t = 10 pA, Scale bar: 12 nm). b) High quality STM image showing the details of the network with an atomistic model superimposed. The green ball represents the Dy atom. The unit cell of the network is square, composed by the vectors $\vec{b} = (20.5 \pm 0.5)$ Å forming an angle of $\theta = (88 \pm 5)°$ (V_{bias} = 0.5 V, I_t = 20 pA, Scale bar: 2 nm).

coordinate with the lanthanide centres, the carboxylate moieties are rotated with respect to the plane of the network [29].

The coordination structure calculated by DFT is similar to a square antiprism (D_{4d} symmetry), though it presents distortions deviating from this ideal symmetry (Figure 3-4b). To investigate such deviations, the network has been analysed by continuous shape measurements (CShMs) [118]. The method compares the atomic positions obtained by DFT calculations with a symmetry of reference. The difference is numerically computed and gives an estimation of how similar the structure is compared to the reference. All the symmetries included in the software were tried, being D_{4d} the most similar one. Nevertheless, the deviation from the D_{4d} symmetry is still high. In fact, DFT reveals that the twist angles between the diagonals of the antiprism are 31° and 34°, far from the ideal distorted antiprism, in which such twist angles are 45°. As a result, the structure is compressed in the vertical direction, affording a C_4 symmetry, which is not included in the software for an eight-fold polyedra.

The bonding energy per TDA species is ≈9.84 eV, with two main contributions. The first component is due to the interaction of the molecule with the metallic substrate, which is ≈1.25 eV per TDA. The second one comes for each Dy-bond (2.15 eV). Such values are in good agreement with a predominant ionic bond.

Structurally, non-coordinated deprotonated TPA species on Cu(111) present a bending of the molecular backbone, while the peripheral carboxylate-aryl moieties are rotated

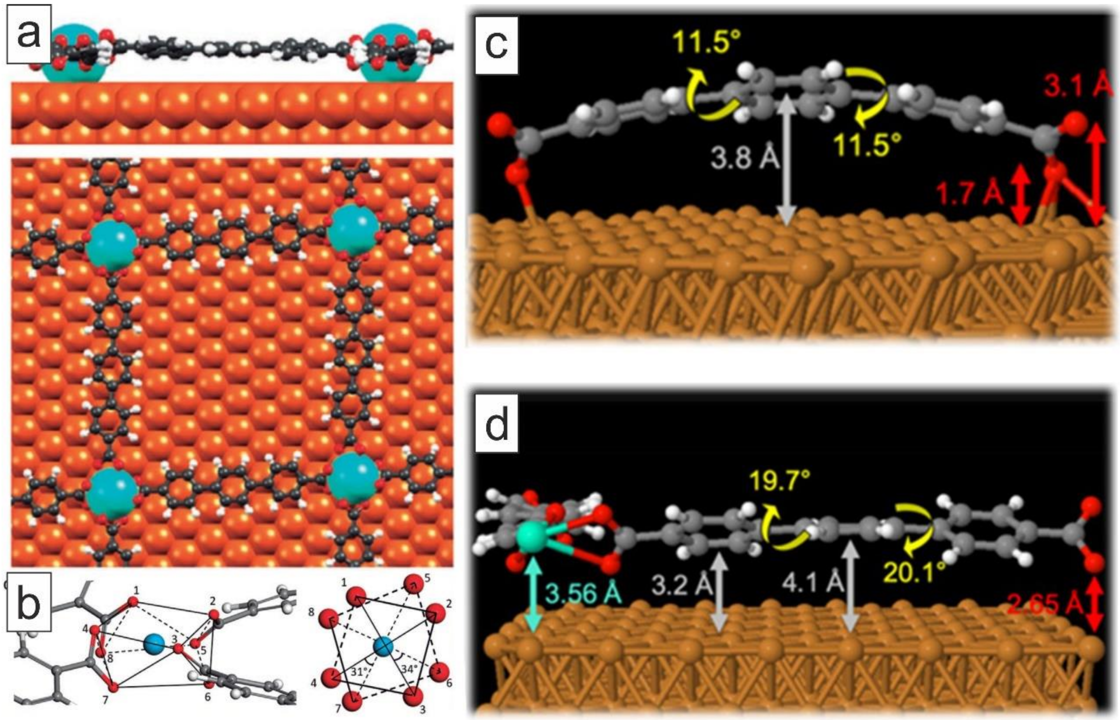

Figure 3-4 DFT calculations on Dy-TDA coordination network structure.

a) Side (upper panel) and top (lower panel) view of a Dy-TDA coordination node. The TDA terminal oxygens are rotated alternately in the same molecule. b) 3D and top view of the coordination polyhedron formed by oxygen atoms. c, d) Lateral view of the adsorption geometry of TDA(c) and TDA coordinated with Dy(d) on Cu(111). Most representative distances in this interface are indicated. White, grey, red, tan and green spheres correspond to H, C, O, Cu and Dy atoms respectively.

with respect to the plane of symmetry, in order to steer the interaction of one oxygen atom of the carboxylate unit with the substrate, as illustrated in Figure 3-4c. Next, upon coordination, the deprotonated TPA species recover much of its planarity, though the peripheral carboxylate-aryl moieties rotate to steer the coordination (Figure 3-4d).

3.1.2 Electronic properties of Dy-TDA coordination network.

To determine the electronic structure of the network, scanning tunnelling spectroscopy (STS) was performed at selected points: clean substrate, non-coordinated molecule, Dy-coordinated molecule, and metallic centre (Figure 3-5a). The non-coordinated species present a resonance at 1.2 V, which is tentatively assigned to the LUMO. Upon coordination, such resonance is shifted to 1.7 V. DFT calculations of the density of states for both species reveal that the LUMO resonance of the non-coordinated species is in fact shifted toward higher energies, corroborating our rationalization (Figure 3-5d). Such a shift in energy is associated with the change in the conformation of deprotonated TDA upon coordination. The distribution of the LUMO was probed by acquiring a dI/dV map at 1.6 V, which reveals a two-lobed aspect at the rims of the molecular backbone.

Next, we wonder about the ionic versus covalence nature of the Dy-carboxylate bond. It is important to keep in mind that a lanthanide-directed metal-organic bond is

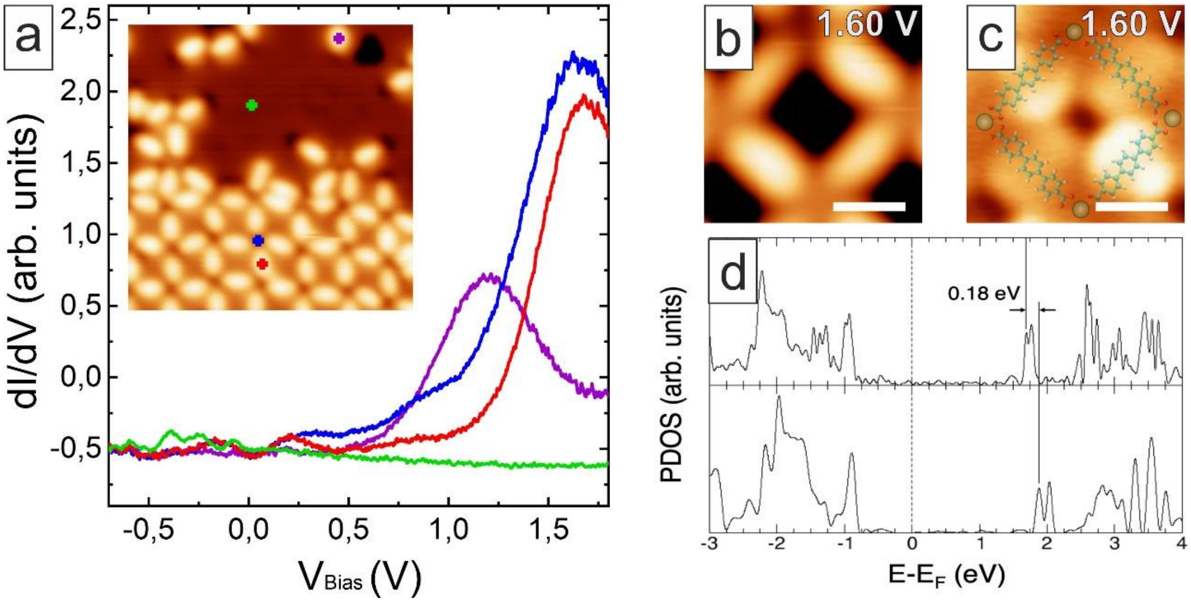

Figure 3-5 Electronic structure of Dy-TDA coordination network.

a) STS spectra taken on non-coordinated TDA molecules (purple), coordinated TDA (red), Dy centres (blue) and Cu(111) (green). The inset is a STM image showing the STS positions. b,c) STM reference image and dI/dV map taken at 1.60 V, with corresponding superimposed atomistic model (V_{bias} = 1.6 V, I_t = 80 pA, Scale bar: 1 nm). d) Computed density of states of non-coordinated TDA species (top panel) and Dy coordinated TDA (bottom panel).

predominantly ionic, due to the inner character of the f-valence electrons [104,119]. First, a charge density plots was calculated and displayed in Figure 3-6. The plot illustrates the difference in the charge distribution density between the interacting part of the system and the non-interacting part. In these plots, red colour shows regions with accumulation of charge, whereas green colour displays regions with a depletion of charge. As it can be observed, the charge is mostly accumulated at the oxygens of the carboxylate groups, the Dy metal loses charge and there is no discernible distribution of charge associated with covalency, which altogether is a strong indication of an ionic bond. This result is in good agreement with XPS data of this same network published recently by us[29] also in agreement with Gd-TDA networks on Cu(111)[27]. The minority contribution of covalence bond can be experimentally seen by the presence of the 1.7 V resonance at the metallic centres, though with less intensity in dI/dV mapping[120,121].

3.1.3 Magnetic properties of Dy-TDA coordination network

In this section, the effect of the coordination environment on the electronic and magnetic properties of Dy will be discussed. To that end, XAS, XNLD and XMCD experiments were performed over two distinct samples, Dy clusters on Cu(111) and Dy-TDA coordinated network on Cu(111). To properly compare the samples, the Dy coverage is the same in both cases, equivalent to ≈0.01 ML. Additionally, our findings are compared with results from individual Dy atoms on Cu(111) [93].

In Figure 3-7, XAS, XNLD and XMCD measurements for Dy clusters and Dy-TDA networks are displayed, whereby the background contribution coming from the Cu substrate has

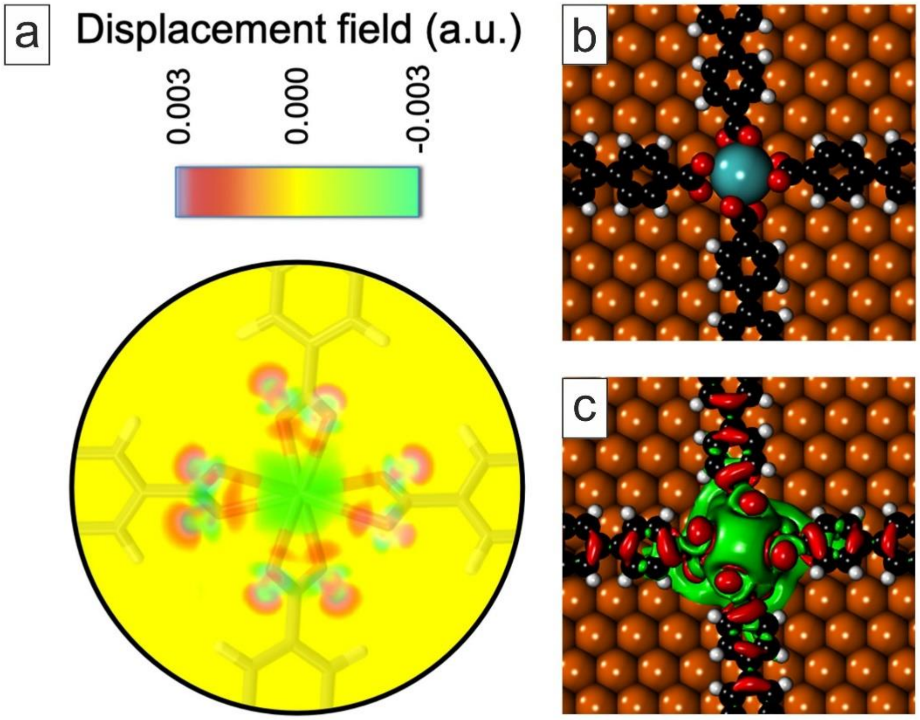

Figure 3-6 Charge density difference plots of the Dy-TDA network on Cu(111).

a)3D plot illustrating the difference between the electron charge density of the interacting system and the one of its non-interacting counterpart. The structure model of Dy-TPA on the Cu(111) surface is superimposed. Negative values (green) represent charge depletion, accounting for an ionic character of the Dy centre. Positive values (blue, red) indicate charge accumulation, highlighting the charge gained by the carboxylate moieties. b) Structural model and c) 3D charge density difference isosurface (with isovalues of 0.001 a.u.). Green isosurfaces represent charge depletion and red isosurfaces indicate charge accumulation.

been previously removed. The experiments were performed with a nominal temperature of 2 K, though the experimental temperature was found to be 6 K (see below).

By analysing the XAS structure of the M_5 peak for Dy clusters and for Dy-TDA networks, it is observed that both samples exhibit the same structure of three peaks, featuring the one at 1289 eV more intense than the other two. Such behaviour of the third peak is the signature of the trivalent oxidation state of Dy (Dy^{3+})[93,122]. On the contrary, the results for individual Dy atoms on Cu(111) are different. In that case, the XAS structure in the M_5 region illustrates that the second peak is more intense than the rest, indicating a divalent oxidation state (Dy^{2+})[93]. The change of oxidation state from individual Dy atoms to clusters of Dy atoms is attributed to the metallic bonds formed between the Dy atoms inside the cluster, a phenomenon also found in bulk compounds. In the case of the Dy-TDA networks, the coordination of Dy with the carboxylate ligands results in a 3+ oxidation state (Dy^{3+}).

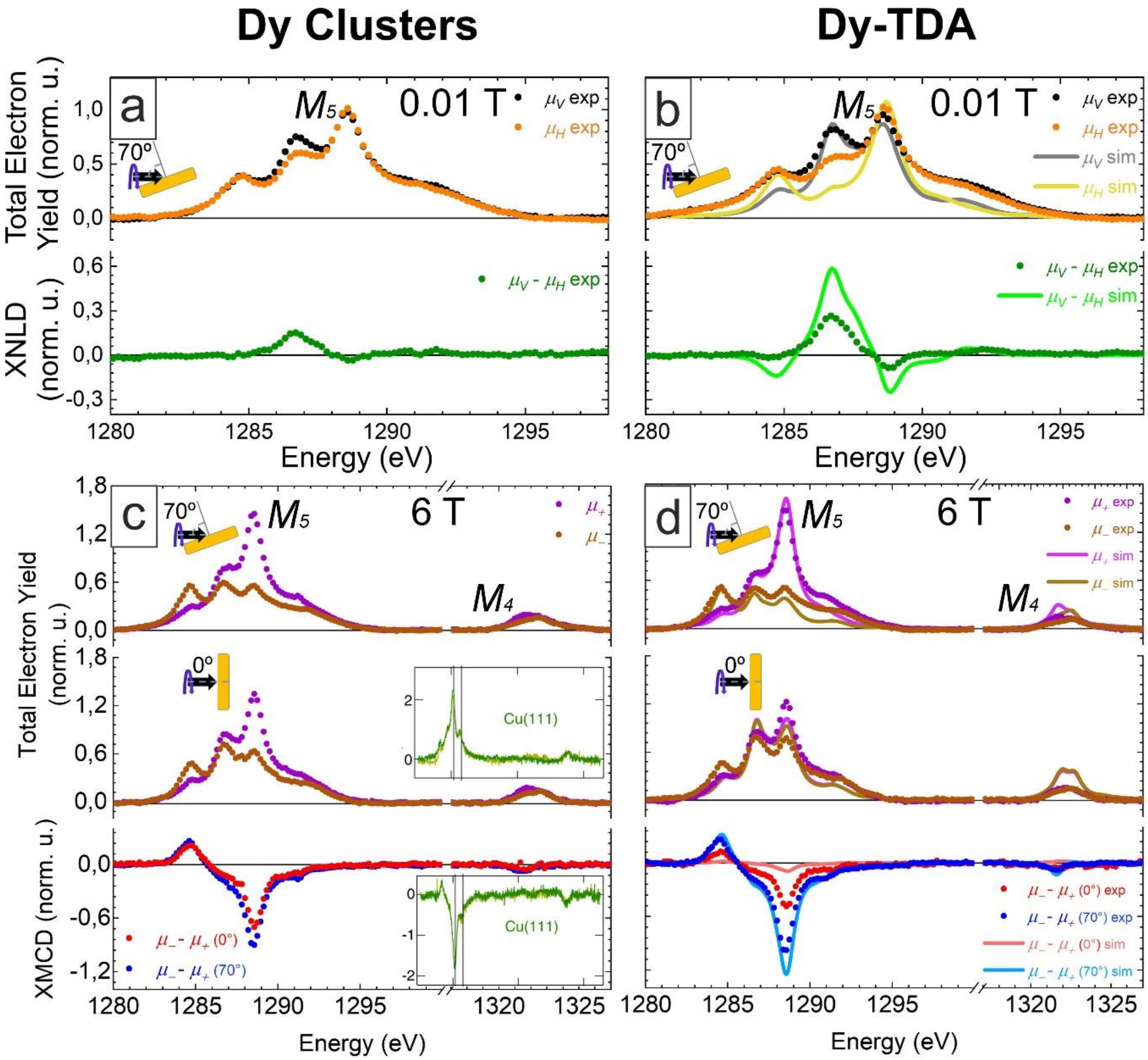

Figure 3-7 XAS, XNLD and XMCD of Dy clusters and Dy-TDA on Cu(111).

a,b) XAS spectra acquired with vertical and horizontal linearly polarized light in the M_5 peak of Dy taken at 70° (GI, top) and XNLD (bottom) of Dy clusters on Cu(111)(a) and Dy-TDA(b). c,d) XAS spectra acquired with circularly polarized light, to the left and to the right in the $M_{4,5}$ peaks of the Dy taken at 70° (GI, top) and at 0° (NI, middle) of Dy clusters on Cu(111)(c) and Dy-TDA(d). Bottom panels display the XMCD signal for both orientations. The solid lines in the panels of Dy-TDA corresponds to multiplet calculations of the system, to compare with the experimental data. The inset in the middle panel in c) is the average XAS signal taken with circularly light polarized to the left and to the right for NI (darker) and for GI (lighter) for individual atoms of Dy on Cu(111). The inset in the bottom panel is the XMCD signal in NI and in GI (same colour legend). Both insets have been adapted from reference [93].

The study of the XNLD curves for Dy clusters and Dy-TDA samples gives information about the charge distribution of the valence orbitals of the Dy atoms in both situations. These measurements were performed with low magnetic field (0.01 T). The linear dichroism signal measured in Dy clusters is a fingerprint of the charge anisotropy of the 4f orbitals. Comparing to Dy clusters, the XNLD signal of Dy-TDA is slightly higher, which means that the charge anisotropy increases with the coordination. These results were compared with XNLD spectra taken in $DyPc_2$[123], which is a molecule that can be rationalized as metal-organic sandwich of Dy^{3+} [124] with a coordination symmetry D_{4d}.

Interestingly, for this molecular species the structure of the peaks is inverted respect to the signal obtained in Dy in clusters or metal-organic networks. Even if in our case the symmetry is C_4 instead of D_{4d}, the symmetry axis has the same orientation for both Dy-TDA and $DyPc_2$, and, thus, a similar XNLD would be expected. The inverted orientation indicates that for Dy-TDA networks the effective crystal field acting on Dy atoms does not follow the coordination symmetry axis. A further comparison with Dy_3^+ ions in the dysprosium-tris(1,1,1-trifluoro-4-(2-thienyl)-2,4-butanedionate) ($Dy(tta)_3$) complex on Au(111)[110] also confirms that the alignment of the symmetry axis of Dy 4f orbitals in the Dy-TDA network is close to the surface plane.

Regarding the magnetic properties, it has been reported that individual Dy atoms on Cu(111) are almost isotropic, presenting similar XMCD intensities measured at 0° and at 60° [124]. Compared to individual atoms, Dy clusters display an increase in the magnetic anisotropy, showing a more intense XMCD signal measured at 70° than at 0°. These results proves that it is possible to tune the magnetic anisotropy of the Dy by the formation of metallic bonds with other Dy atoms, as it has been previously reported for other lanthanides [25]. Furthermore, focusing our attention to Dy-TDA, it is observed an increment of the difference between the grazing and normal incidence intensities. To quantify the magnetic anisotropy, sum rules were applied[98,125]. The sum rules are used to calculate the projection of the magnetic moments along the measurement axis (at 0° and at 70°) at the experimental conditions. The results showed in Table 3-1 corresponds to the experimental conditions of 6 T of magnetic field and the sample held at 6 K. Additionally, data for Dy^{2+} from reference [93] taken at 6.8 T and 2.5 K are displayed for comparison.

The moment anisotropy $\Delta M_T = M_T(70°) - M_T(0°)$ gives information about the presence of an easy axis of the magnetization. The lower this quantity, the more magnetically isotropic is the sample since both axes are equally magnetized. Comparing the results in Table 3-1, Dy coordinated with TDA exhibits a moment anisotropy 4.9 times higher than the individual Dy atoms and 2.2 times bigger than Dy clusters, indicating a strong improvement of the magnetic anisotropy due to the CF imposed by the TDA molecules.

To further support these results, multiplet calculations have been performed for Dy centres of Dy-TDA networks (Figure 3-7b, d). Even if there is not a perfect match in some results, due to the difficulties to simulate the exact crystal field, the peak structure of the XAS, the correct orientation of the peaks of the XNLD and the magnetic anisotropy of the XMCD are qualitatively well reproduced. Additionally, through the simulations, the role of the Cu(111) substrate has been explored, revealing an almost negligible role, which is just limited in contributing to the conformation of the molecular species upon adsorption and coordination with Dy.

Measurements of magnetization curves were performed to investigate the magnetic behaviour of these samples in an external magnetic field. Such curves reveal how the main peak of the M_5 edge is modified upon changing the magnetic field. The measurement

	Dy clusters on Cu(111)		Dy centres on TDA network		Dy single atoms on Cu(111)	
Incidence angle (°)	0	70	0	70	0	60
$\langle L_z\rangle(\hbar)$	1.19(12)	1.87(19)	1.36(14)	2.35(24)	4.7(2)	4.4(2)
$\langle S_z\rangle(\hbar)$	0.65(6)	0.86(9)	0.44(4)	1.14(11)	1.6(1)	1.5(0)
$\langle J_z\rangle(\hbar)$	1.84(18)	2.73(27)	1.80(18)	3.49(35)	6.3(2)	5.9(2)
$M_T(\mu_B)$	2.49(25)	3.59(36)	2.24(22)	4.63(46)	7.9(2)	7.4(2)
$\Delta M_T(\mu_B)$	1.10(61)		2.39(68)		0.5(3)	

Table 3-1 Expectation values obtained from sum rules for Dy clusters, Dy centres on TDA network and Dy single atoms on Cu(111).

Expectation values at the experimental temperature and at 6T field of orbital ($\langle L_z\rangle$), spin ($\langle S_z\rangle$), and total moments ($\langle J_z\rangle$), total magnetic moment (M_T) and moment anisotropy (ΔM_T) obtained from XMCD sum rules at normal and grazing incidences for Dy clusters on Cu(111), Dy-TDA and Dy single atoms on Cu(111) (obtained from reference [93]).

is realized by increasing and decreasing the magnetic field to observe if the samples present hysteresis loop or magnetic remanence. Magnetic remanence would imply that the Dy could act as a single atom magnet. Neither Dy clusters nor Dy-TDA networks on Cu(111) present opening of an hysteresis loop or magnetic remanence (Figure 3-8 a,b). Since the Dy^{3+} is a Kramer ion (guaranteed doubly degenerated ground state in absence of magnetic field) and has a total moment of $J_z = 15/2$, it should be an ideal candidate to act as a single atom magnet[105,106], provided the coordination preserves a high J_z. The causes that prevent Dy to show magnetic remanence in these systems could be: i) the interaction of the Dy with conduction electrons coming from the substrate, ii) the interaction with phonon modes associated to the molecules or the substrate [17,93,126,127], and iii) the life-time of the magnetic remanence is too short and thus, it is not possible to observe it in the time-scale of the experiments [122].

Magnetization curves were fitted to a theoretical model based on a simple spin Hamiltonian with uniaxial zero-field splitting [110]:

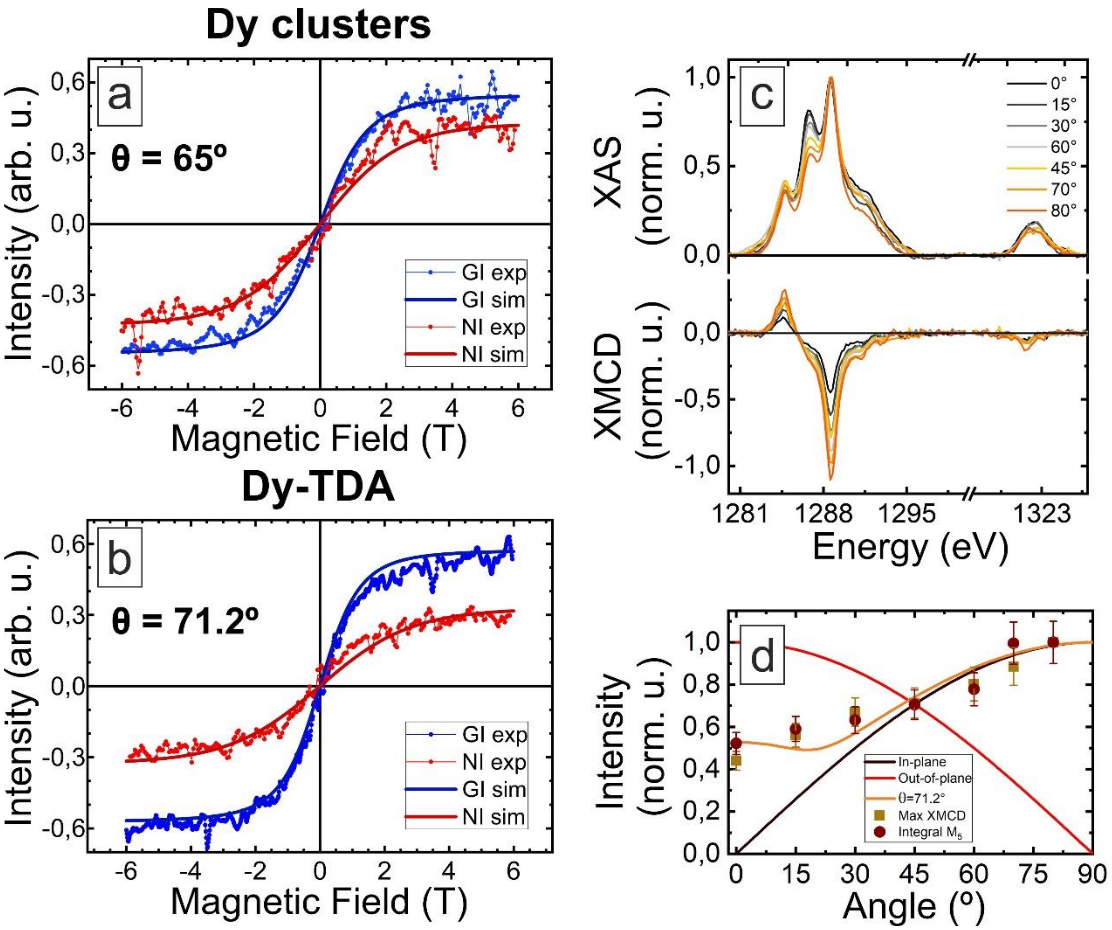

Figure 3-8 Magnetization curves of Dy clusters and Dy-TDA network on Cu(111) and angle dependence of Dy-TDA integrated XMCD.

a, b) Magnetization curves of Dy clusters (a) and Dy-TDA (b) on Cu(111) at T = 6 K. The model employed to fit the curves is described in the text. c) XAS and XMCD spectra taken at angles ranged from 0° to 80° in the $M_{5,4}$ edges of Dy centres in Dy-TDA sample at B = 6 T and T = 6 K. d) Angle dependence data for Dy-TDA network. The solid lines represent theoretical models with the easy axis oriented at different angles with respect to the surface and represent the projection of the expected value of the magnetization along the direction of the beam. Yellow square dots correspond to the experimental values of the peak maximum at the M_5 edge of the Dy centres of Dy-TDA. Round brown dots represent the value of the integral of the whole M_5 edge. Both, theoretical and experimental data are normalized to the unit, being the highest intensity 1.

$$H = \mu_B g_J \vec{B} \cdot \vec{J} + D J_z^2 \tag{3.1}$$

where $J_z = 15/2$ and Landau factor $g_J = 4/3$ for the nine 4f electrons of Dy^{3+}. To properly fit the model with the experimental data, the temperature T, the anisotropy energy D and the angle of the quantization axis were taken as free parameters. The first remarkable result is that the temperature to fit the curves (6 K) is higher than the nominal temperature of the experiments (2 K). However, this difference could be explained by an insufficient thermal contact of the sample with the cold reservoir of the end-station, which would increase the effective temperature of the sample. During the chapter, 6 K has been considered as the real substrate temperature. The second meaningful found result is that during the calculations, for both samples, the anisotropy energy goes to high negative values, indicating the presence of a strong easy axis anisotropy, which at these temperatures and for the fields employed in the experiment means that the system can be modelled by an effective 1/2 spin system with only the doubly degenerated ground state being occupied.

As illustrated in Figure 3-8d, the Dy-TDA network cannot by modelled by an easy plane of magnetization lying in-plane or out of plane from the substrate. Our calculations establish an easy axis of the magnetization tilted a certain angle from the normal of the surface, being 65° for Dy clusters and 71.2° for Dy centres on Dy-TDA networks. This result explains the higher intensity of the grazing incidence XMCD signals compared to normal incidence, as there is a higher projection of the easy axis of the magnetization on the beam direction when arrives from grazing incidence. In the case of Dy clusters, the 65° of inclination between the quantization axis and the normal of the surface that fits the magnetization curves can be attributed to the averaging of the different Dy atoms in the cluster with different anisotropy orientations.

XMCD angle dependent measurements were taken for Dy-TDA sample. The XMCD signal was measured in a range from 0° to 80° (Figure 3-8c). These measurements have been compared with the theoretical projection of the magnetization for the quantization axis oriented at 0° (totally out of plane), at 90° (totally in plane) and tilted 71.2° from the normal of the surface (Figure 3-8d), the latter exhibiting an excellent agreement. The origin of the inclination of the axis of quantization is revealed by multiplet calculations[128]. The simulations show that the orientation of the anisotropy fundamentally depends on the balance of two factors: i) The symmetry of the crystal field, which in this case favours the out of plane direction and ii) the interaction of the negative charges of the O atoms involved in the coordination with the Dy^{3+}, which modifies the charge distribution of the 4f orbitals, steering the in-plane direction.

At this point, it is important to explain that the values for the moments expressed in Table 3-1 are lower limits of the real values, since the samples are not magnetically saturated. This saturation cannot be experimentally achieved for our set-up. To saturate the sample, it would be necessary to measure the XMCD signal along the easy axis of magnetization of the sample. However, the Dy-TDA coordination samples present six metallosupramolecular domains on Cu(111), due to the adsorption on six-fold symmetric substrate. As a result, a XMCD measurement is an average of the contribution of the distinct domains.

3.2 Effects of reducing the internodal distance preserving the lattice structure: Dy-TPA networks

The previous section illustrates that metal-organic coordination is able to improve the magnetic anisotropy of dysprosium. However, there was no opening of the hysteresis loop and no magnetic remanence. As it has been discussed above, part of such

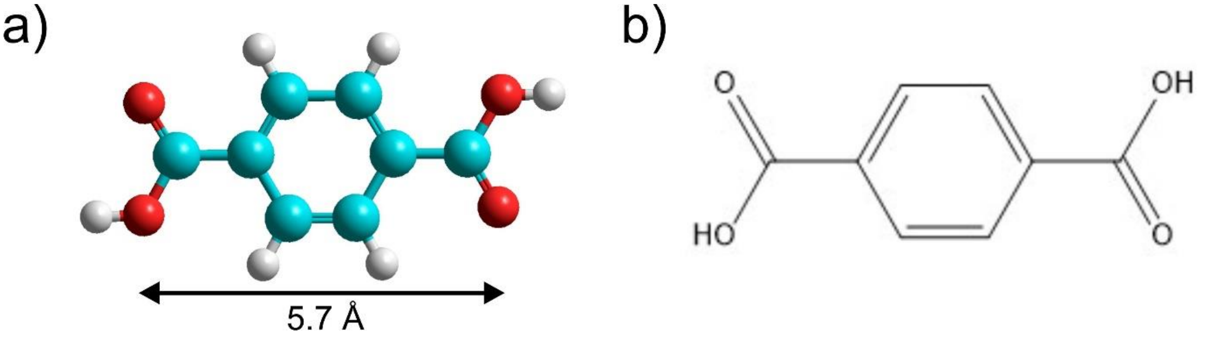

Figure 3-9 Chemical structure of a free standing TPA species.

a) Stick and ball model obtained by relaxing the species in the gas phase (MM+, Hyperchem package). Carbon, oxygen, and hydrogen atoms are represented by cyan, red and white solid spheres, respectively. b) Chemical structure of TPA.

shortcoming could be associated to the interaction of the phonon modes coming from the molecules of the network. Additionally, there is no information about the existence of coupling or not between the Dy nodes, which could be pernicious for the development of a lattice of single atom magnets.

In an attempt to overcome these barriers, benzene-1,4-dicarboxylic acid (TPA) organic ligand is employed, which is shorter and also more rigid. This ligand consists in two carboxylate groups attached in the para positions of a phenyl ring, making the molecule shorter (5.7 Å) than TDA (Figure 3-9), while preserving the carboxylic moieties to steer coordination.

The deposition of Dy on top of a submonolayer TPA coverage on Cu(111) held at RT results in the formation a Dy-directed metal-organic network (Figure 3-10), as previously reported [29]. This network can be described by a slightly distorted a square structure, with unit cell vectors $\vec{c} = (11.8 \pm 0.5)$ Å and an angle of $\theta = (93 \pm 5)°$.

DFT optimized models of these architectures reveal that they share some characteristic with its Dy-TDA homologous, since Dy is also placed on hollow sites of the lattice, while the carboxylate moieties also display a dihedral rotation (Figure 3-11a). The crystal field induced by this coordination is again a distorted square antiprism, in which the twist angle between the oxygen planes is higher than for the TDA. As a result, the coordination environment is less compressed in the vertical direction (Figure 3-11b). Regarding the adsorption geometry, DFT calculations show differences between the uncoordinated species and the coordinated ones. In the dilute phase, TPA species are placed at 3.4 Å from the surface as illustrated in Figure 3-11c. The carboxylate moieties are both rotated, looking to maximize the interaction of one of the oxygen atoms with the Cu surface. Upon coordination with Dy, the ring is oriented completely parallel to the surface, increasing the adsorption distance to 4.0 Å (Figure 3-11d). The carboxylate groups are rotated to coordinate with the Dy atom. Again, the coordinative bond established between the terminal oxygens and the Dy atoms exhibits a strong ionic character, as it is revealed by the calculated charge density difference plots (Figure 3-11e-g).

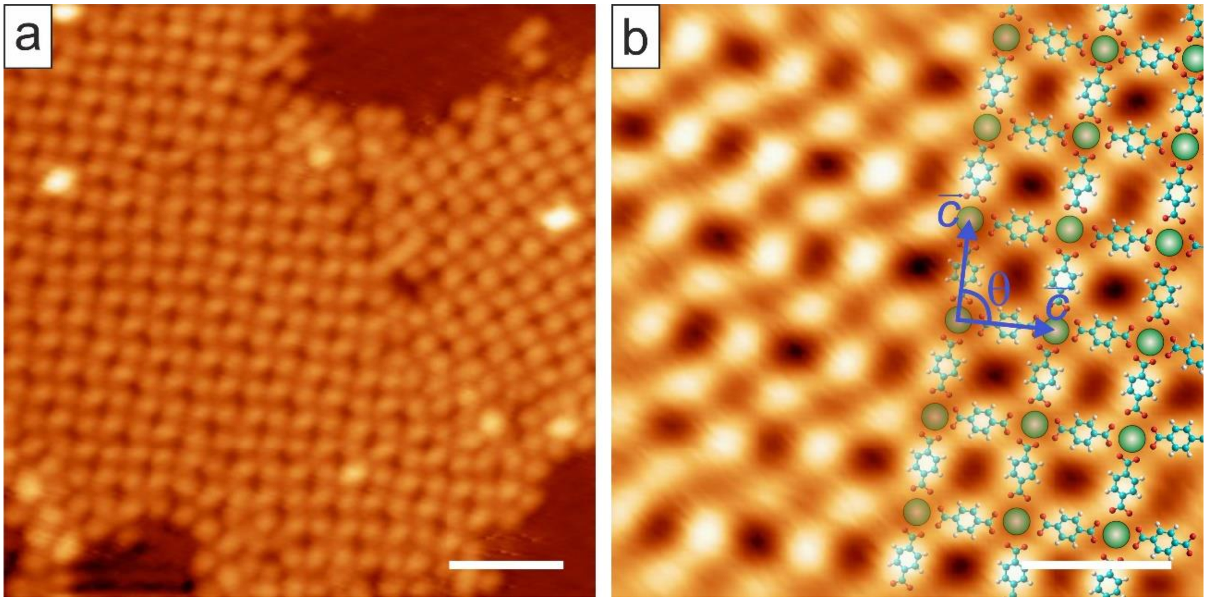

Figure 3-10 Dy-TPA coordination networks on Cu(111)

a) STM image showing Dy-TPA coordination patches on Cu(111) (V_{bias} = 1.1 V, I_t = 110 pA, Scale bar: 4 nm). b) STM image displaying the network with a superimposed atomistic model. The green ball represents the Dy atom. The unit cell is square, described by the vectors $\vec{c} = (11.8 \pm 0.5)$ Å forming an angle of $\theta = (93 \pm 5)°$ (V_{bias} = -1.1 V, I_t = 170 pA, Scale bar: 2 nm).

XAS, XNLD and XMCD measurements were performed on the TPA-Dy sample to collect the magnetic information of this system and compare the results to the previously obtained for Dy-TDA networks. The peak structure of the XAS spectra acquired by using linearly polarized light in both vertical and horizontal directions at low magnetic field (0.01 T) and at 6 K features the same three peaks structure obtained for Dy clusters on Cu(111) and for Dy-TDA networks, indicating the oxidation state of the Dy atoms coordinated with TPA molecule is Dy^{3+} (Figure 3-12a). Subtracting both signals, the XNLD spectrum is obtained, which is analogous to the one found in TDA-Dy, thus revealing that the axis of the Dy charge is close to the surface plane.

XMCD signal is measured in grazing (70°) and in normal (0°) incidences to analyse the magnetic anisotropy and the orientation of the easy axis of magnetization (Figure 3-12b). The results show a strong magnetic anisotropy, with a more intense signal coming from the grazing incidence. To quantitatively compare these findings with Dy clusters on Cu and Dy-TDA, sum rules are applied to calculate the projection of the magnetic moments. The values are showed in Table 3-2.

The TPA-Dy network increases the moment anisotropy of Dy 1.2 times more than the Dy-TDA architecture. This increment in the moment anisotropy is attributed to the differences in the coordination antiprism imposed by TPA molecules. Multiplet calculations were performed to corroborate the experimental data. Though a perfect match between theory and experiment is almost impossible due to the difficulties in establishing the exact crystal field, the XAS peak structure, the orientation of XNLD curve

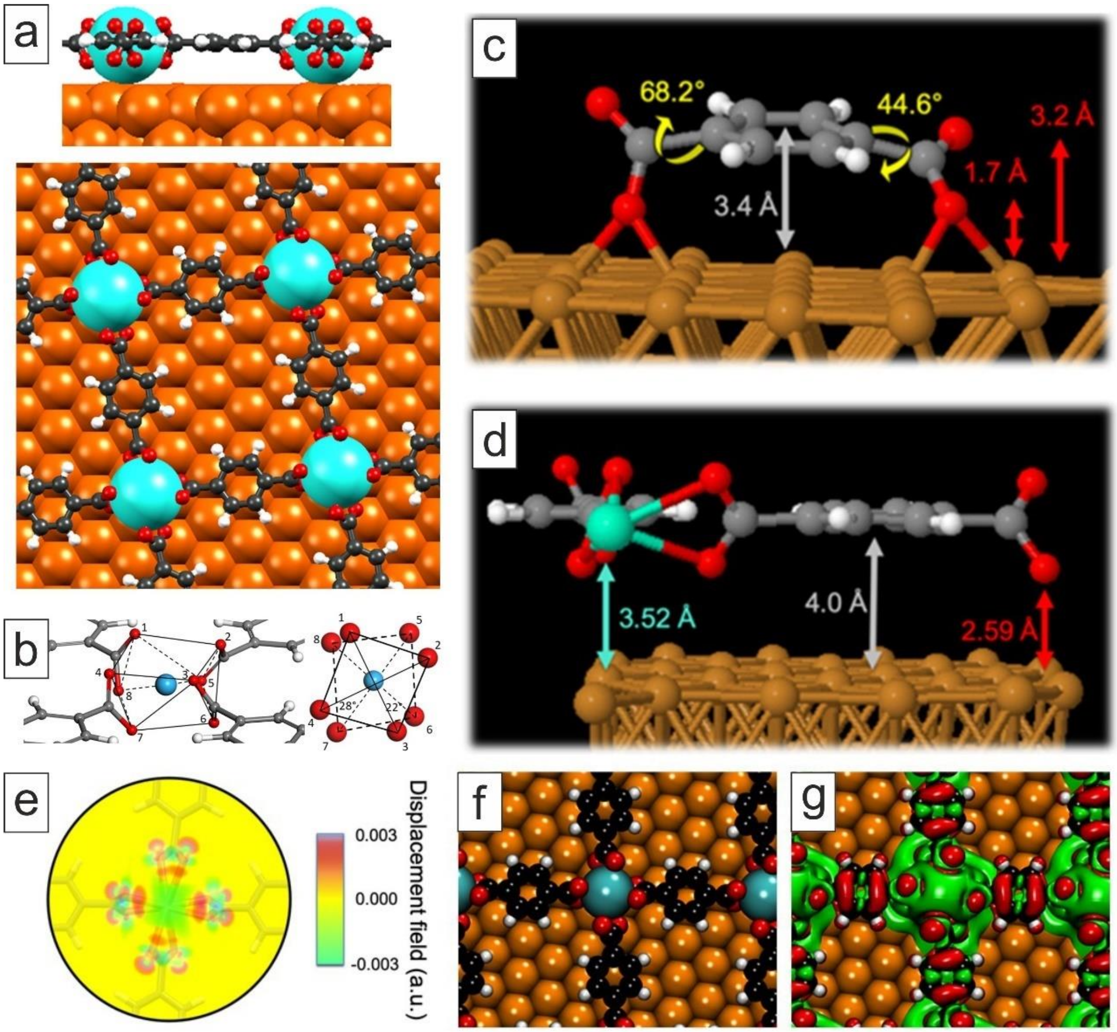

Figure 3-11 DFT calculations on Dy-TDA coordination network structure and charge density difference plots of the Dy-TPA network on Cu(111).

a) Side (upper panel) and top (lower panel) view of a Dy-TPA coordination node. b) 3D and top view of the coordination polyhedron formed by the oxygens. c,d) Lateral view of the adsorption geometry of TPA(c) and TPA coordinated with Dy(d) on Cu(111). Most representative distances in this interface are indicated. White, grey, red, tan and green spheres correspond to H, C, O, Cu and Dy atoms respectively. e) 3D plot illustrating the difference between the electron charge density of the interacting system and the one of its non-interacting counterpart. The structure model of Dy-TPA on the Cu(111)surface is superimposed. Negative values(green)represent charge depletion, accounting for an ionic character of the Dy centre. Positive values (blue, red) indicate charge accumulation, highlighting the charge gained by the carboxylate moieties. f) Structural model and g) 3D charge density difference isosurface (with isovalues of 0.001 a.u.). Green isosurfaces represent charge depletion and red isosurfaces indicate charge accumulation.

and the magnetic anisotropy of the XMCD for grazing and normal incidence are well reproduced. The role of the substrate is simply limited to contribute to the conformation of the molecular species.

In addition, magnetization curves are measured for Dy-TPA centres at 6 K and fitted with the same model explained in the previous section (Figure 3-12c). The term D, representing the anisotropy energy takes again high negative values during the iterations, indicating strong easy axis anisotropy. In this case, to perfectly fit the

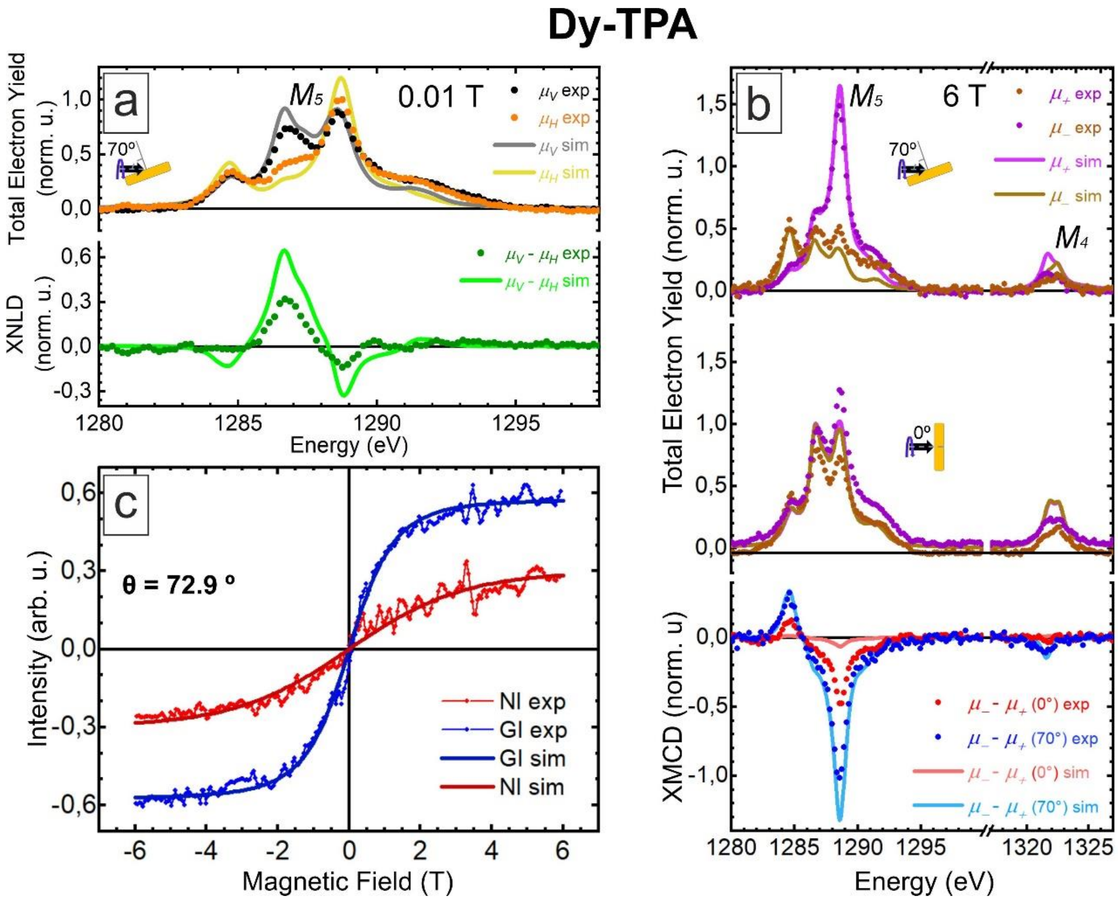

Figure 3-12 Magnetic properties of Dy centres on Dy-TPA networks.

a) XAS spectra acquired with vertical and horizontal linearly polarized light in the M_5 peak of the Dy (top) taken at 70° (GI) and XNLD (bottom) of Dy-TPA. b) XAS spectra acquired with circular polarized light, to the left and to the right in the $M_{5,4}$ edges of the Dy taken at 70° (GI, top) and at 0° (NI, middle) of Dy-TPA. Bottom panel displays the XMCD signal for both orientations. The solid lines correspond to the multiplet calculations of the system. c) Magnetization curves of Dy-TPA (b) on Cu(111) at T = 6 K, fitted by the same model employed for Dy-TDA.

experimental data, the calculations considered a tilted angle of the quantization axis with respect to the normal of the surface of 72.9°, being this axis slightly closer to the surface plane than for Dy-TDA case. As it has been predicted by DFT and multiplet calculations, the slight modification of the coordination geometry imposed by TPA molecules, produces a higher inclination of the easy axis of the quantization towards the surface, incrementing the difference between the XMCD signals in grazing and in normal incidences. Thus, the improvement in the magnetic properties comes from a reorientation of the easy axis of the quantization. Despite the increase of the magnetic anisotropy, magnetization curves for Dy-TPA networks do not show an opening of the hysteresis and, thus, no detectable internodal coupling is observed.

	Dy-TPA on Cu(111)	
Incidence angle (°)	0	70
$\langle L_z \rangle (\hbar)$	1.00(10)	2.77(28)
$\langle S_z \rangle (\hbar)$	0.60(6)	1.18(11)
$\langle J_z \rangle (\hbar)$	1.60(16)	3.95(40)
$M_T (\mu_B)$	2.20(22)	5.13(51)
$\Delta M_T (\mu_B)$	2.93(73)	

Table 3-2 Expectation values obtained from sum rules for Dy centres on TPA networks

Expectation values at the experimental temperature and at 6T field of orbital ($\langle \boldsymbol{L_z} \rangle$), spin ($\langle \boldsymbol{S_z} \rangle$), and total ($\langle \boldsymbol{J_z} \rangle$) moments, total magnetic moment ($\boldsymbol{M_T}$) and moment anisotropy ($\Delta \boldsymbol{M_T}$) obtained from XMCD sum rules at normal and grazing incidences for Dy-TPA.

3.3 Conclusions

In this chapter the electronic and magnetic properties of Dy-carboxylates metal-organic networks on Cu(111) have been explored. The networks have been engineered by an appropriate choice of ditopic organic linkers that preserve the coordination environment but exhibit different internodal distances.

Concerning the electronic properties, it has been shown that the nature of the coordinative bond between the carboxylate moieties and Dy atoms is fundamentally ionic, presenting a minor covalent contribution. For both Dy-TDA and Dy-TPA networks, Dy atoms are found in an +3 oxidation state, in contrast with the divalent oxidation state of Dy single atoms on Cu(111). Such finding shows the capability of changing the oxidation state of lanthanides upon metal-organic coordination on surfaces. Additionally, it has been observed that for both networks, the symmetry axis of the charge distribution of the 4f orbitals is located close to the surface plane.

Regarding the magnetic properties, it has been found that the easy axis of magnetization of both networks is placed close to the surface plane, even if the coordination symmetry axis points towards the out of plane direction. The magnetic properties of these networks depend on a delicate balance between the coordination geometry and the electrostatic interaction between oxygens from the carboxylic moieties and Dy. As it has been discussed, the smaller differences of the crystal field in Dy-TDA and Dy-TPA networks leads to an improvement in the magnetic anisotropy in the latter due to a slightly higher inclination of the easy axis. Both networks display a clear improvement of the magnetic anisotropy as compared to individual Dy atoms. Thus, metal-organic coordination is a powerful strategy in the quest for exploiting the potential of lanthanides as single atom magnets. Nevertheless, the networks do not show magnetic remanence, which could be a consequence of a short spin relaxation time or the interaction with conduction electrons or phonons coming from the molecular lattice or from the metallic substrate. A plausible way to discard some of such limitations could be to engineer the networks on decoupling supports, as it will be introduced in the last chapter of the thesis.

4. Tailoring energy level alignment and magnetic anisotropy by metal-exchange in lanthanide-directed networks

In this chapter, we introduce the design on Au(111) of dinuclear metal-organic networks based on Dy and Er.

Identical networks are obtained with Dy or Er as directing metals, without any structural difference at our level of spatial resolution. On the contrary, a study of these networks, employing STS, XAS, XMCD, XLD and magnetization curves, reveals that the electronic and magnetic properties are modified by the lanthanide exchange.

The nature of the metal-organic bonding with lanthanides lies in the 4f structure of their valence electrons[119]. Because of the inherent inner character of such orbitals, lanthanides display metal-organic bonds that are predominantly ionic, with a minor covalent contribution, in contrast to the d-block elements counterparts. As a result, the lanthanide coordination sphere tends to maximize the number of ligands, increasing the coordination number of lanthanides with respect to 3d metals, being this number mostly limited by the steric repulsion between the surrounding ligands.

In the last decade, several lanthanide-based metal-organic networks have been developed on surfaces [35,48,50,129,130], featuring different structural characteristic, but having in common mononuclear based coordination patterns. Just recently, non-periodic dinuclear Gd/Ce based metal-organic networks[27,29] and Au/Ce periodic heteronuclear structures[131] have been created on Au(111). The development of mechanisms to synthesize different lanthanide multinuclear metal-organic networks and the characterization of them is gaining impetus in materials science, in order to understand the influence of the environment in the physico-chemical properties of lanthanides. Such knowledge is mandatory in order to develop applications based on lanthanides.

In the first part of this chapter, the deposition and self-assembly of a ditopic linear ligand equipped with pyridyl groups (DPBP) on Au(111) is described. Next, by subsequent evaporation of Dy over a submonolayer DPBP sample held at 425 K, a dinuclear Kagome metal-organic network is formed and analysed. To our surprise the coordinative motif involves four pyridyl linking groups and a dinuclear node in drastic contrast to the behaviour of ditopic linkers equipped with carbonitrile moieties[132].

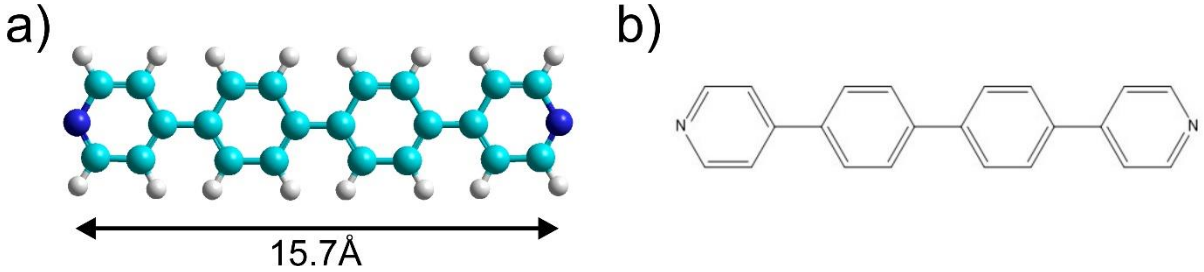

Figure 4-1 Chemical structure of DPBP molecule.

a) Atomistic model of DPBP linker, calculated from the relaxation of the structure in gas phase. Cyan balls represent carbon atoms, white balls represent hydrogen atoms and dark blue balls represent nitrogen atoms. The distance has been measured between terminal nitrogens. b) Structure of DPBP.

In the second part of the chapter, we focus on the possibility of modifying the coordination pattern by increasing the amount of molecules and Dy atoms, but preserving the stoichiometry. Close to the monolayer coverage, a new metallosupramolecular network emerges, which is described by a rhombic unit cell. The structure is going to be analysed and the differences and similarities in the electronic and magnetic properties between these two coordination patterns are addressed.

In the final part of the chapter, Dy atoms on the networks are exchanged by Er. The results show the same coordination patterns, but distinct electronic and magnetic properties, which are rationalized and discussed.

4.1 DPBP on Au(111)

The molecular linker to be used is [1,4-bis(4-pyridyl)-biphenyl] (to be termed DPBD in short), which is a linear ditopic organic ligand equipped with pyridyl groups at its termini to steer coordination(Figure 4-1), as previously found in literature [133–136].

First, DPBD was deposited at varying coverages on Au(111) held at RT. When the coverage is low, the molecular species form supramolecular wires able to cross the herringbone reconstruction (Figure 4-2a). A closer inspection of these nanostructures shows that they are mainly driven by two-fold coordination of DPBP species with gold adatoms from the surface[137]. The increase of the molecular coverage induces a different self-assembly. Due to higher molecular pressure, the DPBP species form a more compact and disordered reticular self-assembly (Figure 4-2b). Such self-assembly is stabilized by two distinct interactions. The first one is the two-fold coordination with gold adatoms present in the previous stage. The second interactions are hydrogen bonds between pyridyl groups and the hydrogen atoms of adjacent species (Figure 4-2c).

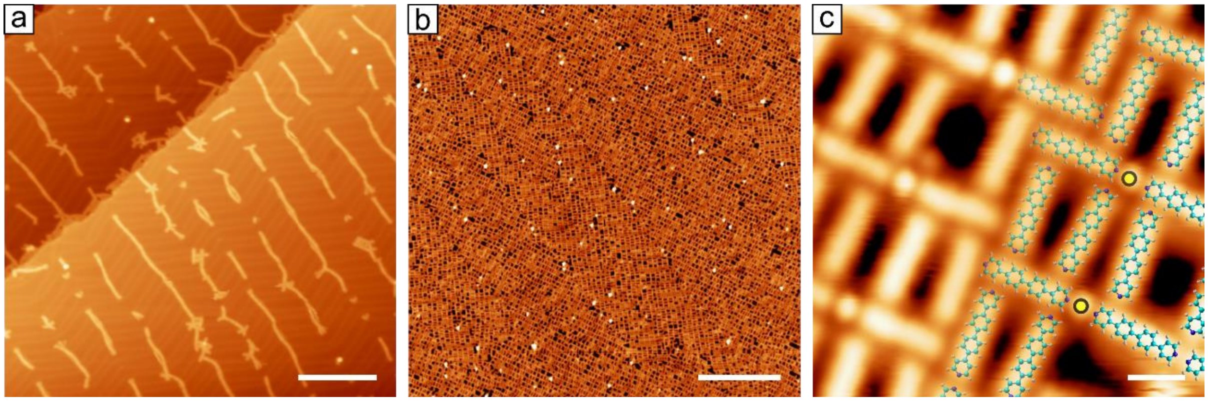

Figure 4-2 Self-assembly of DPBP on Au(111).

a) Long range STM image of low coverage of DPBP on Au(111). The wire structure is stabilized by 2-fold coordination with gold adatoms (V_{Bias} = 0.50 V; I_t = 50 pA; Scale bar: 20 nm). b) Long range STM image of high coverage of DPBP on Au(111) (V_{Bias} = 0.50 V; I_t = 100 pA; Scale bar: 40 nm). c) High resolution STM image of high coverage of DPBP on Au(111) with a superimposed atomistic model. The yellow balls correspond to gold adatoms. The structure is stabilized by hydrogen bonds and coordination with gold adatoms (V_{Bias} = 0.30 V; I_t = 50 pA; Scale bar: 1 nm).

4.1.1 Formation of Kagomé dinuclear Dy-DPBP coordination metal-organic network on Au(111)

Deposition of Dy and subsequent annealing at 425K during half an hour with a metal:ligand stoichiometry of 1:1 leads to the formation of big patches of coordination networks, exhibiting a Kagome pattern than can be extended by hundreds of nanometres (Figure 4-3a). This lattice is very homogeneous, with no defects in tens of nanometres (Figure 4-3b). The coordination nodes are visualized by a metallic STM tip as bright protrusions. To gain further insight on the nature of the node, a tip functionalized with CO has been used. The result is the acquisition of high quality STM images, which show that the nodes host two Dy atoms (Figure 4-3c). The molecular architecture can be described by the vector basis $\overrightarrow{b_1} = (22.0 \pm 0.5)$ Å and $\overrightarrow{b_2} = (22.1 \pm 0.5)$ Å, with unit cell vectors $\overrightarrow{c_1} = (43.9 \pm 0.5)$ Å and $\overrightarrow{c_2} = (43.5 \pm 0.5)$ Å, forming an angle of $\theta = (63 \pm 5)°$. By superimposing atomistic models calculated in gas phase to well calibrated STM images, it is possible to infer the projected distance between Dy atoms in a metallic centre. In this lattice, the Dy-Dy distance is (3.3 ± 0.5) Å, and the distance between Dy and the closer nitrogen atoms Dy-N is (2.4 ± 0.5) Å. Additionally, the images obtained with the CO tip show the molecular linkers featuring a dentated appearance. This effect is associated to the rotation of the aryl moieties, as a consequence of the steric repulsion between hydrogens in opposite aryl units, as it has been previously observed in other pyridyl equipped species[138].

4.1.2 Switching from Kagome to rhombic Dy-DPBP coordination network by increasing the molecular pressure

By preserving the metal:ligand stoichiometry to 1:1, but exactly depositing the double of DPBP and Dy on Au(111), and subsequent annealing at 425 K during half an hour, a new

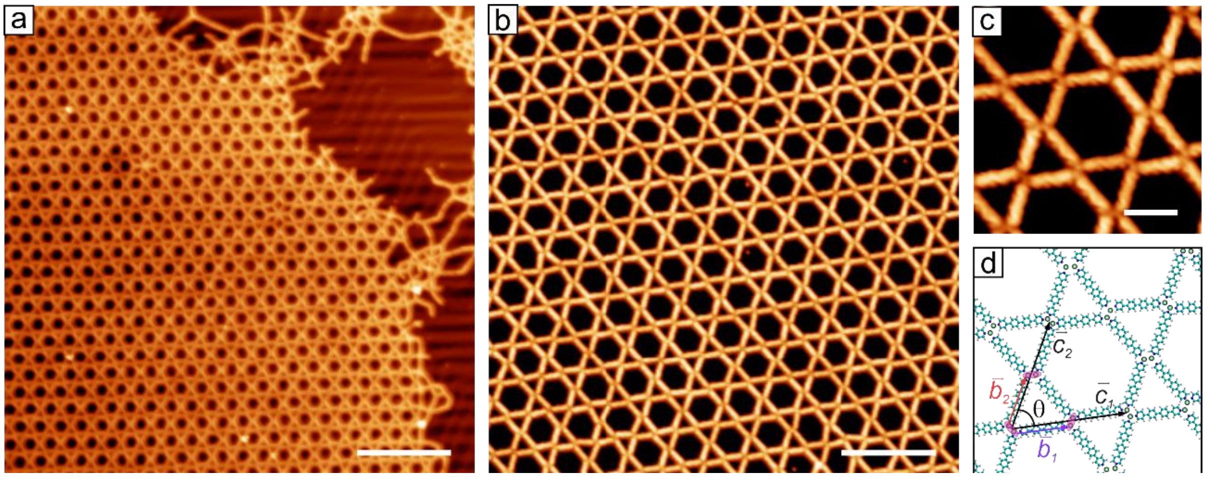

Figure 4-3 Dy-DPBP Kagome coordination network on Au(111).

a) Long range STM image showing a big patch of the Kagome lattice (V_{Bias} = 0.50 V; I_t = 50 pA; Scale bar: 20 nm). b) Medium range STM image of Dy-DPBP Kagome lattice, showing the high degree of homogeneity of the structure (V_{Bias} = -0.30 V; I_t = 1000 pA; Scale bar: 10 nm). c) High resolution STM image taken with a functionalized CO tip in constant current mode. The image reveals the dinuclear nature of the coordination nodes (V_{Bias} = -0.30 V; I_t = 1500 pA; Scale bar: 2 nm). d) Atomistic model of the coordination pattern showing the unit cell. The three orientations of the nodes are marked in pink. The basis vectors are $\overrightarrow{b_1} = (22.0\ \pm 0.5)$ Å (in blue) and $\overrightarrow{b_2} = (22.1\ \pm 0.5)$ Å (in red). The vectors of the unit cell are $\overrightarrow{c_1} = (43{,}9\ \pm 0.5)$ Å and $\overrightarrow{c_2} = (43{,}5\ \pm 0.5)$ Å. The angle between the unit cell vectors is $\theta = (63\ \pm 5)°$.

metal-organic network is found, described by a rhombic unit cell. This network is the result of an increase of the supramolecular pressure, since it is obtained for close to a monolayer coverage (Figure 4-4a). The lattice has concomitant few defects and shows some degree of molecular flexibility, which alters the long-range order (Figure 4-4b). A more detailed inspection with a CO functionalized tip reveals that the nodes are also dinuclear (Figure 4-4c). Additionally, it is possible to observe the dentated resolution of the molecules, indicating the rotation of the aryl moieties by steric hindrance. The structure can be rationalized by a rhombic network, whereby the vectors of the unit cell are $\overrightarrow{a_1} = (22{,}4\ \pm 0.5)$ Å and $\overrightarrow{a_2} = (22.2\ \pm 0.5)$ Å, spanning an angle of $\theta = (49\ \pm 5)°$ between them (Figure 4-4d). Superimposing atomistic models on the STM images, the intermetallic distance Dy-Dy obtained in this case is $(2.9\ \pm 0.5)$ Å and the metal-ligand distance Dy-N is $(2.4\ \pm 0.5)$ Å. These results are further confirmed by DFT calculations, represented in the inset of Figure 4-4c.

4.1.3 Electronic and magnetic properties of Dy-DPBP dinuclear coordination networks

Once the Dy-DPBP coordination networks have been grown and their structure have been characterized, the next stage is to inspect the electronic and magnetic properties of these lattices.

To that end, STS have been performed on selected points: i) the centre of a molecule involved in the coordination bond, and ii) the metallic centre (Figure 4-5a). Two resonances have been detected. The first one is placed at 1.47V, being tentatively

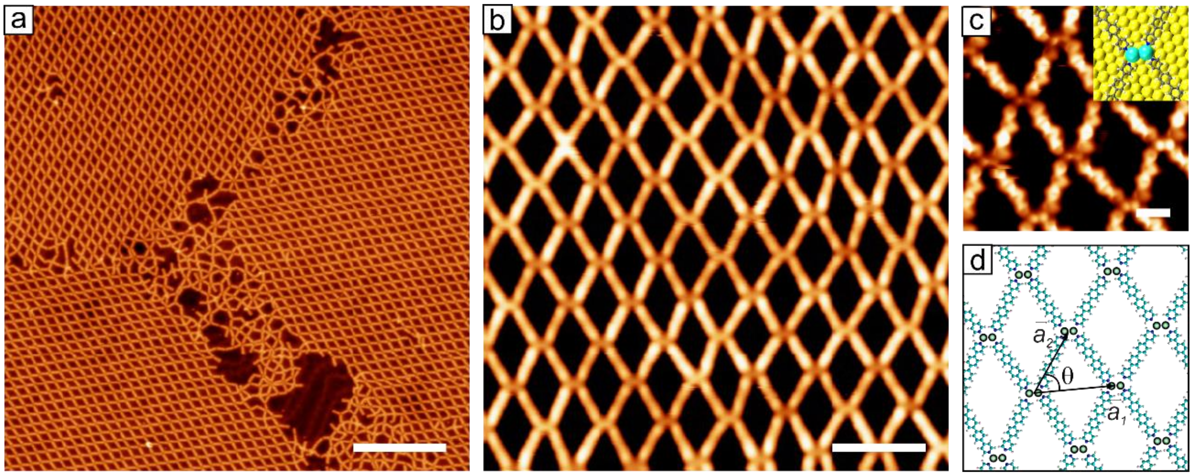

Figure 4-4 Dy-DPBP rhombic coordination network on Au(111).

a) Long range STM image of the rhombic coordination network. The structure covers almost all the surface (V_{Bias} = 0.20 V; I_t = 120 pA; Scale bar: 20 nm). b) Medium range STM image of the structure. The structure shows homogeneity in the medium range distances (V_{Bias} = -1.00 V; I_t = 50 pA; Scale bar: 4 nm). c) Constant height STM image taken with a functionalized CO tip. The nodes are composed by two Dy atoms in the centre (V_{Bias} = 0.005 V; Scale bar: 1 nm). The inset is a DFT simulation of the Dy-DPBP rhombic network. d) Atomistic model of the rhombic coordination network. The green balls represent Dy atoms. The vectors of the unit cell are $\overrightarrow{a_1} = (22{,}4\ \pm 0.5)$ Å and $\overrightarrow{a_2} = (22.2\ \pm 0.5)$ Å, forming an angle of $\theta = (49\ \pm 5)$º

assigned to the LUMO of the molecule, whose spatial distribution is shown by acquiring a dI/dV map at such voltage (Figure 4-5b, left panel).

The second resonance is found at higher energies, at 2.01V, and it is assigned to the metallic node since the spatial distribution of such state is located over the node (Figure 4-5b, right panel).

An analogous electronic structure can be observed in the rhombic lattice. Herein, the main peaks are found at 1.46V and 1.96V, corresponding to the LUMO of the molecule and the Dy state respectively, as it is shown in the dI/dV maps (Figure 4-5c).

To reveal and compare the magnetic properties of both systems, XAS, XMCD, XLD and magnetization curves have been performed (Figure 4-6), considering two main directions determined by the angle of incidence of the beam with respect to the sample, at 0° (NI) and at 70° (GI).

The samples were grown and explored by STM in situ prior to the magnetic measurements at 1.6 K. By following this protocol, no formation of metallic clusters that could contribute to the magnetic signal was detected.

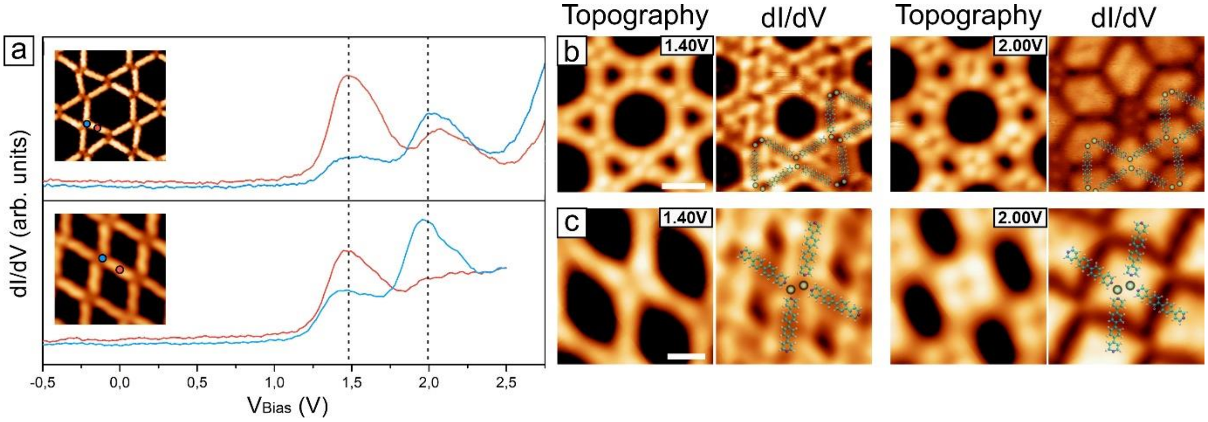

Figure 4-5 Electronic structure of Dy-DPBP coordination networks.

a) STS of the Kagome (upper panel) and rhombic (lower panel) Dy-DPBP lattices. The insets are STM images showing the positions where the spectra were taken. The dashed lines mark the electronic states of the Kagome structure (STS parameters: V_{mod} = 20 mV; f = 723 Hz; 25 ms integration time; Upper panel: 700 points/spectra; Lower panel: 400 points/spectra). b) Topography and dI/dV maps of the Kagome lattice, with a superimposed atomistic model (I_t = 200 pA; Scale bar: 2 nm). c) Topography and dI/dV maps of the rhombic lattice, with a superimposed atomistic model (I_t = 50 pA; Scale bar: 1 nm).

The XAS measurements of both lattices are very similar, featuring three distinct peaks in the M_5 edge. The third one is the most intense in both cases, which is characteristic of the oxidation state Dy^{3+} (Figure 4-6a,d)[93]. To further confirm these results, multiplet calculations for Dy on the rhombic configuration were performed assuming an oxidation state Dy^{3+} and Dy^{2+}. As it is shown in the inset of Figure 4-6d, calculations considering the divalent state miss some of the main characteristics of the M_5 edge structure. On the other hand, calculations supposing Dy^{3+} fit the experimental curve with a high degree of accuracy, confirming the oxidation state.

Magnetic measurements have been performed applying magnetic fields of 6 T (in the direction of the beam incidence) unless other conditions are expressed. The XMCD curves of the networks show that both of them present a strong in plane magnetic anisotropy (Figure 4-6a,d). It has not been observed the opening of hysteresis cycle during the measurements of the magnetization curves in any of the networks (Figure 4-6b,e).

To explore the charge anisotropy of both networks, XLD measurements with low magnetic field (0.05 T) have been performed (Figure 4-6c,f). The results show that both lattices present the same charge distribution of the Dy atoms.

By applying the sum rules[98,125] to the normalized XAS and XMCD measurements, the expectation values of the angular, spin and total moments, as well as the total magnetic moment is derived (Table 4-1). From these values it is clear that the magnetic anisotropy is higher for the rhombic lattice. Looking at the magnetization curves, it can be deduced that the samples are not fully saturated, since the slope is not perfectly zero at the highest magnetic field. This lack of saturation is associated to the contribution of different rotational domains during the magnetic measurements, since the diameter of the beam

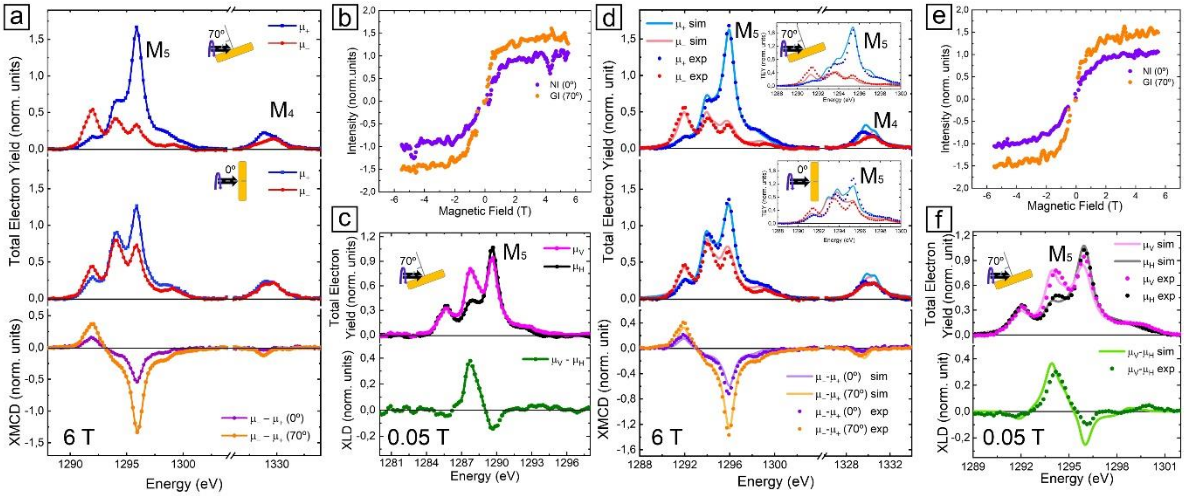

Figure 4-6 Magnetic structure of Dy-DPBP coordination networks.

(a-c) Kagome Lattice; (d-f) Rhombic lattice. (a, d) XAS with positive (μ_+, blue) and negative (μ_-, red) circularly polarized light and XMCD ($\mu_- - \mu_+$) taken at Dy $M_{4,5}$-edges at normal (0°, violet) and grazing (70°, orange) incidences (B = 6 T, T = 1.6 K). Solid lines on (d) correspond to multiplet calculations of the corresponding magnitudes. The intensity of the third peak in the M_5 edge indicates the oxidation state of Dy^{3+} in both networks, showing additionally a strong in plane magnetic anisotropy. The insets in (d) show the multiplet calculations of the M_5 edge considering an oxidation state Dy^{2+}. (b, e) Magnetization curves constructed by measuring the XMCD intensity at the highest peak of M_5-edge (T = 1.6 K). (c, f) XAS spectra acquired with vertical (μ_V, pink) and horizontal (μ_H, black) linearly polarized light and XNLD ($\mu_V - \mu_H$, dark green) taken at Dy M_5-edge at grazing (70°) incidence (B = 0.05 T, T = 1.6 K). Solid lines correspond to multiplet calculations. The orientation of the charge is the same in both networks.

is 1μm. Since the samples are not saturated, the $\langle J_Z \rangle$ values represent just lower boundaries of the saturation values, being $J_Z = 9/2$ for the Kagome network and $J_Z = 11/2$ for the rhombic network. In fact, multiplet calculations of a single domain of the rhombic network reveal that Dy features $J_Z = 15/2$.

	Dy centres on Kagome Dy-DPBP		Dy centres on rhombic Dy-DPBP	
Incidence angle	0°(NI)	70°(GI)	0°	70°
$\langle L_Z \rangle$ ($\hbar$)	1.32(10)	2.99(10)	1.75(18)	3.82(38)
$\langle S_Z \rangle$ ($\hbar$)	0.75(23)	1.38(38)	0.94(10)	1.82(18)
$\langle J_Z \rangle$ ($\hbar$)	2.07(33)	4.37(48)	2.69(28)	5.64(56)
M_T (μ_B)	2.82(56)	5.75(58)	3.63(36)	7.46(75)

Table 4-1 : Expectation values from sum rules of the magnetic moments and total magnetization of Dy in Dy-DPBP networks.

4.2 Tuning the electronic and magnetic properties of Ln-DPBD coordination networks by exchanging the lanthanide metal.

To explore the effects of an exchange of lanthanide in the properties of dinuclear networks, Dy was substituted by Er. Deposition of Er on a substrate containing a

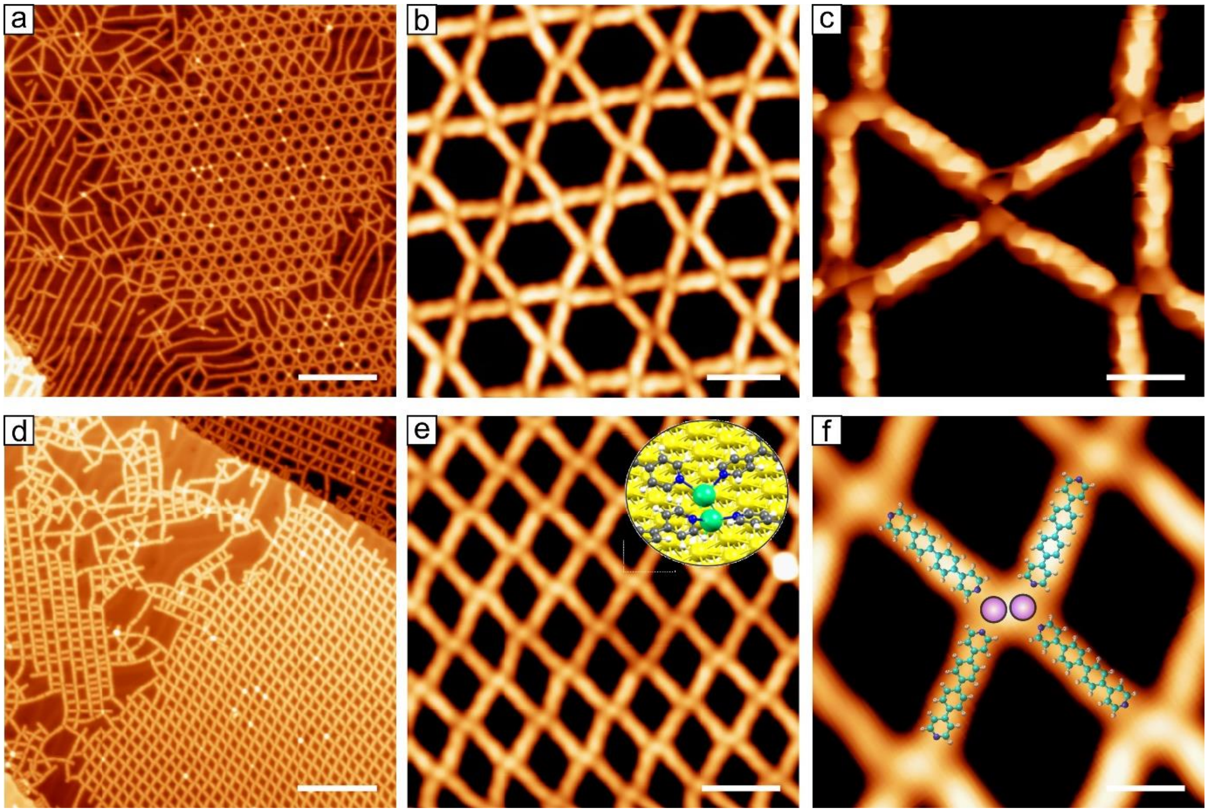

Figure 4-7 Structure of Er-DPBP coordination networks.

(a-c) Er-DPBP Kagome lattice. a) Long range STM image of Er-DPBP Kagome lattice (V_{Bias} = 0.30 V; I_t = 100 pA; Scale bar: 20 nm). b) Short range STM image of Er-DPBP Kagome lattice. The structure is identical to the Dy-DPBP counterpart (V_{Bias} = 0.10 V; I_t = 2000 pA; Scale bar: 3 nm). c) High resolution STM image taken with a functionalized CO tip showing the dinuclear nature of the nodes (V_{Bias} = 0.005 V; I_t = 50 pA; Scale bar: 1 nm). (d-f) Er-DPBP rhombic lattice. d) Long range STM image of Er-DPBP rhombic lattice (V_{Bias} = 0.50 V; I_t = 200 pA; Scale bar: 16 nm). e) Short range STM image of Er-DPBP rhombic lattice (V_{Bias} = 0.50 V; I_t = 200 pA; Scale bar: 3 nm). The inset is a DFT simulation of the Er-DPBP rhombic network f) High resolution STM image with a superimposed atomistic model. The purple balls represent Er atoms (V_{Bias} = 0.50 V; I_t = 200 pA; Scale bar: 1 nm).

submonolayer coverage of DPBP on Au(111), and subsequent annealing to 425K during half an hour, leads to the formation of a Kagome coordination network (Figure 4-7a,b). This structure features the same characteristics as its homologous based on Dy, including the unique dinuclear node, as it can be observed in high resolution STM images obtained with a CO tip (Figure 4-7c). Increasing both the amount of molecules and Er, but preserving the stoichiometry, the rhombic coordination network can be obtained (Figure 4-7 d-e). The structural characteristics of the Er-DPBP rhombic network are essentially the same as the Dy-DPBP counterpart. DFT calculations also supports this affirmation (Figure 4-7e inset), showing a similar structure.

Nevertheless, even if the structures obtained with Dy and Er are the same, the electronic and magnetic properties are altered due to the lanthanide exchange. By making STS measurements on top of the centre of a coordinated linker and on the Er atoms, it is possible to observe two different resonances (upper panel of Figure 4-8a). Following the same analysis done for the Dy-DPBP networks, the resonance at 1.75V is assigned to the

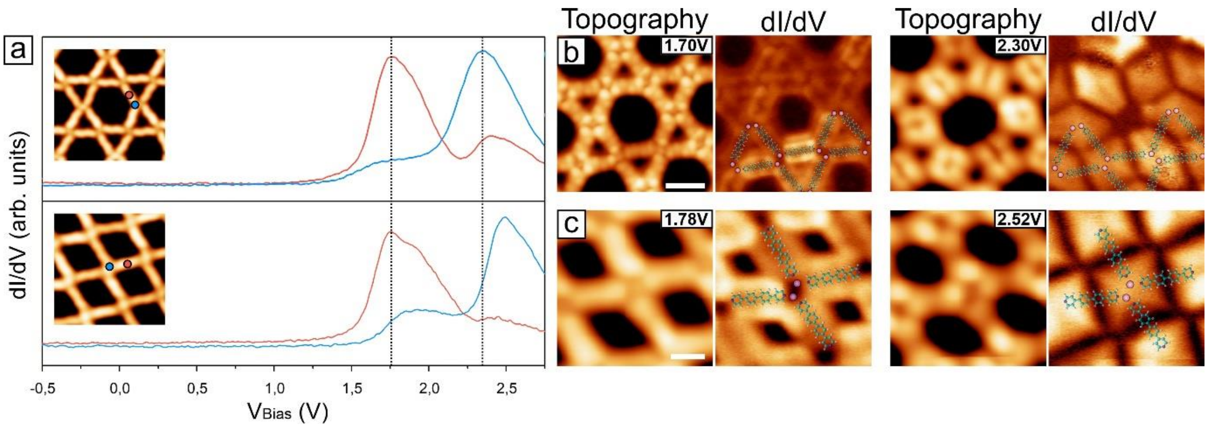

Figure 4-8 Electronic structure of Er-DPBP coordination networks.

a) STS of the Kagome (upper panel) and rhombic (lower panel) Er-DPBP lattices. The insets are STM images showing the positions where the spectra were taken. The dashed lines mark the electronic states of the Kagome structure (STS parameters: V_{Mod} = 20 mV; f = 723 Hz; 25 ms integration time; 700 points/spectra). b) Topography and dI/dV maps of the Kagome lattice, with a superimposed atomistic model (I_t = 150 pA; Scale bar: 2 nm). c) Topography and dI/dV maps of the rhombic lattice, with a superimposed atomistic model (I_t = 100 pA; Scale bar: 1 nm).

LUMO of the species (see dI/dV map in Figure 4-8b). In addition, the resonance at 2.35 V is associated to the dinuclear node (see Figure 4-8b). The same electronic states are manifested in the Er-DPBP rhombic lattice (lower panel of Figure 4- 8a). In this case, the LUMO state is placed at 1.75V and the node state at 2.50 V, the latter shifted 0.15 V away when compared to the same state in the Kagome structure (see Figure 4-8c for the spatial distribution of the electronic states).

Comparing the electronic properties between Dy- and Er- directed networks, it is worth to observe how the lanthanide exchange modifies the energy level alignment of the orbitals (Figure 4-9). For both Kagome and rhombic networks, the exchange of Dy by Er produces an energy shift to energies further away from the Fermi level. To shed some light on the origin of this shifting, PDOS is calculated for Dy- and Er-DPBP rhombic networks, which results are in good agreement with the experimental evidence (Figure 4-9b inset). On- going calculations about the Kagome Dy- and Er-directed networks are being run at the time of submission of this thesis.

Altogether, our results reveal that is possible to build dinuclear lanthanide metal-organic networks preserving the chemical structure, while tuning the energy alignment of the electronic states just by modifying the lanthanide employed.

The analysis of the magnetic properties of the coordinated Er centres reveals a different behaviour compared with its Dy homologous. XAS spectroscopy shows a structure of three peaks in the M_5, where the second peak for positive polarization is much more intense than the others (Figure 4-10a, top and middle panel). This feature is a fingerprint of the oxidation state Er^{3+} as it has been previously addressed for Er atoms on metallic

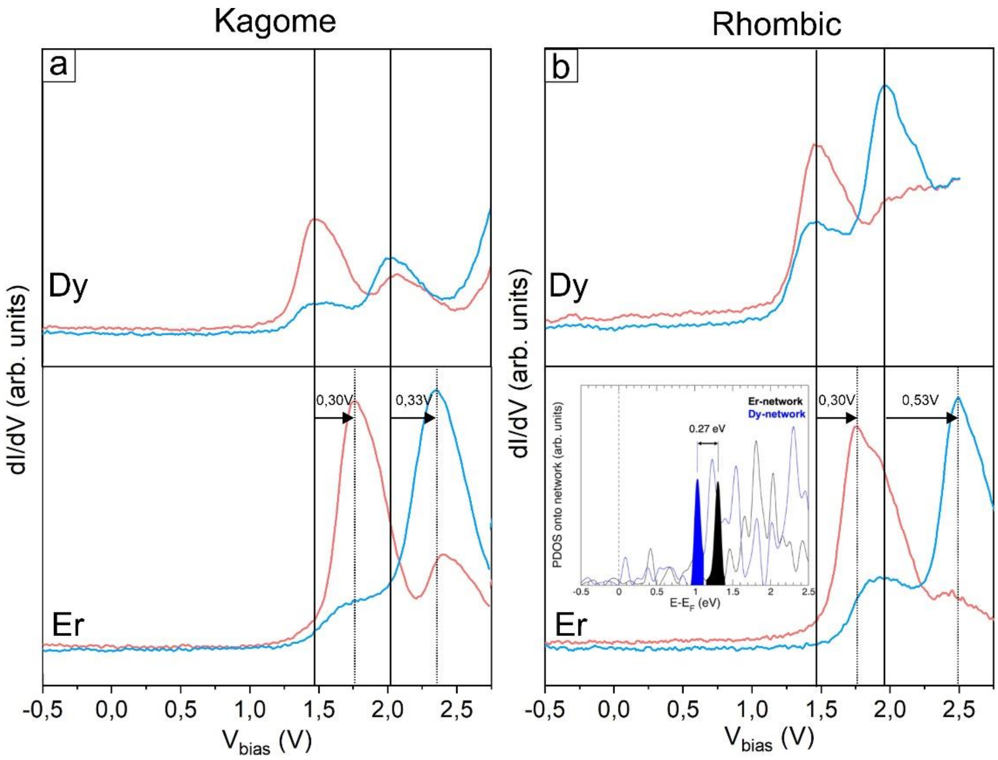

Figure 4-9 Electronic structure comparative between Dy- and Er-DPBP coordination networks.

a) STS of Dy-DPBP (upper panel) and Er-DPBP (lower panel) Kagome lattices. b) STS of Dy-DPBP (upper panel) and Er-DPBP (lower panel) rhombic lattices. The metal exchange from Dy to Er produces an energy shift to higher energies. The inset is the PDOS for both rhombic networks. It reflects the shifting to higher energies of the electronic states of the rhombic structures by the exchange of Dy by Er.

substrate[93]. Regarding the magnetic anisotropy, XMCD spectra taken both in NI and in GI feature identical characteristics with a slightly more intense signal coming from the NI (Figure 4-10a, bottom panel). To gain more insight into the magnetic behaviour of this system, magnetization curves for both orientations have been measured. The results display highly similar curves, showing that the GI curve presents a more squared shape (Figure 4-10b). Field dependent XMCD measurements in the range of +1 T to -1 T confirms the slightly bigger slope of the curve in GI (Figure 4-10b, inset), indicating an easy axis of the magnetization closer to the surface than to the normal plane.

Additionally, XNLD measurements with low magnetic field of 0.05 T in GI are recorded. The result shows that Er-DPBP presents a charge anisotropy with the peaks inverted as compared to the Dy-DPBP networks, indicating that the charge distribution of the Er ions is the opposite than the Dy counterparts (Figure 4-10c).

To unravel the origin of the magnetic properties of this system, multiplet calculations have been performed (4-10a,c). At this point, it is important to remark that since XMCD is not a single atom technique, the results obtained are an average of the contributions of the different orientational metallosupramolecular domains that are concomitant to the synthesis of the networks. To consider these contributions, GI XMCD spectra have been

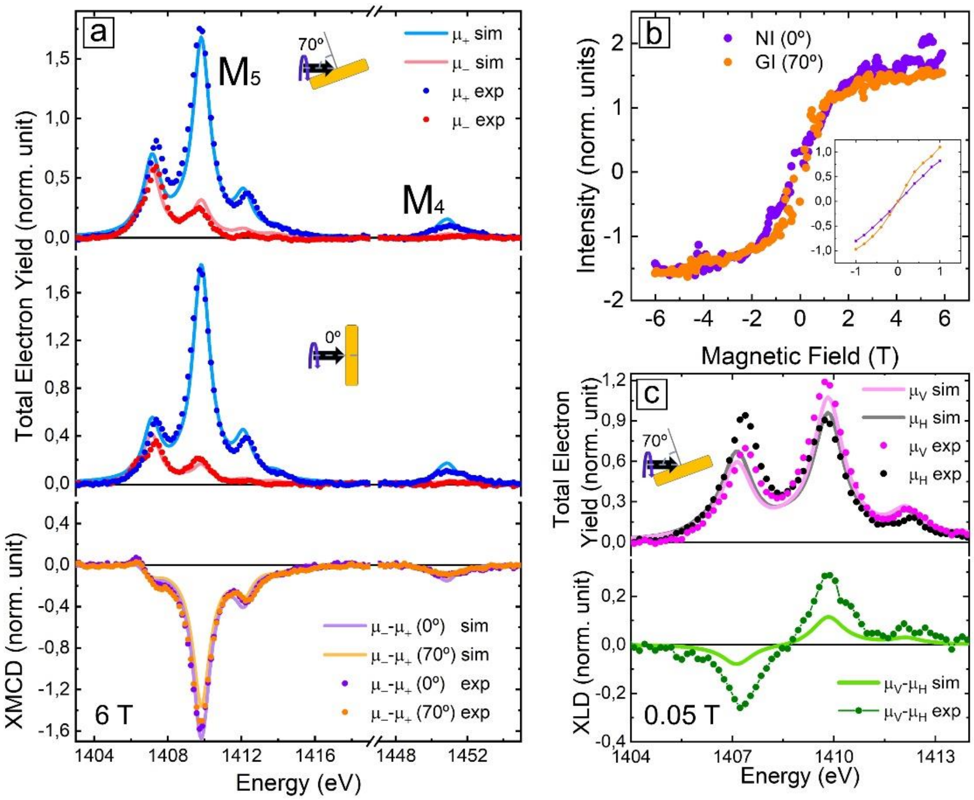

Figure 4-10 Magnetic structure of Er-DPBP rhombic lattice

a) XAS with positive (μ_+, blue) and negative (μ_-, red) circularly polarized light and XMCD ($\mu_- - \mu_+$) taken at Er $M_{4,5}$-edges at normal (0°, violet) and grazing (70°, orange) incidences (B = 6 T, T = 1.6 K). The intensity of the second peak in the M_5 edge indicates the oxidation state Er^{3+}. b) Magnetization curves constructed by measuring the XMCD intensity at the highest peak of M_5-edge (T = 1.6 K). The inset shows field dependent measurements of XMCD intensity for fields ranging from 1 T to -1 T. The higher slope of the magnetization in GI indicates an easy axis closer to that direction (c) XAS spectra acquired with vertical (μ_V, pink) and horizontal (μ_H, black) linearly polarized light and XNLD ($\mu_V - \mu_H$, dark green) taken at Er M_5-edge at grazing (70°) incidence (B = 0.05 T, T = 1.6 K). Solid lines correspond to multiplet calculations.

calculated for different azimuthal angles (Figure 4-11a). These simulations indicate that there is a preferential orientation of the magnetization in the plane. Besides, our calculations show that the similar intensity of the XMCD signals comes from the azimuthal average produced by the measurement of different domains. In fact, a XAS and XMCD multiplet calculations averaging the signal by the different azimuthal contributions allow to reproduce the experimental curves with a high degree of agreement. Polar angle dependent XMCD multiplet calculations reveal that the magnetization possesses an easy axis tilted 50° with respect to the normal plane, being slightly closer to the plane of the surface, in agreement with the magnetization curves (Figure 4-11c). Proceeding the same way with the Dy centres, the azimuthal analysis shows that the in-plane easy axis of these nodes forms an angle of 90° with respect to the Er case (Figure 4-11b). The polar angle analysis shows an easy axis of the magnetization tilted 80° respect to the surface normal, which is considered mostly in plane.

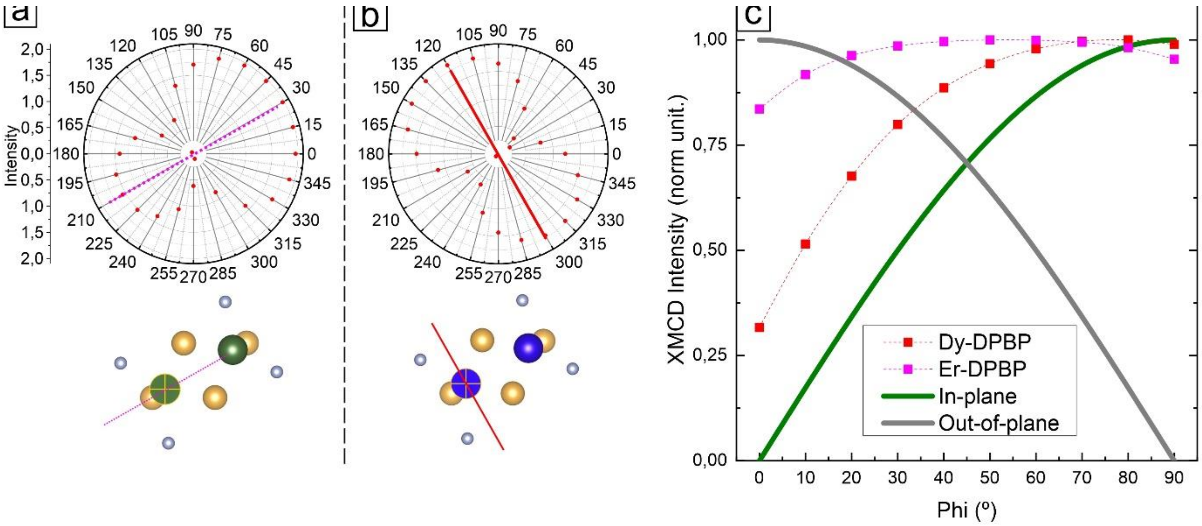

Figure 4-11 Multiplet calculations of the azimuthal and polar dependence of the XMCD signal for Er(Dy)-DPBP networks.

a, b) Polar plot of the multiplet calculations of the XMCD signal depending on the azimuthal angle for Er (a) and Dy(b). The simulations have been performed considering GI (70°). Lower panels are schemes of the preferential direction of the projection of the easy axis on the plane. Green (blue) spheres represent Er (Dy) atoms. The calculations have been performed over the atoms marked with a cross. Yellow spheres represent charges from the Au substrate. Grey spheres represent charges coming from the pyridyl groups. The pink dashed and the red solid lines indicate the preferential direction of the easy axis of the magnetization of each system. c) Plot of the XMCD signal depending on the polar angle for Er and Dy. Meanwhile the Er is tilted 50° from the surface normal, Dy displays an inclination of 80°, being not totally in plane. Grey and olive lines represent the limit cases of the magnetization totally out of plane and in-plane, respectively.

Application of the sum rules over the XAS and XMCD curves allows the obtention for the expected values of the magnetic moments (Table 4-2). The smaller values obtained in GI compared to NI are attributed to the incomplete magnetic saturation of the sample due to the contribution of the different rotational domains of the supramolecular architecture, as happens in the Dy-DPBP samples. In any case, the differences between both directions are inside the experimental error. The results show that the lower limit value of the total magnetic moment for the Er centres is $J_Z = 11/2$, the same result as for Dy-DPBP rhombic networks. Additionally, multiplet calculations confirms that for a single domain, the expected value for both Dy and Er would be $J_Z = 15/2$.

As it has been previously stated, the electronic and magnetic properties of the lanthanides are closely related to the charge distribution of the 4f electrons. This charge distribution adapts to the CF to minimize the electrostatic repulsion, resulting into the stabilization of one of the allowed J_z quantum states. In this context, Dy^{3+} is expected to show large out-of-plane J_z for an oblate charge density and Er^{3+} would display high values of J_z for prolate charge density in-plane with the symmetry of the charge. The XNLD spectra for Dy centres in dinuclear nodes feature the same peak structure as Dy-

	Er centres on rhombic Er-DPBP	
Incidence angle	0° (NI)	70° (GI)
$\langle L_Z \rangle$ ($\hbar$)	1.09(11)	1.00(10)
$\langle S_Z \rangle$ ($\hbar$)	5.11(51)	4.13(41)
$\langle J_Z \rangle$ ($\hbar$)	6.20(62)	5.13(51)
M_T (μ_B)	7.29(73)	6.13(61)

Table 4-2 Expectation values of the magnetic moments and total magnetization for Er centres on DPBP rhombic network

TDA/TPA centres from the previous chapter, indicating a prolate charge distribution with the symmetry axis oriented close to the surface. This configuration is compatible with the strong in plane magnetic anisotropy detected in these systems. On the other hand, the peak inversion manifested in the XNLD spectrum of the Er points to an inverted charge distribution compared to Dy. Assuming an oblate charge distribution due to the high J_z and taking into account the CF, it is expected that both the charge axis and the magnetic anisotropy easy axis adopt a 50°.

4.3 Conclusions

In this chapter, the synthesis of two different types of Dy-pyridyl dinuclear networks has been described, and a comparison between the electronic and magnetic properties of these systems has been stablished. Additionally, exchanging Dy by Er atoms produce identical supramolecular architectures but with a different energy states alignment. The exchange also alters the magnetic properties of the metal-organic network.

Deposition of Dy on a sample containing a submonolayer coverage of DPBP leads to the formation of a dinuclear metal-organic network showing a Kagome pattern. Increasing the coverages of Dy and DPBP preserving the stoichiometry give rise to the formation of a dinuclear rhombic network.

The lanthanide exchange produces identical dinuclear structures. Despite the fact that both metals present the same oxidation state 3+, the energy level alignment of unoccupied frontier orbitals of the networks shift towards higher energies in both coordination structures.

Regarding the magnetic properties, the experiments reveal the possibility to tune both the easy axis of the magnetization and the magnetic anisotropy of lanthanide metal-organic networks by exchanging the metallic atom. Multiplet calculations have allowed to determine the tilting of the easy axis of the magnetization of both metals, as well as its preferential direction respect to the plane. These insights have been invaluable to gain more understanding into the magnetic behaviour of these systems.

These findings allow to envision the engineering of bidimensional structures with tuneable electronic alignment and magnetic properties through lanthanide exchange.

Additionally, the dinuclear structures can be seen as experimental model systems to study the interactions between lanthanides inside a node.

We anticipate future experiments will deal with the synthesis of such dinuclear metallosupramolecular architectures on decoupling layers, targeting to characterize and study their magnetic properties minimizing the role of the metallic substrate underneath, in order to develop new paths to exploit their pristine physico-chemical properties.

5. Towards lanthanide-directed metallosupramolecular networks on graphene.

In this chapter, we introduce the seminal design of a lanthanide-directed coordination network on a sp^2 template (Gr/Ir(111)).

More in detail, we report the growth of Dy-carbonitrile coordination networks on Au(111) and Gr/Ir(111) and characterize them by STM and DFT, making emphasis in the similarities and differences regarding the employed substrate.

Metallic substrates are widely used as supports for the fabrication of coordinated networks, because of the ease to use them for standard surface techniques, allowing to explore by STM changes in the morphology of coordinated systems by modifying the crystal geometry or the metallic substrate. However, the use of metals as supports presents a major drawback, which is the interaction between the coordinated architecture and the metal. Such interaction, which varies depending on the metal and the morphology of the coordination networks, is not trivial and leads to the modification of the optical, electronic and magnetic properties of the adsorbed nanomaterial, most of the time in a detrimental fashion.

Recently, targeting to overcome this barrier, the growth of coordination networks has been successfully achieved on sp^2-hybridized high-quality layers such as h-BN[42] or Gr [121,139]. In the case of the present thesis, we have selected Gr on Ir(111) as a support for the following reasons. First, the protocols for growing Gr on Ir(111) are well known [140–143], making easier the reproducibility in our experimental set-up. Second, since the growing mechanism is self-limited, a full monolayer of Gr is guaranteed in the long-range regime, avoiding clustering of the molecules on remaining metallic patches, as it has been previously observed in molecular self-assembly experiments on insulator layers [144,145]. Third, Gr layers on metallic substrates have been deeply studied in the last decade because of their unique properties [142,143,146–153]. Such Gr layers can be grown on several metals, presenting distinct degree of interaction regarding the nature of the metal, being some of them highly interacting, as is the case of Gr/Ru(0001) [154–156]. For the purposes of the experiment, Gr on Ir(111) has been chosen because of the low interaction between Gr and Ir(111), which allows to consider the Gr as a decoupling layer from the Ir(111) substrate[154,157,158]. We expect that the growth of lanthanide coordination networks on Gr/Ir(111) will serve to seed light to several optical or magnetic properties of the networks. In this sense, the magnetic bistability of lanthanides on Gr/Ir(111) was recently introduced[17], opening new avenues for magnetic storage and quantum nanoscience.

As illustrated in Annex I, we selected distinct molecular backbones equipped with terminal carbonitrile or pyridyl functional groups. We discarded here the carboxylic moieties since they demand thermal activation for transforming into carboxylate linkers to coordinate with lanthanides, which would imply the desorption of the molecular species. After distinct attempts that were discarded by the irregularity of the formed metallosupramolecular patterns, a quasi-hexagonal nanoarchitecture based on carbonitrile-dysprosium coordination was achieved, which is the focus of this section.

In the first part of this chapter, the self-assembly of three-fold molecular species equipped with carbonitrile terminal functional groups is studied, describing the afforded structural supramolecular designs and their dependence upon thermal annealing. Next, the coordination of such species with Dy atoms is addressed, giving rise to a metal-organic Dy-directed network.

In the second part of the chapter, we reproduce the same methodology and study of the precursor in the absence and in the presence of Dy, but this time on Gr/Ir(111), as an archetype sp^2 substrate. A brief description of the method to grow Gr/Ir(111) is introduced, as well as the procedures to check the quality of the Gr layer, prior to the experiments. Next, the self-assembly of the species on Gr/Ir(111) is analysed, as well as the quasi-hexagonal Dy-coordinated phase obtained after the deposition of Dy, which is compared and almost identical to the one found on Au(111).

The main results of this chapter have been recently published by us in Chemical Communications[159].

5.1 BCNB on Au(111)

The (1,3,5-tris(40-biphenyl-400-carbonitrile)benzene (to be termed BCNB) is a three-fold symmetric ligand equipped with carbonitrile functional groups at the *para* positions of the terminal phenyl groups[160] (Figure 5-1). Carbonitrile group is known to stablish coordinative bonds with lanthanide atoms. From square and hexagonal coordination patterns to snub square Archimedean tiling, and even quasicrystals, the mixing of nitrile groups with lanthanides can result in a great variety of metallosupramolecular networks involving 3-, 4-, 5- and 6-fold mononuclear nodes[48,50,161,162]. Thus, the choice of this molecule is fully justified to take advantage of its great chemical affinity for coordination with lanthanides. The molecular linker is relatively big, measuring 22.1 Å between the extreme nitrogen atoms as seen in Figure 5-1.

First, the molecular species are deposited on a clean Au(111) substrate held at RT. STM imaging reveals that the species, featuring a tripod appearance, self-assemble into large islands (Figure 5-2a). This self-assembly is driven by the hydrogen bond interactions between terminal carbonitriles and hydrogens of the adjacent molecular species, as it has been previously described on other coinage metals[37,163,164]. The average projected distance of the CN···H bond is (2.6 ± 0.5) Å, obtained by superimposing atomistic models

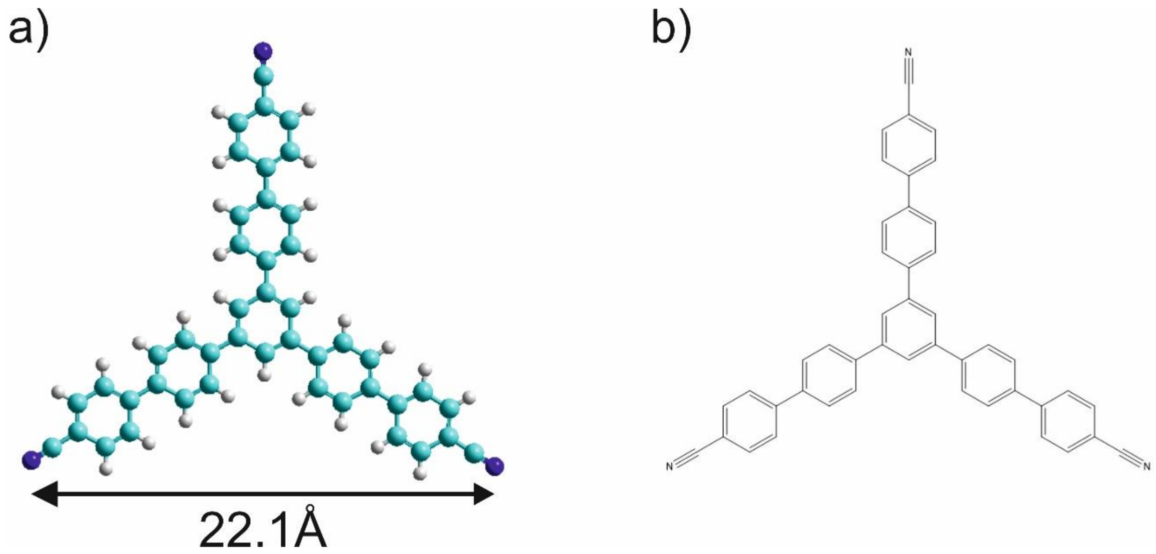

Figure 5-1 Chemical structure of a free standing BCNB species.

a) Stick and ball model of BCNB linker, which is obtained by relaxing the species in the gas phase (MM+, Hyperchem package). Carbon, nitrogen and hydrogen atoms are represented by green, cyan and white solid spheres, respectively. b) Chemical structure of BCNB.

on calibrated images. The molecular linkers form a hexagonal lattice (Figure 5-2b), being the modules of the vectors of the unit cell $|\overrightarrow{a_1}| = (17.4 \ \pm 0.5)$ Å, $|\overrightarrow{a_2}| = (17.5 \ \pm 0.5)$ Å, and spanning an angle of $\theta = (59 \ \pm 5)°$ between them.

After annealing the sample up to 373K for 30 minutes, a new metal-organic phase arises (Figure 5-3a). This phase does not show long-range order and it is based on the coordination of the carbonitriles groups with Au adatoms. Notably, it is observed that the lack of long-range order comes from the variety of the coordination nodes. Up to three different nodes are detected, one of them being 3-fold (Figure 5-3b) [160,165,166]and the other two 4-fold (Figure 5-3c,d) [167]. In the STM images, the Au adatom remains invisible, a phenomenon previously reported in several metal-organic coordination networks employing 3d metals [137,165,166,168].

5.1.1 On surface Dy-BCNB coordination metal-organic network on Au(111).

Deposition of a low amount of Dy atoms on a submonolayer coverage of BCNB on Au(111) held at RT and subsequent annealing at 373 K to promote molecular diffusion favours the formation of a new metal-organic phase (Figure 5-4a), coexisting with the purely non-coordinated BCNB phase. High resolution imaging and modelling allows to rationalize this new phase, identifying 4-fold and 5-fold nodes, which are assigned to Au and Dy metallic centres, respectively. Such assignment is based on the following reasoning:

i) The 4-fold nodes remain invisible to the STM and present the same geometry as the metal-organic BCNB-Au architecture reported above (Figure 5-4b).

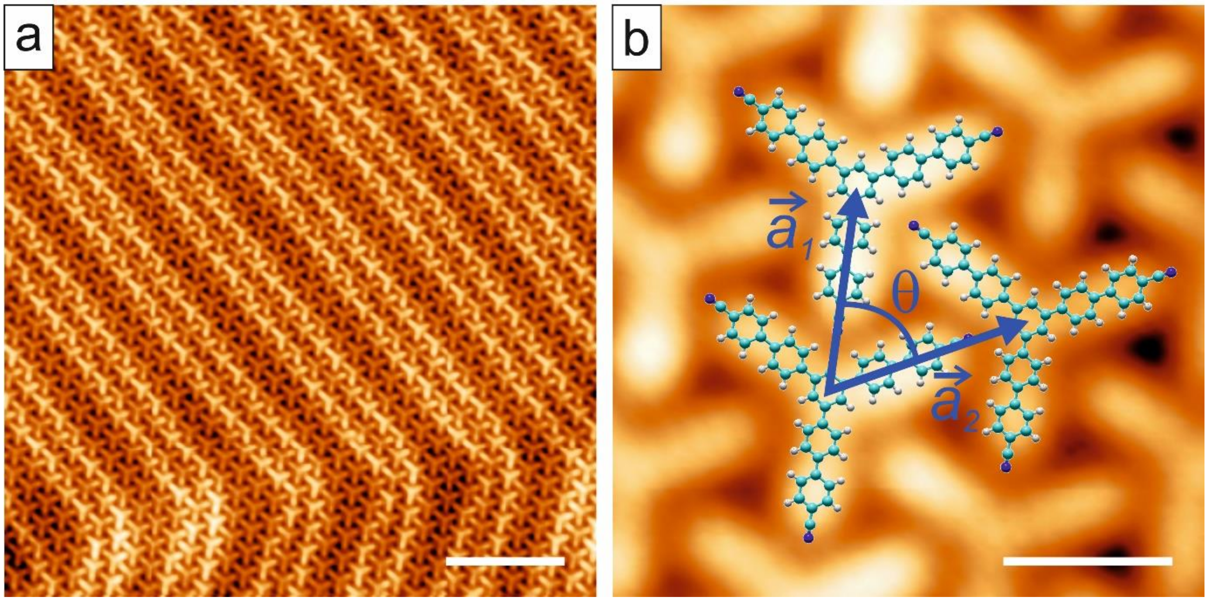

Figure 5-2 Self-assembly of BCNB on Au(111).

a) Long range STM image of BCNB molecules self-assembled on Au(111). It is possible to observe the herringbone reconstruction trough the layer of molecules (V_{bias} = -1.00 V; I_t = 100 pA. Scale bar: 10 nm). b) High resolution STM image of the BCNB self-assembly. Atomistic models of the molecules are superimposed. The self-assembly is stabilized by the interaction between carbonitrile and the hydrogen atoms of the surrounding molecules. The vectors of the unit cell are $\vec{a_1} = (17.4\ \pm 0.5)$ Å, $\vec{a_2} = (17.5\ \pm 0.5)$ Å and span an angle of $\theta = (59\ \pm 5)°$ (V_{bias} = -1.00 V; I_t = 100 pA. Scale bar: 2 nm).

ii) The 5-fold nodes only appear after the deposition of Dy and it has been previously reported that carbonitrile functional groups like to steer five-fold coordination nodes with lanthanides [29,47,48,50]. The metallic centre is imaged as a bright ball in the nodes, and the averaged projected distance of the molecules involved in the CN⋯Dy bond is (2.5 ± 0.5) Å, which is in good agreement with values reported in other lanthanide based coordination networks[129]. In addition, DFT calculations (inset of Figure 5-4d) reveal an average CN⋯Dy projected bond distance in the range from 2.6Å to 2.7 Å, in good agreement with the experimental results. Importantly, the Bader analysis performed over the Dy atom reveal a positive charge of $+2.35e^-$, compatible with a 3^+ oxidation state observed in previous Dy and Gd architectures [50].

An increment of the amount of deposited Dy and subsequent annealing of the substrate up to 373 K leads to the expression of a full metal-organic coordinated phase (Figure 5-5a).

In this case, we detect three distinct types of coordination nodes (Figure 5-5c). The majority node (65%) is five-fold and based on individual Dy atoms. Next in abundance (23%), we find a four-fold coordination node, which by similarity to the previous cases is assigned to Au atoms. Finally, there is a new and minority (12%) six-fold node. Though the node cannot be resolved in STM, by modelling it is rationalized as a dinuclear coordination node based on Dy centers. For a mononuclear node, the average CN⋯Dy

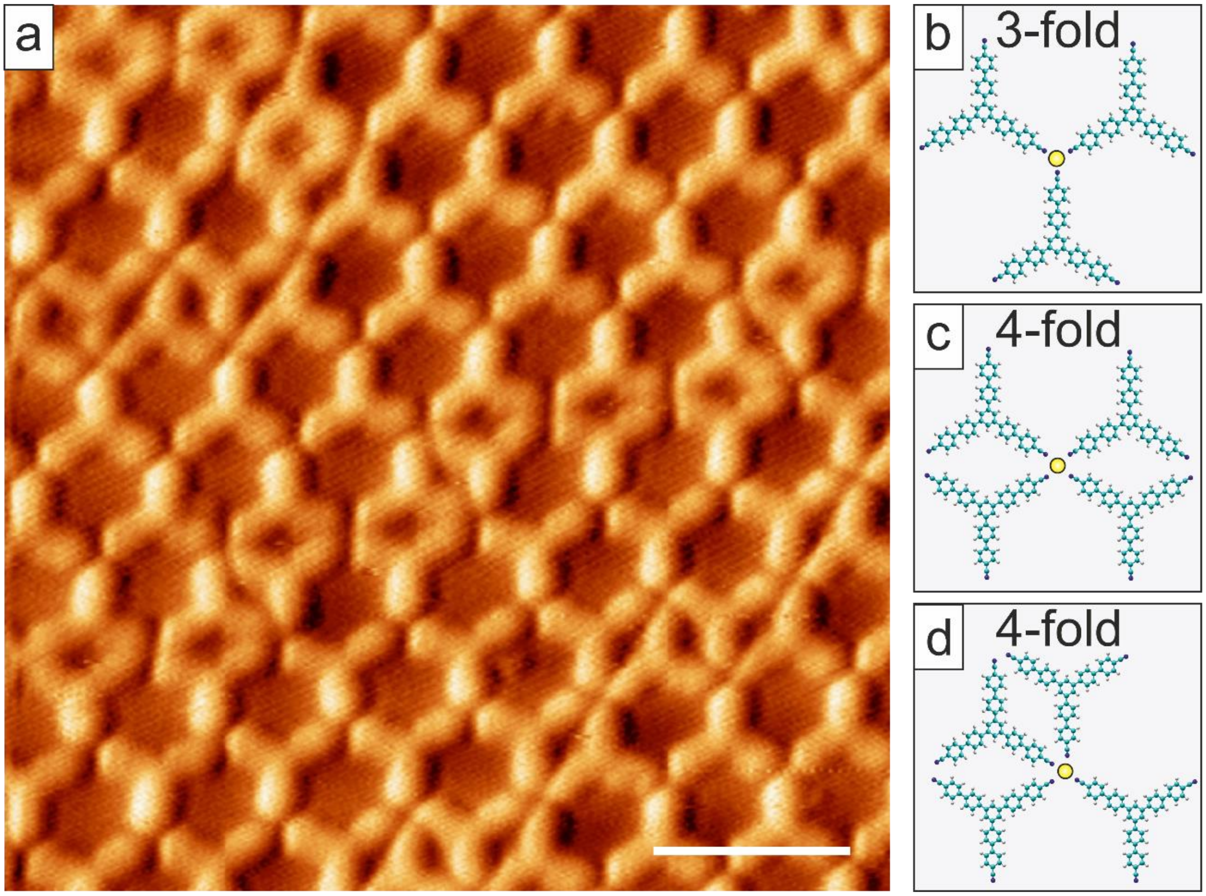

Figure 5-3 Assembly of BCNB on Au(111) after annealing.

a) STM image showing the self-assembly after annealing at 373 K a submonolayer coverage of BCNB on Au(111) (V_{bias} = 0.70 V; I_t = 130 pA. Scale bar: 3 nm). The new nanostructure is driven by coordination with gold adatoms and it is based on different kinds of nodes, one that is 3-fold and two that are 4-fold, displayed in b), c) and d) respectively. The yellow ball represents a gold adatom.

projected bond distances would be 4.5 ± 0.5 Å, and thus too long for a bond [169]. Discarded the possibility of a mononuclear Dy node, if we impose a model based on a dinuclear node, the CN···Dy would be 2.6 ± 0.5 Å, which is compatible with previous results and typical bond distances involving lanthanide coordination. Importantly, related dinuclear nodes have also been reported in Dy-directed carboxylate coordination networks[29].

5.2 BCNB on Gr/Ir(111)

Although the study of the electronic and magnetic properties of these networks on metals is very interesting and can shed light about how these properties are modified by different coordination patterns, there is a concomitant interaction with the metallic substrate, which can alter substantially the electronic, magnetic and optical properties of the coordinated architectures.

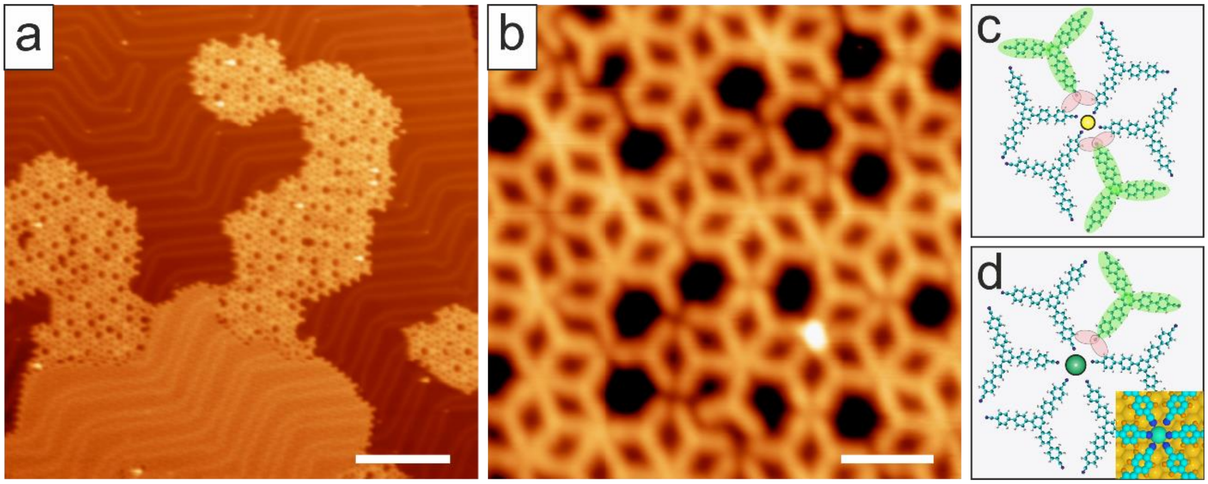

Figure 5-4 Dy-BCNB coordination network on Au(111) with low amount of Dy.

a) Long range STM image of the Dy-BCNB coordination network coexisting with the self-assembly phase on Au(111). The preservation of large non-coordinated islands is a signal of the low dosage of Dy (V_{bias} = -1.00 V; I_t = 25 pA. Scale bar: 20nm). b) STM image of the Dy-BCNB coordination network on Au(111). The formation of this phase is associated to a competition between coordination with Au adatoms and Dy atoms, forming new types of nodes (V_{bias} = -1.00 V; I_t = 100 pA. Scale bar: 3 nm). c) Scheme of 4-fold coordination nodes involving Au adatoms. The molecules marked in green are not involved in the coordination, but just stablish hydrogen bonds as illustrated by pink ellipses. d) Scheme of 5-fold coordination nodes involving Dy atoms. The Dy atom is represented by a green ball. The molecule highlighted in green is not involved in the coordination bond, being stabilized by the other molecules through hydrogen bonds. The inset corresponds to a DFT simulation, illustrating the 5-fold coordination between the carbonitrile groups and the Dy atom.

In addition, even if the Au(111) is considered a low interacting metal, it cannot be denied that the coordination with Au adatoms, concomitant to the substrate, is an undesired effect for the construction of lanthanide-based coordination networks. To avoid the contribution of adatoms and to minimize the effects of the interaction between the coordination network and the metallic substrate, it was decided to grow the lattice on top of a Gr/Ir(111) support.

Graphene grown on Ir(111) is considered a decoupling layer. In addition, it is easy to grow it in vacuum by preparing the Ir(111) crystal by repeated sputtering and high temperature annealing cycles (up to 1600 K) and exposing the hot Ir(111) crystal (1440 K) to an atmosphere of ethylene (CVD). When the ethylene enters in contact with the hot substrate, the pyrolysis of the molecule is produced, forming a monolayer of graphene covering the surface. Since the process is self-limiting, one monolayer is guaranteed[141]. The quality of the Gr is checked both by LEED and by STM. The LEED pattern of the sample shows six brighter spots, corresponding to the Ir(111) crystal, and additional spots associated with the Moiré pattern of the Gr[121,141], confirming the correct growth of the material (Figure 5-6a). By STM, the coverage and the cleanliness of the sheet of Gr are checked out (Figure 5-6b). The Gr layer covers the major part of the crystal, and the Moiré pattern can be identified, showing a periodicity of (24.9 ± 0.5) Å, in good agreement with previous experimental results[141].

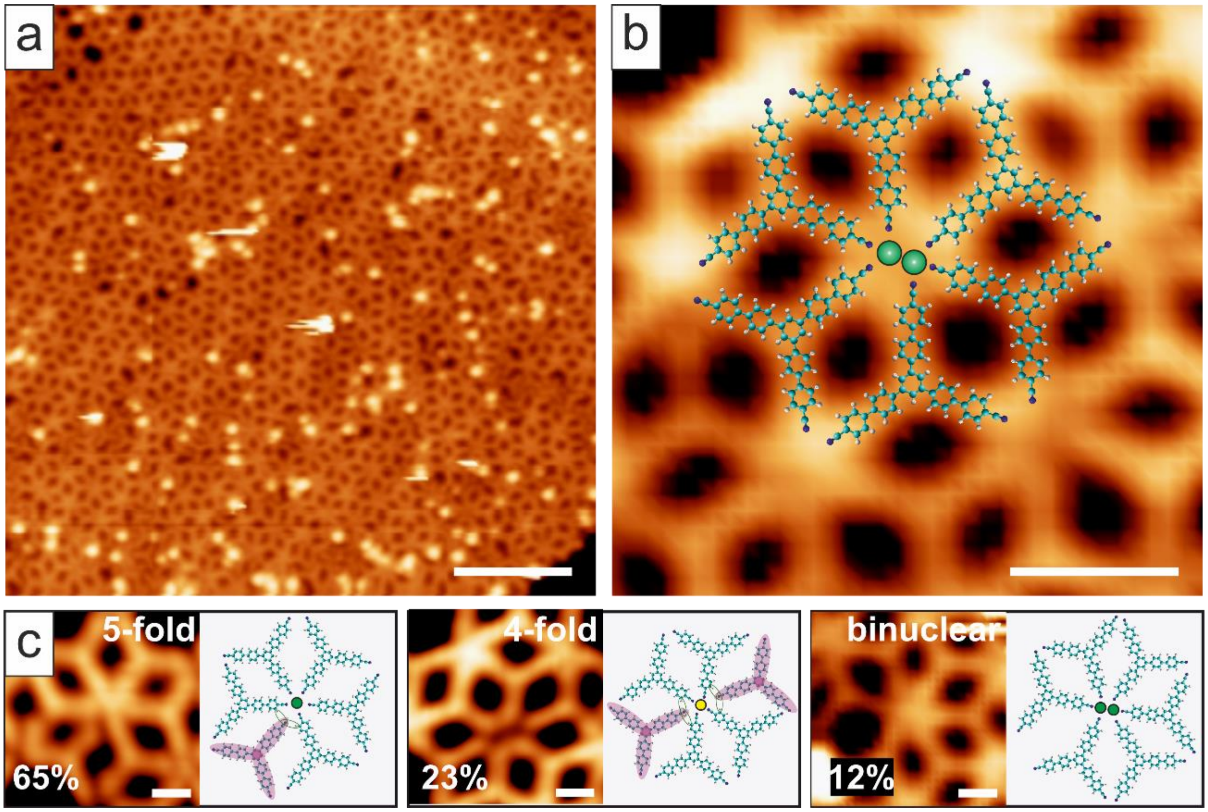

Figure 5-5 Dy-BCNB coordination network on Au(111).

a) Long range STM image of a patch of the Dy-BCNB coordination network covering the surface (V_{bias} = 0.50 V; I_t = 15 pA. Scale bar: 10 nm). b) Stick and ball model superimposed on a STM image showing a coordination node involving two Dy atoms in the centre. (V_{bias} = 0.50 V; I_t = 15 pA. Scale bar: 2 nm). c) High resolution STM images and corresponding atomistic models of the three different coordination nodes forming the structure. The molecules marked in pink are not participating in the coordination bond. The percentage in the corner corresponds to the frequency of each node in the coordinative network (V_{bias} = 0.50 V; I_t = 15 pA. Scale bar: 1 nm).

Once the substrate is ready, BCNB molecules are deposited on top of Gr/Ir(111) held at room temperature. In this case, the molecules self-assemble forming large islands. Two distinct phases are distinguished, to be termed α-phase and β-phase (Figure 5-7a). Both phases exhibit a distinct rectangular packing, which can be described by a basis and the lattice vectors. In the α-phase, the two molecules on the basis (marked in pink in Figure 5-7b) interact with each other though hydrogen bonding between the terminal nitrogen and the hydrogens in the ortho positions. The basis vector is $|\overrightarrow{b_1}| = (14.5\ \pm 0.5)$ Å and the lattice vectors are $|\overrightarrow{a_1}| = (29.4\ \pm 0.5)$ Å, $|\overrightarrow{a_2}| = (17.1\ \pm 0.5)$ Å, forming between them an angle of $\theta = (88\ \pm 5)°$. In the β-phase, the molecules on the basis (Figure 5-7c) also interact by hydrogen bonding, but in this case the nitrogens interact with the adjacent hydrogens in the meta positions. Herein, the basis vector is $|\overrightarrow{d_1}| = (20.7\ \pm 0.5)$ Å and the lattice vectors are $|\overrightarrow{c_1}| = (30.2\ \pm 0.5)$ Å and $|\overrightarrow{c_2}| = (17.6\ \pm 0.5)$ Å spanning an angle of $\theta = (89\ \pm 5)°$.

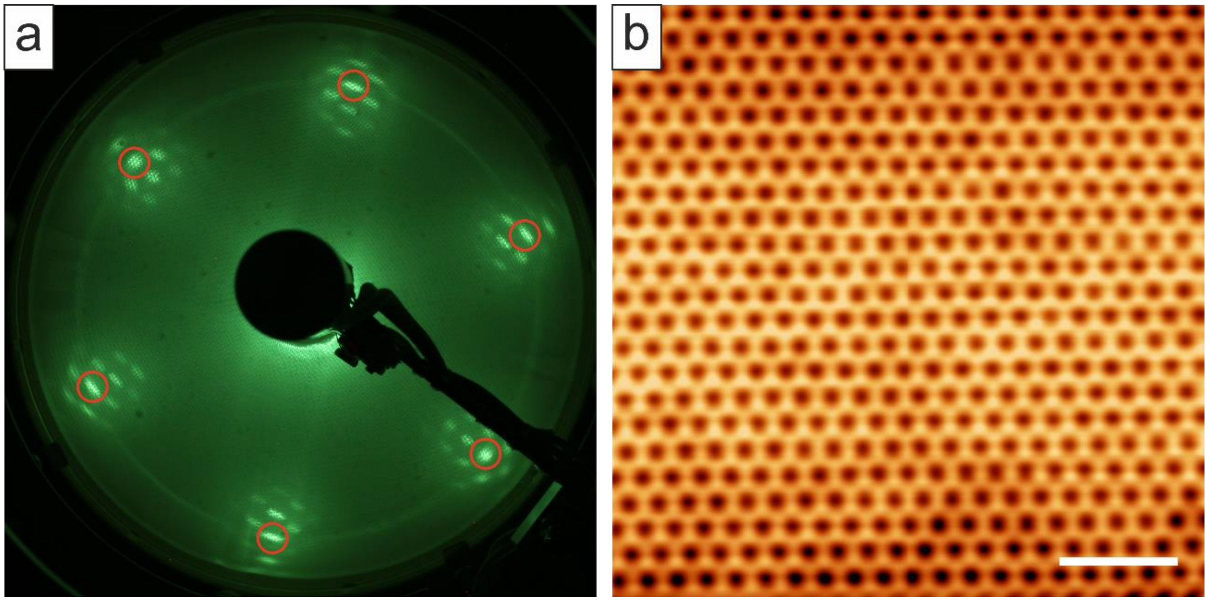

Figure 5-6 Growing Gr on Ir(111).

a) Photograph of the LEED pattern of Gr/Ir(111). The spots marked with red circles correspond to first order spots of Ir(111). The energy of the LEED is 67 eV. b) Long range STM image showing the Moiré pattern of the Gr on Ir(111) (V_{bias} = 5.00 V; I_t = 20 pA. Scale bar: 10nm).

5.2.1 On surface Dy-BCNB coordination metal-organic network on Gr/Ir(111)

Deposition of Dy on a submonolayer coverage of BCNB on Gr/Ir(111) with the substrate held at 338 K and subsequent annealing to 473 K during 30 minutes, leads to the formation of a Dy-directed coordination network on Gr/Ir(111). In this case, even in the low Dy coverage regime, the metal-organic network is mostly based on five-fold coordination nodes (Figure 5-8a). A closer inspection to the network allows to identify an additional 6-fold coordination node taking a role in the network.

The majority five-fold coordination node (79%) is similar to the one found on Au(111)(Figure 5-8b), with an average CN···Dy projected distance of (2.9 ± 0.5) Å, slightly higher than the same distance measured on Au(111). This fact is also observed in the DFT calculations, where the obtained projected distance is in good agreement with the experiment. The Bader analysis of the Dy atom in this node shows a positive charge state of $+2.26e^-$, similar to the one found on Au (111). This seems to point out that the charge state of Dy is governed by the interaction with the crystal field produced by the carbonitriles, with no appreciable contribution of the substrate.

The minority coordination node (21%) is 6-fold and dinuclear (Figure 5-8c). In this case, it was possible to spatially resolve the centres, seeing clearly two bright balls directly assigned to Dy atoms, in which the average CN···Dy projected distance is (2.5 ± 0.5) Å.

Importantly, the 4-fold coordination node is missing, indicating that the gold adatoms are mandatory for the expression of such node on Au(111) and reinforcing our rationalization of the previous networks.

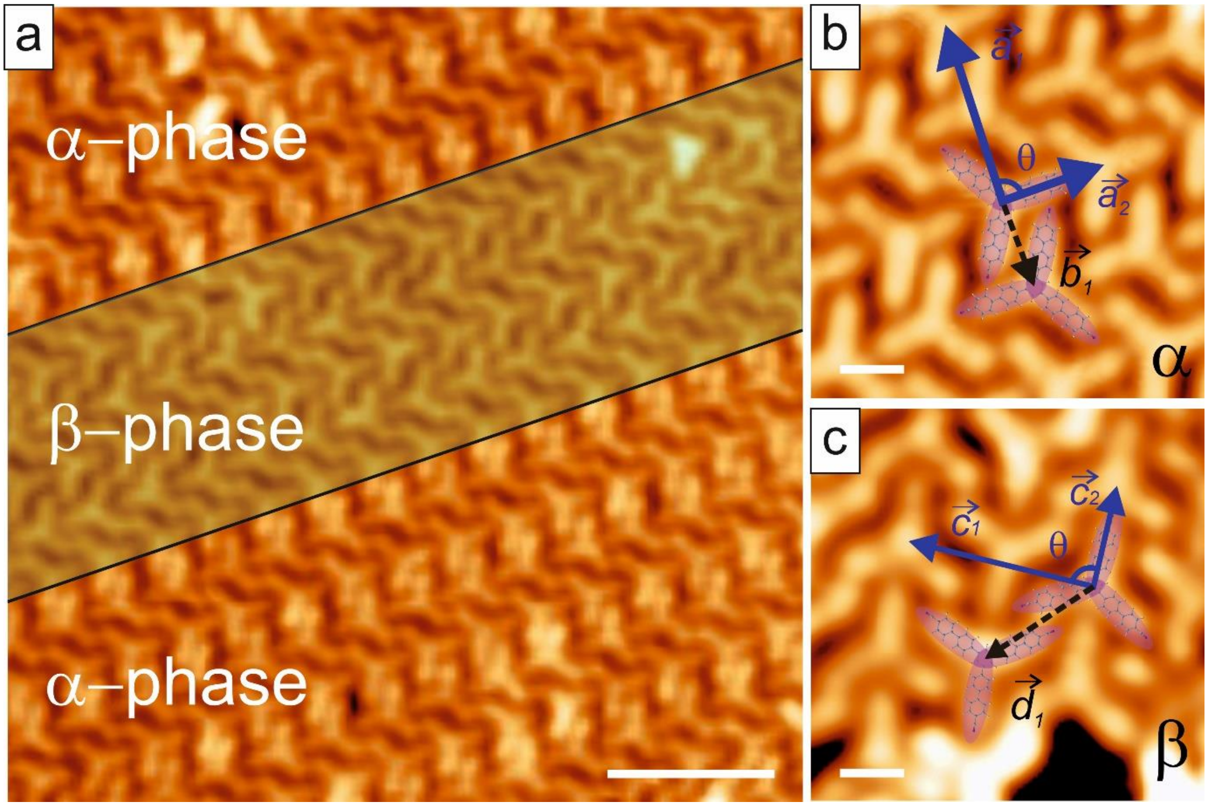

Figure 5-7 Self-assembly of BCNB on Gr/Ir(111).

a) STM image of the self-assembly of BCNB on top of Gr/Ir(111). The self-assembly shows two different phases (V_{bias} = -1.00 V; I_t = 100 pA. Scale bar: 5 nm). b) High resolution STM image of α-phase with the corresponding superimposed atomistic model. The dotted black arrow represents the basis vector $\overrightarrow{b_1} = (14.5\ \pm 0.5)$ Å and the blue arrows are the vectors of the unit cell $\overrightarrow{a_1} = (29.4\ \pm 0.5)$ Å, $\overrightarrow{a_2} = (17.1\ \pm 0.5)$ Å, forming an angle of $\theta = (88\ \pm 5)°$ (V_{bias} = 0.80 V; I_t = 400 pA. Scale bar: 1 nm). c) High resolution STM image of β-phase with superimposed atomistic model. The basis vector is $\overrightarrow{d_1} = (20.7\ \pm 0.5)$ Å and the vectors of the unit cell are $\overrightarrow{c_1} = (30.2 \pm 0.5)$ Å, and $\overrightarrow{c_2} = (17.6\ \pm 0.5)$ Å spanning an angle of $\theta = (89\ \pm 5)°$ (V_{bias} = 0.80 V; I_t = 10 pA. Scale bar: 1 nm)

5.3 Conclusions

In this chapter it has been shown the feasibility to grow Dy-carbonitrile coordination networks on Au(111) and on Gr/Ir(111), preserving the structural characteristics dictated by the lanthanide on both surfaces. Thus, it is expected that many designs found and to be found on metals could be reproduced on sp^2 supports, opening fascinating avenues for chemical engineering on surfaces.

First, the deposition of BCNB molecules on Au(111) leads to the formation of large molecular islands featuring an hexagonal pattern. Additionally, subsequent annealing of this self-assembly phase gives rise to a metal-organic phase based on gold adatoms.

Second, deposition of Dy atoms on a submonolayer coverage of BCNB on Au(111) and subsequent annealing to 373 K affords a new metal-organic phase based on Dy-directed 5-fold mononuclear coordination nodes, 6-fold dinuclear Dy nodes and 4-fold mononuclear Au nodes.

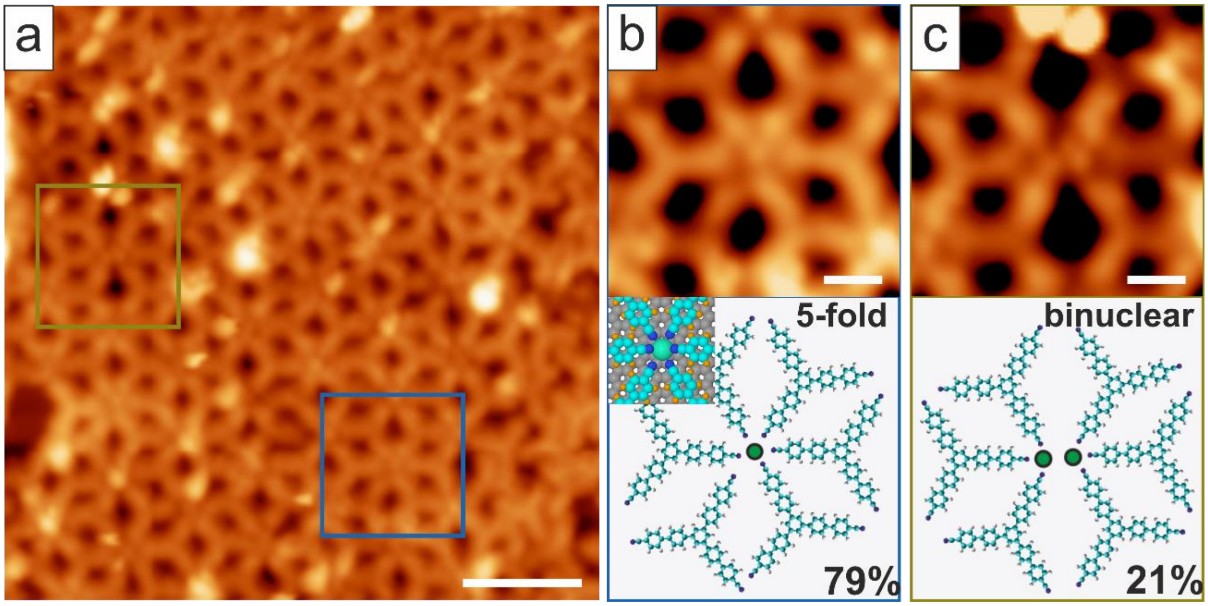

Figure 5-8 Dy-BCNB coordination network on Gr/Ir(111).

a) STM image showing the first Dy-based metal-organic network on Gr/Ir(111) (V_{bias} = 0.50 V; I_t = 10 pA. Scale bar: 4 nm). b) High resolution STM image of the 5-fold node marked by a blue square in a). An atomistic model is proposed in the lower panel. The inset corresponds to a DFT calculation of the 5-fold node on Gr. One of the molecules is not contributing to the coordination bond. c) High resolution image of the dinuclear node marked with a green square in image a). The atomistic model is proposed in the lower panel. The percentages in the corners of the lower panel indicate the abundancy of these nodes in the lattice.

DFT simulations confirm the structural characteristics of the 5-fold centers. In addition, the Bader analysis of Dy in these nodes reveals a positive state charge of $+2.35e^{-}$ on Au(111) and of $+2.26e^{-}$ on Gr/Ir(111), both compatible with a 3^{+} oxidation state of the Dy. This indicates the almost negligible contribution of the substrate in the charge state of Dy upon coordination with lateral ligands.

Third, the deposition of BCNB on Gr/Ir(111) results in a different self-assembly from the one obtained on Au(111). Two distinct phases are detected, both of them forming rectangular lattices with two molecules on the basis, and a distinct arrangement of the basis, though both of them are based on hydrogen bonds between adjacent molecular species.

Subsequent deposition of Dy on a submonolayer coverage of BNCB on Gr/Ir(111) and annealing to 473 K affords the expression of a nanoarchitecture based on Dy-directed mononuclear 5-fold nodes and dinuclear 6-fold nodes, which features almost the same structure as its homologous on Au(111), only distinguishable for the absence of Au adatoms.

In summary, it has been possible to reproduce a Dy-directed metal-organic architecture both on Au(111) and Gr/Ir(111), while preserving the local order. Such results opens new avenues to grow such lanthanide directed nanostructures on decoupling layers like Gr/Ir(111), in order to study the inherente physico-chemical properties of lanthanide-directed metallosupramolecular network, while avoiding the pernicious role of the metallic support.

6. General conclusions and perspectives

This thesis reports a comprehensive study of the structural, electronic and magnetic properties of lanthanide-directed metallosupramolecular networks on surfaces, both on metals and on graphene/Ir(111).

The main postulate of the thesis, i.e. the capabilities of metal-organic coordination to tune the magnetic properties of lanthanides, has been proven, opening fascinating opportunities for nanomagnetism.

Despite our efforts, magnetic remanence could not be observed on the samples grown on metals, probably due to the interaction with the reservoir of electronic states and phonons of the metal. Steered by such concomitant limitations, we introduce the first metallosupramolecular architectures on a sp^2 template (graphene/Ir(111)), in which lanthanides play the major structural directing role. From such success, we anticipate fascinating results regarding the pristine electronic and magnetic properties of that family of coordinative nanostructures.

To achieve our goals, we have relied on a very powerful combination of surface science techniques complemented by DFT, Hamiltonian modelling and multiplet calculations. Structural characterization of the samples has been performed with ultimate spatial resolution by STM, while STS measurements have provided access to their local electronic density of states, including energy level alignment with respect to Fermi and spatial distribution. Further insights about oxidation state and charge distribution have been granted by XAS and XNLD, respectively, at ALBA synchrotron. In addition, the magnetic behaviour of lanthanides has been inspected with XMCD and complemented by multiplet calculations, providing insights on the magnetic moments, magnetic anisotropy and orientation of the easy axis.

More in detail, in the third chapter of the thesis, it is studied the electronic and magnetic properties of the reticular architecture formed by the coordination of Dy with a ditopic organic linker, equipped with carboxylate moieties (TDA) on Cu(111). Despite being the nature of the bond mostly ionic, as expected for lanthanides and corroborated by DFT, the experiments show a minor covalent contribution. In addition, synchrotron studies reveal the high impact that the coordination has on the properties of Dy. Upon coordination, the Dy changes its oxidation state from divalent (individual Dy atoms on the surface) to trivalent (Dy embedded in the metal-organic network). The crystal field imposed by the oxygens from the carboxylate moieties strongly increases the magnetic anisotropy compared to Dy clusters or individual Dy atoms. In addition, such electrostatic role dominates over the symmetry of the crystal field, tilting the easy axis of anisotropy, which is placed close to the surface plane.

Next, we take advantage of a shorter linker (TPA), though equipped with analogous terminal functional groups. The result is the formation of a reticular architecture directed by Dy mononuclear nodes, in which the magnetic anisotropy is increased as compared to the Dy-TDA counterpart, though keeping the easy axis of magnetization close to the surface plane.

Altogether, our findings from the third chapter highlight the extraordinary potential of metallosupramolecular networks on surfaces to tune the crystal field in order to increase the magnetic anisotropy and possibly achieve magnetic bistability. Unfortunately, no magnetic remanence was observed, which could be assigned to the role of the substrate or to a faster relaxation time than our experimental temporal window. To circumvent such limitations two strategies have been developed in chapters 4 and 5. First strategy deals with modifying the linking functional group to tailor the crystal field. Second strategy addresses the design of metallosupramolecular networks on decoupling supports.

Thus, in the fourth chapter, we have addressed the coordination of a ditopic linear biphenyl species equipped with pyridyl linking units at their termini (DPBP). Since no activation of the pyridyl functional group to steer coordination was necessary, we performed our experiments on Au(111). To our surprise, the resulting metallosupramolecular architectures were directed by lanthanide dinuclear nodes, and not by mononuclear ones. Two distinct lanthanide elements were employed: Dy and Er, since they are archetypes of oblate and prolate charge density distribution for maximum J_z moments. Structurally, by preserving the lanthanide:linker stoichiometry, but varying the coverage, it is possible to move from a Kagome (low coverage) to a rhombic (close to monolayer) metallosupramolecular architecture. High resolution STM images unambiguously reveal that both networks are directed by dinuclear nodes, preserving the electronic structure as it is revealed by STS. Importantly, the metal exchange results in the same metallosupramolecular architecture, thus opening fascinating opportunities for maintaining structural integrity, while modifying the directing lanthanide metal. In fact, STS reveals a shift of the frontier orbitals while comparing the Dy- versus the Er-networks, which is assigned to the distinct electronic nature of Er, presenting two more f electrons than Dy.

Next, we pay attention to the information about the electronic structure provided by synchrotron techniques for the rhombic network. In this sense, XAS experiments confirm the trivalent oxidation of both Dy and Er. However, XLND reveals that the distribution of the charge is distinct in both cases, being out-of-plane for Dy, while tilted for Er. Additional experiments on Dy-DBPB Kagome network also reveal that the Dy shows a trivalent oxidation state and out-of-plane charge distribution.

Regarding the magnetic properties of Dy-DPBP Kagome and rhombic networks, XMCD measurements display that both structures present a strong magnetic anisotropy, with the easy axis oriented close to the plane of the surface. Multiplet calculations ratify our XAS, XNLD and XMCD rationalization for the Dy-DPBP rhombic network, displaying a maximum value J_z=15/2.

In addition, the substitution of Dy by Er produces a deep variation in the magnetic properties for the rhombic networks. A similar behaviour between Er-DPBP rhombic and Er-DPBP Kagome networks is expected by comparison with the Dy-DPBP counterparts. XMCD curves for the Er-DPBP rhombic system show that Er atoms are mostly isotropic, in contrast with Dy networks. Nevertheless, multiplet calculations confirm the magnetic anisotropy of the Er atoms, which present an easy axis tilted 50° with respect to the normal of the surface. Here, it is worth to mention that the signal at grazing incidence is an average of six supramolecular domains and, thus, as it is the case here, a direct comparison between the values of XMCD at NI and GI could be misleading, and theoretical input is always necessary, as we did. Quantitatively, Dy-DPBP rhombic networks present 2.6 times greater magnetic anisotropy than Er-DPBP counterparts.

Altogether, results from chapter 4 indicate the feasibility to keep the same structural design, while exchanging the lanthanide element. In addition, such findings illustrate the first lanthanide-driven dinuclear metallosupramolecular periodic architectures reported up to date to the best of our knowledge. Both scientific inputs will contribute to develop lanthanide materials science from a pure design perspective. Furthermore, we clearly observe the capability of tuning the energy level alignment of frontier orbitals by metal exchange, which could have deep implications in future applications of lanthanide-based low dimensional systems in metallosupramolecular electronics, optoelectronics and spintronics. Finally, the capability of tailoring the easy axis of magnetization as well as improving drastically the magnetic anisotropy of lanthanides in dinuclear metallosupramolecular designs opens pathways in the quest for single atom magnetism on surfaces. Actually and unfortunately, no magnetic remanence in absence of magnetic field could be observed for any of the dinuclear DPBP metal-organic networks, which signals that another strategy, not simply based on changing the functional group, must be adopted to engineer magnetic bistability on surfaces.

To this aim, on chapter 5, we directly pioneer the design of a lanthanide metallosupramolecular architecture on Gr/Ir(111), a sp^2 template, since such substrate is reported to allow the maintenance of magnetic stability for isolated Dy atoms grown on top. At the submission of this thesis, we have requested and been granted beamtime to explore the electronic and magnetic properties of such architecture.

After trial and error attempts based on our knowledge of lanthanide chemistry, we could engineer the coordination of Dy with a three-fold linker equipped with terminal coordinative carbonitrile moieties (BNCB). First, we inspect the quasi-hexagonal metallosupramolecular Dy-directed architecture formed on Au(111), which is based on

Au four-fold nodes and Dy five-fold mononuclear and six-fold dinuclear nodes. Second, we move to Gr/Ir(111), where we observe a related quasi-hexagonal self-assembly, lacking the Au four-fold nodes. Thus, we reveal that it is feasible to engineer lanthanide-directed networks on sp^2 templates, and that such assemblies could be very related to the ones found on metals, while avoiding the pernicious role of the electronic adsorbate-substrate interaction and the participation of metal adatoms. Such findings would help to speed up the synthesis of lanthanide metal-organic low dimensional materials on decoupling supports, allowing to explore the intrinsic properties of lanthanides in coordination environments.

In summary, the findings described in this thesis points that metallosupramolecular coordination chemistry is an excellent paradigm to engineer lanthanide-based bidimensional materials with tuneable electronic and magnetic properties.

At the submission of this thesis, magnetic remanence has not been observed in any of these systems. Future experiments involving decoupling layers, principally Gr/Ir(111), are envisioned in order to determine the role of the substrate in the stabilization of the lanthanide magnetic moments. Additionally, electron spin resonance measurements of these networks are anticipated to be crucial, since they could give insights about the local magnetic behaviour of lanthanides, as well as their behaviour as qubits, thus being of relevance for magnetic information storage and quantum nanoscience.

In addition, we anticipate that scientific community will pay attention to the optical properties of lanthanides. Though, it has not been the scope of this thesis, lanthanides have unique light emission properties, like their extreme narrow line-like emission. The tunability of such properties by means of coordination chemistry could be of extraordinary relevance to engineer low dimensional materials for optoelectronics and displays.

To conclude, I consider this thesis an important step to make reality the promising opportunities that lanthanide-based low dimensional materials, as an emerging field, have to offer both to science and technology.

7. Conclusiones generales y perspectivas

En esta tesis se realiza un estudio de las características estructurales, electrónicas y magnéticas de redes metalosupramoleculares dirigidas por lantánidos en superficies, tanto en metales como en grafeno/Ir(111).

El postulado fundamental de esta tesis reside en contrastar la capacidad de la coordinación metal-orgánica para modificar las propiedades magnéticas de los lantánidos, lo que abre oportunidades fascinantes para el nanomagnetismo.

A pesar de nuestros esfuerzos, no se ha observado remanencia magnética en las muestras crecidas sobre metales, probablemente debido a la interacción con el reservorio de estados electrónicos y fonones del metal, que inevitablemente relajan el estado magnético del lantánido. Para superar dichas limitaciones, introducimos la primera arquitectura metalosupramolecular dirigida por lantánidos en un soporte sp^2 (grafeno/Ir(111)). De este experimento, anticipamos fascinantes resultados relacionados con las propiedades electrónicas y magnéticas de esta familia de nanoestructuras coordinadas.

Para alcanzar nuestras metas nos hemos servido de una poderosa combinación de técnicas de ciencia de superficies complementadas por cálculos DFT, modelado de Hamiltoniano y cálculo de multipletes. La caracterización estructural de las muestras con máxima resolución espacial se ha hecho con STM, mientras que las medidas de STS han dado acceso a su densidad de estados local, incluyendo el alineamiento de los niveles de energía respecto del nivel de Fermi y su distribución espacial. Medidas de XAS y de XNLD, realizadas en el sincrotrón ALBA han permitido obtener más información sobre los estados de oxidación y la distribución de carga. Además, el comportamiento magnético de los lantánidos se ha inspeccionado con XMCD, obteniendo nueva información sobre los momentos magnéticos, la anisotropía magnética y la orientación del eje fácil, constatado por comparación entre los experimentos y las simulaciones.

Más en detalle, en el tercer capítulo de la tesis se estudian las propiedades electrónicas y magnéticas de arquitecturas reticulares formadas por la coordinación de átomos de Dy con ligandos lineales equipados con grupos carboxilatos (TDA) sobre Cu(111). A pesar de que la naturaleza del enlace es mayormente iónica, los experimentos muestran una pequeña contribución covalente, corroborada por cálculos DFT. Además, los estudios realizados en sincrotrón revelan el alto impacto que tiene la coordinación química sobre el Dy. Tras coordinar, el Dy cambia su estado de oxidación desde una configuración divalente (átomos de Dy individuales en superficie) a una configuración trivalente (Dy coordinado en redes metal-orgánicas). El campo cristalino impuesto por los oxígenos del grupo carboxilato aumenta en gran medida la anisotropía magnética en comparación con átomos individuales o Dy agregado. Adicionalmente, el efecto electroestático domina sobre la simetría del campo cristalino, inclinando el eje fácil de anisotropía hasta ubicarlo cerca de la superficie del plano.

A continuación, escogemos un ligando más corto (TPA) equipado con el mismo grupo funcional. El resultado es la formación de una arquitectura reticular compuesta por nodos mononucleares de Dy, en la cual la anisotropía magnética se ve incrementada en comparación con su contraparte Dy-TDA aunque conserva el eje fácil de magnetización cercano a la superficie del plano.

En conjunto, los resultados de este tercer capítulo subrayan el extraordinario potencial de las redes metalosupramoleculares en superficie para alterar el campo cristalino en aras de incrementar la anisotropía magnética y posiblemente estabilizar el momento magnético de los lantánidos. Desafortunadamente, no se ha podido ver remanencia magnética, lo que podría deberse al papel del sustrato a una relajación del estado magnético más rápido que nuestra ventana de medida. Para superar dicha limitación, se han desarrollado dos estrategias plasmadas en los capítulos 4 y 5. La primera consiste en modificar el grupo funcional para cambiar el campo cristalino. La segunda consiste en diseñar las redes supramoleculares sobre soportes desacoplantes.

De este modo, en el capítulo 4 hemos estudiado la coordinación de un ligando lineal equipado con grupos piridil en sus posiciones terminales (DPBP). Dado que en este caso no era necesaria la activación del grupo piridil para que se diese la coordinación, los experimentos se realizaron sobre Au(111). Para nuestra sorpresa, las estructuras supramoleculares resultantes manifestaron nodos binucleares de lantánido, en vez mononucleares. Para este experimento, se emplearon dos lantánidos distintos, Dy y Er, que son arquetipos de distribuciones de carga oblato y prolato para momentos J_z máximos. En lo que se refiere a la estructura, preservando la estequiometría mientras se varía el recubrimiento es posible formar una red Kagomé (bajo recubrimiento) o una red rómbica (cerca de una monocapa). Las imágenes de STM muestran sin ambigüedad que ambas redes son binucleares, preservando su estructura electrónica, como revelan las medidas STS. Sin embargo, es importante destacar que el intercambio del metal produce la misma arquitectura supramolecular, abriendo oportunidades fascinantes para mantener la integridad estructural a la vez que se modifica el lantánido. De hecho, las medidas de STS muestran un corrimiento de los orbitales frontera cuando se comparan las redes de Dy y las de Er, debido a la diferente naturaleza electrónica del Er, que tiene dos electrones f más que el Dy.

A continuación, hemos prestado atención a la información sobre la estructura electrónica caracterizada por técnicas de sincrotrón para la red rómbica. En este sentido, los experimentos de XAS confirman que ambos, el Dy y el Er presentan un estado de oxidación trivalente. Sin embargo, el XNLD demuestra que la distribución de carga es distinta en ambos casos, encontrándose fuera del plano en el caso del Dy e inclinada en el caso del Er. Experimentos adicionales sobre la red Dy-DPBP Kagomé revelan que en este caso el Dy también muestra también un estado de oxidación trivalente y distribución de carga fuera del plano.

En lo referente a las propiedades magnéticas de las redes de Dy-DPBP, tanto Kagomé como rómbica, las medidas de XMCD muestran que ambas estructuras presentan una fuerte anisotropía magnética, con su eje fácil orientado cerca del plano de la superficie. Los cálculos de multipletes ratifican nuestra racionalización de los resultados de XAS, XNLD y XMCD para la red Dy-DPBP rómbica, mostrando un valor máximo $J_z = 15/2$.

Además, la sustitución de Dy por Er produce profundas variaciones en las propiedades magnéticas de las redes rómbicas. Por comparación con las redes de Dy-DPBP, se espera un comportamiento similar entre las redes Er-DPBP rómbica y Kagomé. Las curvas de XMCD para la red rómbica Er-DPBP muestran que los átomos de Er son prácticamente isotrópicos en comparación con las redes de Dy. Sin embargo, los cálculos de multipletes confirman la anisotropía magnética de los átomos de Er, que presenta un eje fácil de magnetización inclinado 50° respecto a la normal de la superficie. Llegados a este punto, es importante destacar que la señal medida con incidencia rasante es un promedio entre seis dominios rotacionales de la estructura supramolecular, por tanto una comparación directa entre los valores medidos con incidencia normal y rasante puede resultar errónea, requiriendo refuerzo teórico. Cuantitativamente hablando, las redes Dy-DPBP rómbicas presentan una anisotropía magnética 2.6 veces mayor que su contraparte Er-DPBP.

Por tanto, los resultados del capítulo 4 indican la viabilidad de mantener la estructura a la vez que se intercambia el lantánido. Además, por lo que sabemos, los resultados muestran la primera arquitectura supramolecular binuclear dirigida por lantánidos reportada hasta la fecha. Ambos resultados contribuirán al desarrollo de la ciencia de materiales con lantánidos desde una perspectiva de diseño. Adicionalmente, hemos observado claramente la capacidad de modificar el alineamiento de energía de los orbitales frontera tras el intercambio de metal, lo cual podría tener importantes implicaciones en futuras aplicaciones de sistemas de baja dimensionalidad con lantánidos en electrónica supramolecular, optoelectrónica y espintrónica. Finalmente, la capacidad de modificar el eje fácil de magnetización así como de aumentar drásticamente la anisotropía magnética del lantánido en redes metalosupramoleculares binucleares abre nuevas vías en la misión de obtener imanes atómicos en superficie. Desafortunadamente no hemos visto remanencia magnética para ninguna de las redes DPBP binucleares, lo que parece apuntar a que se necesita adoptar otra estrategia, no simplemente cambiar el grupo funcional, para conseguir la estabilidad magnética en superficies.

Con este propósito, en el capítulo 5 desarrollamos de manera pionera el diseño de una arquitectura supramolecular dirigida por lantánidos sobre Gr/Ir(111), un material sp^2, debido a que demostrado que permite mantener la estabilidad magnética de átomos de

Dy depositados en su superficie. En el momento de entregar la presente tesis, tenemos solicitado y asegurado un tiempo de medida en el sincrotrón para explorar las propiedades electrónicas y magnéticas de estos sistemas.

Después de una serie de intentos de ensayo y error basados en nuestro conocimiento de coordinación química, logramos coordinar Dy con ligandos con forma de trípode equipados con grupos carbonitrilo en sus terminaciones (BCNB). En primer lugar, inspeccionamos la red casi hexagonal formada por la coordinación con Dy sobre Au(111), la cual está formada por nodos de Au con simetría 4 y por nodos de Dy mononucleares de simetría 5 y binucleares de simetría 6. En segundo lugar, crecimos el sistema en Gr/Ir(111), donde observamos un ensamblado similar con orden casi hexagonal que carece de los nodos de Au con simetría 4. Por tanto, demostramos la viabilidad de diseñar redes dirigidas por lantánidos sobre sustratos sp^2, y estos ensamblados podrían asemejarse bastante a sus homólogos en metales, mientras que evitamos el rol de la interacción electrónica del metal y la participación de sus adátomos. Estos descubrimientos ayudarían a acelerar la síntesis de materiales metal-orgánicos de baja dimensionalidad basados en lantánidos sobre soportes desacoplantes, permitiendo explorar las propiedades intrínsecas de los lantánidos en entornos de coordinación.

En resumen, los resultados descritos en esta tesis apuntan a que la coordinación química en superficies es un excelente paradigma para producir materiales magnéticos bidimensionales basados en lantánidos con propiedades ajustables.

En el momento de entrega de la presente tesis, no hemos observado remanencia magnética en ninguno de los sistemas. Se prevén futuros experimentos con sustratos desacoplantes, principalmente Gr/Ir(111), para determinar el papel del sustrato en la estabilización del momento magnético de los lantánidos. Además, medidas utilizando resonancia paramagnética electrónica se anticipan cruciales para obtener información sobre el comportamiento magnético local de los lantánidos y para identificar su comportamiento como bits, siendo de vital importancia para el almacenamiento magnético de la información y la nanociencia cuántica.

Adicionalmente, creemos que la comunidad científica valorará las propiedades ópticas de los lantánidos. Aunque está más allá del alcance de esta tesis, los lantánidos presentan propiedades únicas de emisión de luz, como líneas de emisión muy estrechas y colores altamente puros debido a que presentan niveles de energía electrónicos bien definidos. La modificación de estas propiedades mediante la coordinación química podría ser de extraordinaria relevancia para fabricar materiales de baja dimensionalidad relevantes para la optoelectrónica y pantallas.

Para terminar, considero esta tesis un importante paso adelante para hacer realidad las oportunidades que los materiales de baja dimensionalidad basados en lantánidos tienen que ofrecer tanto para la ciencia como para la tecnología.

8. Anexes

8.1 Annex I: Molecular linkers failing to develop ordered Dy-directed networks on Gr/Ir(111)

Because of the relevance to decouple lanthanide-directed metallosupramolecular architectures from the substrate, we attempted to grow these materials on Gr/Ir(111). Several molecular species involving carbonitrile and pyridyl groups were tested in independent experiments. Nevertheless, most of them showed irregular coordination patterns or not coordination at all. Only the described BCNB species in the thesis were selected because of the formation of metal-organic networks featuring quasi-hexagonal order. In Figure 8-1 we have drawn such attempted organic ligands.

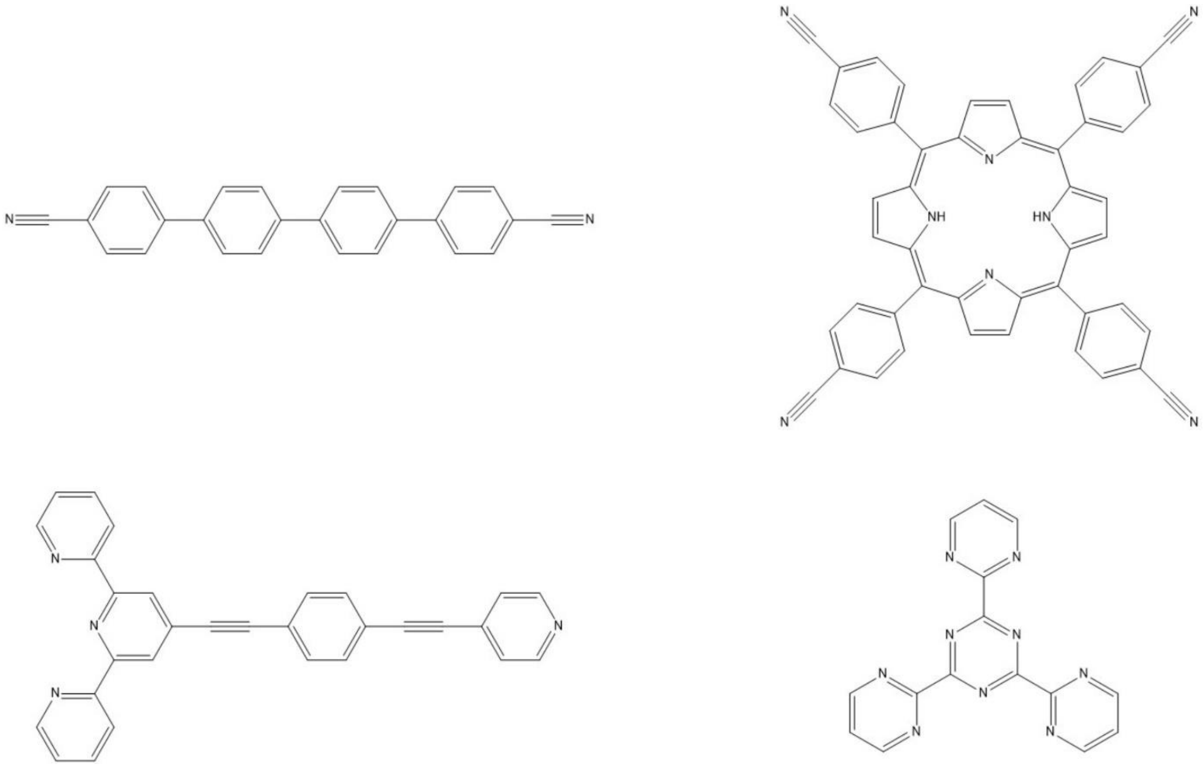

Figure 8-1 Chemical schemes of additional linkers inspected to form surface-confined metal-organic networks on Gr/Ir(111), all of them without success.

9. Bibliography

1. Rinehart, J. D. & Long, J. R. Exploiting single-ion anisotropy in the design of f-element single-molecule magnets. *Chem. Sci.* **2**, 2078–2085 (2011).

2. Rau, I. G. *et al.* Reaching the magnetic anisotropy limit of a 3d metal atom. *Science (80-.).* **344**, 988–992 (2014).

3. Lascialfari, A. *et al.* X-ray magnetic-circular-dichroism spectra on the superparamagnetic transition-metal ion clusters Mn12 and Fe8. *Phys. Rev. B - Condens. Matter Mater. Phys.* **64**, 1–4 (2001).

4. Langenberg, A. *et al.* Spin and orbital magnetic moments of size-selected iron, cobalt, and nickel clusters. *Phys. Rev. B - Condens. Matter Mater. Phys.* **90**, 1–14 (2014).

5. Gambardella, P. *et al.* Giant magnetic anisotropy of single cobalt atoms and nanoparticles. *Science (80-.).* **300**, 1130–1133 (2003).

6. Zadrozny, J. M. *et al.* Magnetic blocking in a linear iron(I) complex. *Nat. Chem.* **5**, 577–581 (2013).

7. Liu, K., Shi, W. & Cheng, P. Toward heterometallic single-molecule magnets: Synthetic strategy, structures and properties of 3d-4f discrete complexes. *Coord. Chem. Rev.* **289–290**, 74–122 (2015).

8. Harrison, A. *et al.* Synthesis, Structure, and Magnetic Properties of the Single-Molecule Magnet [Ni21(cit)12(OH)10(H_2O)10]$^{16-}$. *Dalt. Trans.* **4**, 4271–4274 (2003).

9. Goodwill, J. C. *et al.* Towards nanostructured arrays of single molecule magnets: New Fei9 oxyhydroxide clusters displaying high ground state spins and hysteresis f. *J. Chem. Soc. Dalt. Trans.* 1835–1840 (2000) doi:10.1039/b002135k.

10. Zhong, Z. J. *et al.* A High-Spin Cyanide-Bridged Mn9W6 Cluster (S = 39/2) with a Full-Capped Cubane Structure. *J. Am. Chem. Soc.* 2952–2953 (2000).

11. Soler, M., Wernsdorfer, W., Folting, K., Pink, M. & Christou, G. Single-Molecule Magnets: A Large Mn30Molecular Nanomagnet Exhibiting Quantum Tunneling of Magnetization. *J. Am. Chem. Soc.* **126**, 2156–2165 (2004).

12. Tasiopoulos, A. J., Vinslava, A., Wernsdorfer, W., Abboud, K. A. & Christou, G. Giant single-molecule magnets: A {Mn84} torus and its supramolecular nanotubes. *Angew. Chemie - Int. Ed.* **43**, 2117–2121 (2004).

13. Winpenny, R. E. P. Serendipitous assembly of polynuclear cage compounds. *J. Chem. Soc. Dalt. Trans.* **2**, 1–10 (2002).

14. Liu, K. *et al.* Constraining the coordination geometries of lanthanide centers and magnetic building blocks in frameworks: A new strategy for molecular nanomagnets. *Chem. Soc. Rev.* **45**, 2423–2439 (2016).

15. Zhang, C. *et al.* A series of lanthanide(iii) metal-organic frameworks derived from a pyridyl-dicarboxylate ligand: Single-molecule magnet behaviour and luminescence properties. *Dalt. Trans.* **49**, 14123–14132 (2020).

16. Hübner, C., Baxevanis, B., Khajetoorians, A. A. & Pfannkuche, D. Symmetry effects on the spin switching of adatoms. *Phys. Rev. B - Condens. Matter Mater. Phys.* **90**, 1–6 (2014).

17. Baltic, R. *et al.* Superlattice of Single Atom Magnets on Graphene. *Nano Lett.* **16**, 7610–7615 (2016).

18. Yamashita, A. *et al.* Wheel-Shaped Er III Zn II 3 Single-Molecule Magnet: A Macrocyclic Approach to Designing Magnetic Anisotropy . *Angew. Chemie* **123**, 4102–4105 (2011).

19. Ungur, L., Leroy, J. J., Korobkov, I., Murugesu, M. & Chibotaru, L. F. Fine-tuning the local symmetry to attain record blocking temperature and magnetic remanence in a single-ion magnet. *Angew. Chemie - Int. Ed.* **53**, 4413–4417 (2014).

20. Ma, Y. J. *et al.* Manipulating On/Off Single-Molecule Magnet Behavior in a Dy(III)-Based Photochromic Complex. *J. Am. Chem. Soc.* **142**, 2682–2689 (2020).

21. Rinck, J. *et al.* An octanuclear [CrIII4DyIII4] 3d-4f single-molecule magnet. *Angew. Chemie - Int. Ed.* **49**, 7583–7587 (2010).

22. Fatila, E. M. *et al.* Fine-tuning the single-molecule magnet properties of a [Dy(III)-Radical] 2 pair. *J. Am. Chem. Soc.* **135**, 9596–9599 (2013).

23. Feng, M. *et al.* Chiral Erbium(III) Complexes: single-molecule magnet behavior, chirality, and nuclearity control. *Inorg. Chem.* **58**, 10694–10703 (2019).

24. Singha, A. *et al.* Mapping Orbital-Resolved Magnetism in Single Lanthanide Atoms. *ACS Nano* (2021).

25. Singha, A. *et al.* Magnetic Hysteresis in Er Trimers on Cu(111). *Nano Lett.* **16**, 3475–3481 (2016).

26. Wäckerlin, C. *et al.* Giant Hysteresis of Single-Molecule Magnets Adsorbed on a Nonmagnetic Insulator. *Adv. Mater.* **28**, 5195–5199 (2016).

27. Urgel, J. I. *et al.* Surface-Supported Robust 2D Lanthanide-Carboxylate Coordination Networks. *Small* **11**, 6358–6364 (2015).

28. Jiang, S.-D., Wang, B.-W., Su, G., Wang, Z.-M. & Gao, S. A Mononuclear Dysprosium Complex Featuring Single-Molecule-Magnet Behavior. *Angew. Chemie* **122**, 7610–

7613 (2010).

29. Cirera, B. *et al.* Dysprosium-carboxylate nanomeshes with tunable cavity size and assembly motif through ionic interactions. *Chem. Commun.* **52**, 11227–11230 (2016).

30. Klein, M. J. On a Degeneracy Theorem of Kramers. *Am. J. Phys.* **20**, 65–71 (1952).

31. Ara, F. *et al.* Spin properties of single-molecule magnet of double-decker Tb(III)-phthalocyanine (TbPc2) on ferromagnetic Co film characterized by spin polarized STM (SP-STM). *J. Appl. Phys.* **125**, (2019).

32. Gonidec, M. *et al.* Surface supramolecular organization of a terbium(III) double-decker complex on graphite and its single molecule magnet behavior. *J. Am. Chem. Soc.* **133**, 6603–6612 (2011).

33. Ishikawa, N., Sugita, M. & Wernsdorfer, W. Quantum tunneling of magnetization in lanthanide single-molecule magnets: Bis(phthalocyaninato)terbium and bis(phthalocyaninato)dysprosium anions. *Angew. Chemie - Int. Ed.* **44**, 2931–2935 (2005).

34. Wang, H., Cao, W., Liu, T., Duan, C. & Jiang, J. Synthesis, structure, and single-molecule magnetic properties of rare-earth sandwich complexes with mixed phthalocyanine and Schiff base ligands. *Chem. - A Eur. J.* **19**, 2266–2270 (2013).

35. Ecija, D. *et al.* Two-dimensional short-range disordered crystalline networks from flexible molecular modules. *ACS Nano* **6**, 4258–4265 (2012).

36. Yan, L. *et al.* Self-assembly of a binodal metal-organic framework exhibiting a demi-regular lattice. *Faraday Discuss.* **204**, 111–121 (2017).

37. Schlickum, U. *et al.* Chiral kagomé lattice from simple ditopic molecular bricks. *J. Am. Chem. Soc.* **130**, 11778–11782 (2008).

38. Schüller, L. *et al.* Deposition order controls the first stages of a metal-organic coordination network on an insulator surface. *J. Phys. Chem. C* **120**, 14730–14735 (2016).

39. Zhang, R. *et al.* On-surface Synthesis of a Semiconducting 2D Metal–Organic Framework Cu 3 (C 6 O 6) Exhibiting Dispersive Electronic Bands . *Angew. Chemie* **132**, 2691–2695 (2020).

40. Barth, J. V. Fresh perspectives for surface coordination chemistry. *Surf. Sci.* **603**, 1533–1541 (2009).

41. Barth, J. V., Costantini, G. & Kern, K. Engineering atomic and molecular nanostructures at surfaces. *Nature* **437**, 671–679 (2005).

42. Urgel, J. I. *et al.* Controlling coordination reactions and assembly on a Cu(111)

supported boron nitride monolayer. *J. Am. Chem. Soc.* **137**, 2420–2423 (2015).

43. Shi, Z. *et al.* ._Metallo-supramolecular assembly.pdf. 6150–6153 (2011).

44. Stepanow, S., Lin, N., Barth, J. V. & Kern, K. Surface-template assembly of two-dimensional metal - organic coordination networks. *J. Phys. Chem. B* **110**, 23472–23477 (2006).

45. Barth, J. V. Molecular Architectonic on Metal Surfaces. *Annu. Rev. Phys. Chem.* **58**, 375–407 (2007).

46. Dong, L., Gao, Z. A. & Lin, N. Self-assembly of metal–organic coordination structures on surfaces. *Prog. Surf. Sci.* **91**, 101–135 (2016).

47. Lyu, G. *et al.* Tunable lanthanide-directed metallosupramolecular networks by exploiting coordinative flexibility through ligand stoichiometry. *Chem. Commun.* **52**, 1618–1621 (2016).

48. Urgel, J. I. *et al.* Quasicrystallinity expressed in two-dimensional coordination networks. *Nat. Chem.* **8**, 657–662 (2016).

49. Urgel, J. I. *et al.* Orthogonal insertion of lanthanide and transition-metal atoms in metal-organic networks on surfaces. *Angew. Chemie - Int. Ed.* **54**, 6163–6167 (2015).

50. Écija, D., Urgel, J. I., Seitsonen, A. P., Auwärter, W. & Barth, J. V. Lanthanide-Directed Assembly of Interfacial Coordination Architectures-From Complex Networks to Functional Nanosystems. *Acc. Chem. Res.* **51**, 365–375 (2018).

51. Ginting, E. & Zhou, J. The growth of CeOx(111) thin films on Ru(0001). *IOP Conf. Ser. Earth Environ. Sci.* **753**, (2021).

52. Morales, E. H., He, Y., Vinnichenko, M., Delley, B. & Diebold, U. Surface structure of Sn-doped in2O3 (111) thin films by STM. *New J. Phys.* **10**, (2008).

53. Pundt, A., Getzlaff, M. & Bode, M. H-induced plastic deformation of Gd thin films studied by STM. *Phys. Rev. B - Condens. Matter Mater. Phys.* **61**, 9964–9967 (2000).

54. Stavale, F., Nilius, N. & Freund, H. J. STM luminescence spectroscopy of intrinsic defects in ZnO(0001) thin films. *J. Phys. Chem. Lett.* **4**, 3972–3976 (2013).

55. Wang, Z. *et al.* Strain-relief patterns and kagome lattice in self-assembled c60 thin films grown on cd(0001). *Int. J. Mol. Sci.* **22**, 1–8 (2021).

56. Crommie, M. F., Lutz, C. P., Eigler, D. M. & Heller, E. J. Quantum corrals. *Phys. D Nonlinear Phenom.* **83**, 98–108 (1995).

57. Renard, J., Lundeberg, M. B., Folk, J. A. & Pennec, Y. Real-time imaging of k atoms on graphite: Interactions and diffusion. *Phys. Rev. Lett.* **106**, 2–5 (2011).

58. Dujardin, G. *et al.* Vertical manipulation of individual atoms by a direct stm tip-surface contact on Ge(111). *Phys. Rev. Lett.* **80**, 3085–3088 (1998).

59. Manuscript, A. ce d M us cri Ac pt. (2018).

60. Yang, K. *et al.* Coherent spin manipulation of individual atoms on a surface. *Science (80-.).* **366**, 509–512 (2019).

61. Cirera, B. *et al.* On-surface synthesis of organocopper metallacycles through activation of inner diacetylene moieties . *Chem. Sci.* (2021).

62. Cirera, B. *et al.* Thermal selectivity of intermolecular versus intramolecular reactions on surfaces. *Nat. Commun.* **7**, 1–8 (2016).

63. Auwärter, W. *et al.* Conformational adaptation and selective adatom capturing of tetrapyridyl-porphyrin molecules on a copper (111) surface. *J. Am. Chem. Soc.* **129**, 11279–11285 (2007).

64. Bischoff, F. *et al.* Exploration of Interfacial Porphine Coupling Schemes and Hybrid Systems by Bond-Resolved Scanning Probe Microscopy. *Angew. Chemie* **130**, 16262–16267 (2018).

65. Swart, I., Sonnleitner, T., Niedenführ, J. & Repp, J. Controlled lateral manipulation of molecules on insulating films by STM. *Nano Lett.* **12**, 1070–1074 (2012).

66. Sánchez-Grande, A. *et al.* Diradical Organic One-Dimensional Polymers Synthesized on a Metallic Surface. *Angew. Chemie - Int. Ed.* **59**, 17594–17599 (2020).

67. Corso, M. & de Oteyza, D. G. Topological engineering for metallic polymers. *Nat. Nanotechnol.* **15**, 421–423 (2020).

68. Bieri, M. *et al.* Surface-supported 2D heterotriangulene polymers. *Chem. Commun.* **47**, 10239–10241 (2011).

69. Cirera, B. *et al.* Engineer Quasi-Metallic Polymers. doi:10.1038/s41565-020-0668-7.

70. Saywell, A., Schwarz, J., Hecht, S. & Grill, L. Polymerization on Stepped Surfaces: Alignment of Polymers and Identification of Catalytic Sites. *Angew. Chemie* **124**, 5186–5190 (2012).

71. Tersoff, J. & Hamann, D. R. Theory of the scanning tunneling microscope. *Phys. Rev. B* **31**, 805–813 (1985).

72. Prange, R. E. Tunneling from a many-particle point of view. *Phys. Rev.* **131**, 1083–1086 (1963).

73. Jiao, L. *et al.* Magnetic and defect probes of the SmB6 surface state. *Sci. Adv.* **4**,

(2018).

74. Chen, J. *et al.* Delocalized Surface State in Epitaxial Si(111) Film with Spontaneous √ 3 × √ 3 Superstructure. *Sci. Rep.* **5**, 1–8 (2015).

75. Yamada, M., Hirahara, T. & Hasegawa, S. Magnetoresistance Measurements of a Superconducting Surface State of In-Induced and Pb-Induced Structures on Si(111). *Phys. Rev. Lett.* **110**, 2–6 (2013).

76. Li, G., Luican, A. & Andrei, E. Y. Scanning tunneling spectroscopy of graphene on graphite. *Phys. Rev. Lett.* **102**, 1–4 (2009).

77. Li, Q. *et al.* Grain Boundary Structures and Electronic Properties of Hexagonal Boron Nitride on Cu(111). *Nano Lett.* **15**, 5804–5810 (2015).

78. Chae, J. *et al.* Renormalization of the graphene dispersion velocity determined from scanning tunneling spectroscopy. *Phys. Rev. Lett.* **109**, 1–5 (2012).

79. Sánchez-Grande, A. *et al.* Unravelling the Open-Shell Character of Peripentacene on Au(111). *J. Phys. Chem. Lett.* **12**, 330–336 (2021).

80. Joshi, S. *et al.* Control of molecular organization and energy level alignment by an electronically nanopatterned boron nitride template. *ACS Nano* **8**, 430–442 (2014).

81. Wiengarten, A. *et al.* Surface-assisted dehydrogenative homocoupling of porphine molecules. *J. Am. Chem. Soc.* **136**, 9346–9354 (2014).

82. Ternes, M. Spin excitations and correlations in scanning tunneling spectroscopy. *New J. Phys.* **17**, (2015).

83. Kim, H., Chang, Y. H., Lee, S. H., Kim, Y. H. & Kahng, S. J. Switching and sensing spin states of Co-porphyrin in bimolecular reactions on Au(111) using scanning tunneling microscopy. *ACS Nano* **7**, 9312–9317 (2013).

84. Pietzsch, O. Observation of Magnetic Hysteresis at the Nanometer Scale by Spin-Polarized Scanning Tunneling Spectroscopy. *Science (80-.).* **292**, 2053–2056 (2001).

85. Martín-Fuentes, C. *et al.* Cumulene-like bridged indeno[1,2-b]fluorene π-conjugated polymers synthesized on metal surfaces. *Chem. Commun.* **57**, 7545–7548 (2021).

86. Biswas, K. *et al.* On-surface synthesis of doubly-linked one-dimensional pentacene ladder polymers. *Chem. Commun.* **56**, 15309–15312 (2020).

87. Malavolti, L. *et al.* Magnetism of TbPc2 SMMs on ferromagnetic electrodes used in organic spintronics. *Chem. Commun.* **49**, 11506–11508 (2013).

88. Suzuki, M. *et al.* Magnetic anisotropy of the van der Waals ferromagnet

Cr$_2$Ge$_2$Te$_6$ studied by angular-dependent XMCD. 1–17 (2021).

89. Scholl, A. Observation of antiferromagnetic domains in epitaxial thin films. *Science (80-.).* **287**, 1014–1016 (2000).

90. Stöhr, J. *et al.* Images of the antiferromagnetic structure of a NiO(100) surface by means of X-ray magnetic linear dichroism spectromicroscopy. *Phys. Rev. Lett.* **83**, 1862–1865 (1999).

91. Luo, C., Ryll, H., Back, C. H. & Radu, F. X-ray magnetic linear dichroism as a probe for non-collinear magnetic state in ferrimagnetic single layer exchange bias systems. *Sci. Rep.* **9**, 1–9 (2019).

92. van der Laan, G. & Figueroa, A. I. X-ray magnetic circular dichroism - A versatile tool to study magnetism. *Coord. Chem. Rev.* **277**, 95–129 (2014).

93. Singha, A. *et al.* 4F Occupancy and Magnetism of Rare-Earth Atoms Adsorbed on Metal Substrates. *Phys. Rev. B* **96**, 1–13 (2017).

94. Shelford, L. R. *et al.* Electronic structure of Fe and Co magnetic adatoms on Bi 2Te 3 surfaces. *Phys. Rev. B - Condens. Matter Mater. Phys.* **86**, 1–5 (2012).

95. Dreiser, J. *et al.* Out-of-Plane Alignment of Er(trensal) Easy Magnetization Axes Using Graphene. *ACS Nano* **10**, 2887–2892 (2016).

96. Umbach, T. R. *et al.* Ferromagnetic coupling of mononuclear Fe centers in a self-assembled metal-organic network on Au(111). *Phys. Rev. Lett.* **109**, 1–5 (2012).

97. Baek, S.-J., Park, A., Ahn, Y.-J. & Choo, J. Baseline correction using asymmetrically reweighted penalized least squares smoothing. *Analyst* **140**, 250–257 (2015).

98. Carra, P., Thole, B. T., Altarelli, M. & Wang, X. X-ray circular dichroism and local magnetic fields. *Phys. Rev. Lett.* **70**, 694–697 (1993).

99. Chen, C. T. *et al.* Experimental confirmation of the x-ray magnetic circular dichroism sum rules for iron and cobalt. *Phys. Rev. Lett.* **75**, 152–155 (1995).

100. Oura, K., Lifshits, V.G., Saranin, A., Zotov, A.V., Katayama, M. *Surface Science: An Introduction*. (Springer-Verlag Berlin Heidelberg, 2003).

101. Barla, A. *et al.* Design and performance of BOREAS, the beamline for resonant X-ray absorption and scattering experiments at the ALBA synchrotron light source. *J. Synchrotron Radiat.* **23**, 1507–1517 (2016).

102. Lazić, Z. *et al.* Integrating UHV (ultra high vacuum) and HTS (High Temperature Superconducting) magnets for X-ray synchrotron based experiments. *J. Phys. Conf. Ser.* **425**, (2013).

103. Eliseeva, S. V. & Bünzli, J. C. G. Rare earths: Jewels for functional materials of the

future. *New J. Chem.* **35**, 1165–1176 (2011).

104. Bünzli, J. C. G. Review: Lanthanide coordination chemistry: From old concepts to coordination polymers. *J. Coord. Chem.* **67**, 3706–3733 (2014).

105. Donati, F. *et al.* Magnetic remanence in single atoms. *Science (80-.).* **352**, 318–321 (2016).

106. Natterer, F. D. *et al.* Reading and writing single-atom magnets. *Nature* **543**, 226–228 (2017).

107. Singha, A. *et al.* Engineering atomic-scale magnetic fields by dysprosium single atom magnets. *Nat. Commun.* **12**, 6–11 (2021).

108. Schuh, T. *et al.* Magnetic excitations of rare earth atoms and clusters on metallic surfaces. *Nano Lett.* **12**, 4805–4809 (2012).

109. Liddle, S. T. & Van Slageren, J. Improving f-element single molecule magnets. *Chem. Soc. Rev.* **44**, 6655–6669 (2015).

110. Stoll, P. *et al.* Magnetic anisotropy in surface-supported single-ion lanthanide complexes. *Phys. Rev. B* **94**, 1–13 (2016).

111. Parreiras, S. O. *et al.* Tuning the Magnetic Anisotropy of Lanthanides on a Metal Substrate by Metal–Organic Coordination. *Small* **17**, (2021).

112. Lin, N., Dmitriev, A., Weckesser, J., Barth, J. V. & Kern, K. Real-time single-molecule imaging of the formation and dynamics of coordination compounds. *Angew. Chemie - Int. Ed.* **41**, 4779–4783 (2002).

113. Spillmann, H. *et al.* Ja0362353. *J. Am. Chem. SOC* **125**, 10725–10728 (2003).

114. Dmitriev, A., Spillmann, H., Lin, N., Barth, J. V. & Kern, K. Modular assembly of two-dimensional metal-organic coordination networks at a metal surface. *Angew. Chemie - Int. Ed.* **42**, 2670–2673 (2003).

115. Stepanow, S. *et al.* Steering molecular organization and host-guest interactions using two-dimensional nanoporous coordination systems. *Nat. Mater.* **3**, 229–233 (2004).

116. Stepanow, S. *et al.* Programming supramolecular assembly and chirality in two-dimensional dicarboxylate networks on a Cu(100) surface. *Nano Lett.* **5**, 901–904 (2005).

117. Vidal, F. *et al.* Chiral phase transition in two-dimensional supramolecular assemblies of prochiral molecules. *J. Am. Chem. Soc.* **127**, 10101–10106 (2005).

118. Casanova, D., Llunell, M., Alemany, P. & Alvarez, S. The rich stereochemistry of eight-vertex polyhedra: A continuous shape measures study. *Chem. - A Eur. J.* **11**,

1479–1494 (2005).

119. Bünzli, J. C. G. Benefiting from the unique properties of lanthanide ions. *Acc. Chem. Res.* **39**, 53–61 (2006).

120. Kumar, A., Banerjee, K., Foster, A. S. & Liljeroth, P. Two-Dimensional Band Structure in Honeycomb Metal-Organic Frameworks. *Nano Lett.* **18**, 5596–5602 (2018).

121. Li, J. *et al.* Low-Dimensional Metal-Organic Coordination Structures on Graphene. *J. Phys. Chem. C* **123**, 12730–12735 (2019).

122. Baltic, R. *et al.* Magnetic properties of single rare-earth atoms on graphene/Ir(111). *Phys. Rev. B* **98**, 1–12 (2018).

123. Studniarek, M. *et al.* Understanding the Superior Stability of Single-Molecule Magnets on an Oxide Film. *Adv. Sci.* **6**, (2019).

124. Wang, H., Wang, K., Tao, J. & Jiang, J. Twist angle perturbation on mixed (phthalocyaninato)(porphyrinato) dysprosium(III) double-decker SMMs. *Chem. Commun.* **48**, 2973–2975 (2012).

125. Thole, B. T., Carra, P., Sette, F. & Van Der Laan, G. X-ray circular dichroism as a probe of orbital magnetization. *Phys. Rev. Lett.* **68**, 1943–1946 (1992).

126. Gatteschi, D. & Sessoli, R. Quantum tunneling of magnetization and related phenomena in molecular materials. *Angew. Chemie - Int. Ed.* **42**, 268–297 (2003).

127. Ding, Y. S. *et al.* Field- and temperature-dependent quantum tunnelling of the magnetisation in a large barrier single-molecule magnet. *Nat. Commun.* **9**, 1–10 (2018).

128. Uldry, A., Vernay, F. & Delley, B. Systematic computation of crystal-field multiplets for x-ray core spectroscopies. *Phys. Rev. B - Condens. Matter Mater. Phys.* **85**, 1–14 (2012).

129. Écija, D. *et al.* Five-vertex Archimedean surface tessellation by lanthanide-directed molecular self-assembly. *Proc. Natl. Acad. Sci. U. S. A.* **110**, 6678–6681 (2013).

130. Chen, H. *et al.* Magnetic Archimedean Tessellations in Metal–Organic Frameworks. *J. Am. Chem. Soc.* **2**, 2–6 (2021).

131. Liu, J. *et al.* On-surface preparation of coordinated lanthanide-transition-metal clusters. *Nat. Commun.* **12**, 1–10 (2021).

132. Klyatskaya, S. *et al.* Surface-confined self-assembly of Di-carbonitrile polyphenyls. *Adv. Funct. Mater.* **21**, 1230–1240 (2011).

133. Langner, A. *et al.* Two- to one-dimensional transition of self-assembled coordination networks at surfaces by organic ligand addition. *Chem. Commun.*

134. Lin, T., Shang, X. S., Adisoejoso, J., Liu, P. N. & Lin, N. Steering On-Surface Polymerization with Metal-Directed Template. (2012).

135. Tait, S. L. *et al.* Assembling isostructural metal-organic coordination architectures on Cu(100), Ag(100) and Ag(111) substrates. *ChemPhysChem* **9**, 2495–2499 (2008).

136. Lyu, G., Zhang, R., Zhang, X., Nian Liu, P. & Lin, N. On-surface assembly of low-dimensional Pb-coordinated metal-organic structures. *J. Mater. Chem. C* **3**, 3252–3257 (2015).

137. Shi, Z. & Lin, N. Porphyrin-based two-dimensional coordination kagome lattice self-assembled on a Au(111) surface. *J. Am. Chem. Soc.* **131**, 5376–5377 (2009).

138. Klappenberger, F. Two-dimensional functional molecular nanoarchitectures - Complementary investigations with scanning tunneling microscopy and X-ray spectroscopy. *Prog. Surf. Sci.* **89**, 1–55 (2014).

139. Kumar, A., Banerjee, K., Foster, A. S. & Liljeroth, P. Two-Dimensional Band Structure in Honeycomb Metal-Organic Frameworks. *Nano Lett.* **18**, 5596–5602 (2018).

140. N'Diaye, A. T., Coraux, J., Plasa, T. N., Busse, C. & Michely, T. Structure of epitaxial graphene on Ir(111). *New J. Phys.* **10**, (2008).

141. Coraux, J. *et al.* Growth of graphene on Ir(111). *New J. Phys.* **11**, (2009).

142. Politano, A. *et al.* Evidence for acoustic-like plasmons on epitaxial graphene on Pt(111). *Phys. Rev. B - Condens. Matter Mater. Phys.* **84**, 1–4 (2011).

143. Vázquez De Parga, A. L. *et al.* Periodically rippled graphene: Growth and spatially resolved electronic structure. *Phys. Rev. Lett.* **100**, 1–4 (2008).

144. Ramoino, L. *et al.* Layer-selective epitaxial self-assembly of porphyrins on ultrathin insulators. *Chem. Phys. Lett.* **417**, 22–27 (2006).

145. Abel, M., Clair, S., Ourdjini, O., Mossoyan, M. & Porte, L. Single Layer of Polymeric Fe-Phthalocyanine: An Organometallic Sheet on Metal and Thin Insulating Film. *J. Am. Chem. Soc.* 1203–1205 (2011).

146. Stradi, D. *et al.* Role of dispersion forces in the structure of graphene monolayers on Ru surfaces. *Phys. Rev. Lett.* **106**, 1–4 (2011).

147. Garnica, M. *et al.* Long-range magnetic order in a purely organic 2D layer adsorbed on epitaxial graphene. *Nat. Phys.* **9**, 368–374 (2013).

148. Maccariello, D. *et al.* Spatially resolved, site-dependent charge transfer and induced magnetic moment in TCNQ adsorbed on graphene. *Chem. Mater.* **26**, 2883–2890 (2014).

149. Borca, B. *et al.* Electronic and geometric corrugation of periodically rippled, self-nanostructured graphene epitaxially grown on Ru(0001). *New J. Phys.* **12**, (2010).

150. Barja, S. *et al.* Self-organization of electron acceptor molecules on graphene. *Chem. Commun.* **46**, 8198–8200 (2010).

151. Borca, B., Calleja, F., Hinarejos, J. J., Vzquez De Parga, A. L. & Miranda, R. Reactivity of periodically rippled graphene grown on Ru(0001). *J. Phys. Condens. Matter* **21**, (2009).

152. Calleja, F. *et al.* Spatial variation of a giant spin-orbit effect induces electron confinement in graphene on Pb islands. *Nat. Phys.* **11**, 43–47 (2015).

153. Stradi, D. *et al.* Electron localization in epitaxial graphene on Ru(0001) determined by moiré corrugation. *Phys. Rev. B - Condens. Matter Mater. Phys.* **85**, 1–5 (2012).

154. Preobrajenski, A. B., Ng, M. L., Vinogradov, A. S. & Mårtensson, N. Controlling graphene corrugation on lattice-mismatched substrates. *Phys. Rev. B - Condens. Matter Mater. Phys.* **78**, 2–5 (2008).

155. Martinez-Galera, A. J. *et al.* Imaging molecular orbitals of PTCDA on graphene on Pt(111): Electronic structure by stm and first-principles calculations. *J. Phys. Chem. C* **118**, 12782–12788 (2014).

156. Marchini, S., Günther, S. & Wintterlin, J. Scanning tunneling microscopy of graphene on Ru(0001). *Phys. Rev. B - Condens. Matter Mater. Phys.* **76**, 1–9 (2007).

157. Coraux, J., N'Diaye, A. T., Busse, C. & Michely, T. Structural coherency of graphene on Ir(111). *Nano Lett.* **8**, 565–570 (2008).

158. Wintterlin, J. & Bocquet, M. L. Graphene on metal surfaces. *Surf. Sci.* **603**, 1841–1852 (2009).

159. Moreno, D. *et al.* Dysprosium-directed metallosupramolecular network on graphene/Ir(111). *Chem. Commun.* **57**, 1380–1383 (2021).

160. Sirtl, T. *et al.* Control of intermolecular bonds by deposition rates at room temperature: Hydrogen bonds versus metal coordination in trinitrile monolayers. *J. Am. Chem. Soc.* **135**, 691–695 (2013).

161. Urgel, J. I. *et al.* Five-vertex lanthanide coordination on surfaces: A route to sophisticated nanoarchitectures and tessellations. *J. Phys. Chem. C* **118**, 12908–12915 (2014).

162. Écija, D. *et al.* Five-vertex Archimedean surface tessellation by lanthanide-directed molecular self-assembly. *Proc. Natl. Acad. Sci. U. S. A.* **110**, 6678–6681 (2013).

163. Marschall, M. *et al.* Meta-positioning of carbonitrile functional groups induces interfacial edge-on phase of oligophenyl derivatives. *J. Phys. Chem. C* **118**, 2622–

2633 (2014).

164. Lepper, M. *et al.* Adsorption Behavior of a Cyano-Functionalized Porphyrin on Cu(111) and Ag(111): From Molecular Wires to Ordered Supramolecular Two-Dimensional Aggregates. *J. Phys. Chem. C* **121**, 26361–26371 (2017).

165. Schlickum, U. *et al.* Metal-organic honeycomb nanomeshes with tunable cavity size. *Nano Lett.* **7**, 3813–3817 (2007).

166. Stepanow, S. *et al.* Surface-assisted assembly of 2D metal-organic networks that exhibit unusual threefold coordination symmetry. *Angew. Chemie - Int. Ed.* **46**, 710–713 (2007).

167. Pham, T. A. *et al.* Heat-induced formation of one-dimensional coordination polymers on Au(111): An STM study. *Chem. Commun.* **51**, 14473–14476 (2015).

168. Klappenberger, F. *et al.* Temperature dependence of conformation, chemical state, and metal-directed assembly of tetrapyridyl-porphyrin on Cu(111). *J. Chem. Phys.* **129**, (2008).

169. Barth, J. V. Molecular architectonic on metal surfaces. *Annu. Rev. Phys. Chem.* **58**, 375–407 (2007).